Doctoral Dissertation
Doctoral Program in Civil and Environmental Engineering (34.th cycle)

Pore-scale characterization of rock images

Geometrical analysis and hydrodynamic simulation

Filippo Panini
* * * * *

Supervisors
Dario Viberti
Eloisa Salina Borello

Doctoral Examination Committee:
Prof. Villiam Bortolotti, Referee, University of Bologna
Prof. Claudio Alimonti, Referee, University of Rome "La Sapienza"
Prof. Xiaolong Yin, Colorado School of Mines
Prof. Vera Rocca, Politecnico di Torino
Prof. Francesca Verga, Politecnico di Torino

Politecnico di Torino
April 2022

I hereby declare that, the contents and organisation of this dissertation constitute my own original work and does not compromise in any way the rights of third parties, including those relating to the security of personal data.

. . . . . .

Filippo Panini
Turin, April 2022

Summary

The definition of an optimal reservoir management strategy is fundamental for the primary production of oil and gas, Enhanced Oil Recovery, Underground Gas Storage, Underground Hydrogen Storage, CO_2 storage and geothermal systems. This definition requires a thorough analysis, characterization, description and understanding of fluid flow phenomena occurring in underground porous media. This work proposes a methodology based on geometrical analysis and hydrodynamic modeling in order to estimate microscopic and textural parameters that influence the fluid flow behavior in the pore space. Geometrical analyses and hydrodynamic simulations are run at the pore-scale directly on binary images of rocks. The geometrical analysis is implemented based on the application of the A* algorithm to find paths connecting inlet and outlet points in 2D and 3D rock images. Hydrodynamic simulation is performed using the Lattice Boltzmann Method (LBM) in 2D geometries and the Finite Volume Method (FVM) in 3D geometries. The results obtained through these analyses and simulations are compared and discussed. First of all, 2D binary images are analyzed to characterize the pore network geometry and to estimate effective porosity, pore size distribution and tortuosity. The results show that the path-finding approach can provide reasonable and reliable estimates of the parameters of interest. Then, the methodology is applied to 3D binary images of synthetic rock samples generated with the Quartet Structure Generation Set (QSGS) algorithm. Two different cases, representing an isotropic and an anisotropic porous media, are presented. In these cases, permeability was also estimated by the geometrical approach using the Kozeny-Carman equation and by hydrodynamic simulation inverting the Darcy's equation. The outcome of this investigation evidences that the geometrical analysis used in this research can provide a reliable characterization of 3D porous media.

Acknowledgements

I would like to thank my supervisors Prof. Dario Viberti and Dr. Eloisa Salina Borello for their support and directions during my PhD. Also, I would like to thank Dr. Costanzo Peter. Finally, I would like to thank all my colleagues at Politecnico di Torino.

List of publications

Salina Borello, E., Peter, C., Panini, F., & Viberti, D. (2022). Application of A* algorithm for microstructure and transport properties characterization from 3D rock images. Energy, 122151. https://doi.org/10.1016/j.energy.2021.122151

Panini, F., Salina Borello, E., Peter, C., & Viberti, D. (2022). Application of A* Algorithm for Tortuosity and Effective Porosity Estimation of 2D Rock Images. In: Advanced Problem in Mechanics II. Lecture Notes in Mechanical Engineering. https://doi.org/10.1007/978-3-030-92144-6_39

Viberti, D., Peter, C., Salina Borello, E., & Panini, F. (2020). Pore structure characterization through path-finding and Lattice Boltzmann simulation. Advances in Water Resources, 141, 103609. https://doi.org/10.1016/j.advwatres.2020.103609

Contents

List of Tables

List of Figures

Chapter 1

Introduction

Technical applications such as primary production of oil and gas, Enhanced Oil Recovery, Underground Gas Storage, Underground Hydrogen Storage, CO_2 storage and geothermal systems require a thorough analysis, characterization and description of fluid flow phenomena in underground porous media [1–6].

Porous media can be defined as materials containing voids (pores) and solid (matrix) [7]. Ceramics, filter papers, textiles, biological tissues and natural porous media such as soils and rocks are some examples of porous media [7]. In particular, porous media present in underground reservoirs have pore sizes in the order of magnitude from νm to μm [8]. These media also present solid grains varying over a wide range of sizes and shapes, and the pore space is typically filled by one or more fluids [7]. At least some of the pores should be interconnected (effective pore space) [7]. Furthermore, underground porous media are subjected to relatively high pressure and high temperature mainly depending on the depth of the reservoir. Usually, reservoir rocks are sedimentary rocks of clastic origin, such as sandstone, and rocks of chemical origin, such as carbonate [9]. Among these rocks, 60% of the reservoir rocks are sandstone and 40% carbonate [10]. Sandstone rocks are composed mainly of silicate minerals [11], while carbonate rocks are composed by calcite ($CaCO_3$) or dolomite ($CaMg(CO_3)_2$) minerals, which precipitate from water [11].

It is essential to account for all the insight that can be gained from geology, geophysics, log interpretation, laboratory measurements for fluids PVT and rock properties characterization, well testing and reservoir engineering and to compare, combine, and properly integrate this knowledge in order to describe and understand in depth the behavior of reservoir dynamics [12–15]. Due to the complexity of geological formations, the uncertainty associated to the key parameters must be estimated and possibly mitigated by the acquisition of further information at all stages of reservoir life [16, 17]. The characterization and analysis of fluid flow phenomena in underground porous media are fundamental steps in the process that can contribute to maximizing the reservoir dynamic behavior by minimizing

uncertainties in the characterization of fluid-rock interaction parameters.

The accurate characterization of the pore space across several scales in heterogeneous porous media is a significant challenge in reservoir engineering [18]. In general, natural porous systems can be categorized over three different length scales [19]: (i) the pore-scale (or microscopic scale) at the pore level; (ii) the macroscopic scale (or macro-scale) at the core level; and (iii) the field-scale at the reservoir level. Rock properties and fluids dynamic behavior at the macro-scale and field-scale are strongly affected by the micro-geometrical features of the pore space [20]. In many cases, the flow mechanism can be understood from pore-scale phenomena, allowing predictions at the macro-scale, which can then be compared with experimental results [7]. Multiscale studies associated with pore network properties are increasingly used to improve the understanding of macro-scale parameters such as porosity, absolute and relative permeability and capillary pressure curves [21–24]. Macroscopic properties can be obtained by averaging pore-scale properties over a Representative Elementary Volume (REV), where the REV-scale is the scale above which the heterogeneities at smaller scales do not affect these macroscopic properties [23]. This process of averaging properties to the larger scales is called upscaling (Fig. 1.1).

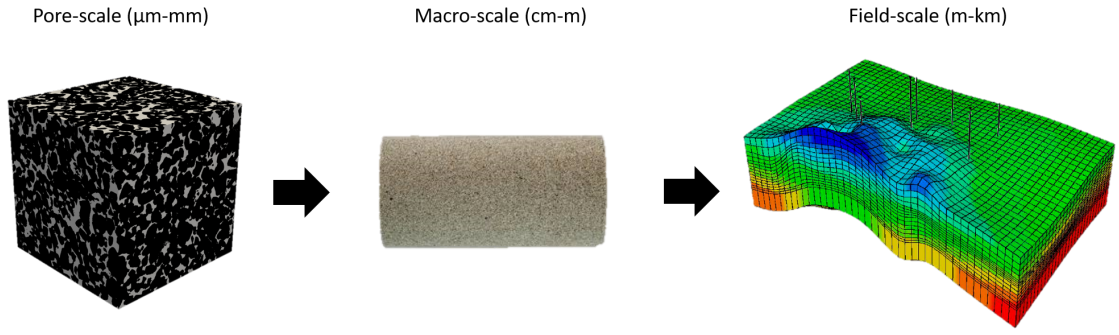

Figure 1.1: Multiscale nature of reservoir rocks. On the left image, the pore-scale (between μm and mm) representation of a sandstone rock is obtained by micro-CT scanning [25]. On the center image, a rock sample is showed as representative of the macro-scale (from cm to m), which is the scale at which laboratory experiments are conducted [26]. On the right image, a portion of a reservoir is represented to show the field-scale (from m to km), which is considered in reservoir models [27]. At different scales, the same rock is studied using different techniques and different parameters. Physical phenomena that occur at larger scales depend on physical phenomena that occur at smaller scales.

In the last twenty years, important advances in imaging techniques and high performance computing have contributed to the development of pore-scale modeling as a reliable technique for predicting averaged macroscopic properties of porous media [28]. In fact, X-ray micro-computed tomography (micro-CT) [29] or Focused

Ion Beam-Scanning Electron Microscopy (FIB-SEM) [30] can reconstruct and visualize a three-dimensional porous medium with a sufficiently high resolution as to identify grains and pores [31, 32]. Thanks to these techniques, a realistic representation of the reservoir rock is obtained, and it can be used as input for further analyses of pore space characteristics [33, 34].

1.1 Aim and outline

The aim of this work is to propose a methodology based on geometrical analysis and hydrodynamic modeling at the pore-scale directly on images of rocks in order to estimate microscopic and textural parameters that influence the fluid flow behavior in the pore space. The geometrical analysis is based on the application of the A* algorithm to find geometrical paths between inlet and outlet points in 2D and 3D rock images. Hydrodynamic simulation is performed using the Lattice Boltzmann Method (LBM) in 2D geometries and the Finite Volume Method (FVM) in 3D geometries. The LBM is implemented using the single relaxation time model for the collision operator. For hydrodynamic simulations in 3D rock images, the open source code OpenFOAM is used and pressure-velocity coupling algorithms are adopted to solve the Navier-Stokes equations directly in the pore space. Finally, the results obtained with the geometrical and hydrodynamic approaches on 2D and 3D rock images are compared and discussed. 2D rock images are taken from literature, while 3D rock images are generated by using the Quartet Structure Generation Set (QSGS) algorithm.

The thesis is articulated as follows. Chapter 2 discusses the image analysis techniques to extract the porous domain from rock images, the REV concept and the main parameters for porous media characterization. In Chapter 3, the geometrical analysis of the pore space based on the A* algorithm is presented. Chapter 4 describes the pore-scale hydrodynamic modeling. After a review of the state of the art, the equations of fluid motion are derived and then two numerical methods used to solve them are presented: the Lattice Boltzmann Method and the Finite Volume Method. In Chapter 5, the whole methodology based on the geometrical analysis and hydrodynamic modeling is applied to 2D images of rocks. In Chapter 6, the methodology is extended to 3D images of rocks generated with the QSGS algorithm. Chapter 7 summarizes the findings of this investigation and discusses its main application.

Chapter 2

Pore-scale characterization

Nowadays, advanced imaging techniques such as micro-CT, Scanning Electron Microscopy (SEM) and FIB-SEM are widely used to acquire 2D and 3D images of rock samples with a resolution in the order of micrometers [33–36]. Once the rock image is obtained, specific algorithms can be used to extract information of the pore structure and to characterize the internal pore space [37, 38]. Moreover, powerful computational fluid dynamics (CFD) methods can be employed for solving fluid flow equations directly in the pore space [24, 39, 40].

2.1 Rock imaging

A complete rock imaging procedure is preformed by two main steps: image acquisition and processing [34, 41, 42]. In this section, these two steps are addressed.

The first attempt to acquire images of a solid object with a micrometer resolution using X-ray computed tomography was in 1982 by Elliott & Dover [43], who achieved a resolution of 15 μm. Later, in 1987 Flannery *et al.* [44] obtained images of porous rocks with a resolution of 1 μm, and since then the technology to acquire and process images have been extremely improved [8]. The technique of using X-ray computed tomography for imaging small objects with micrometer resolution is called X-ray computed-micro tomography or micro-CT (or μCT) [45]. Using micro-CT, it is possible to obtain 3D images of the internal structure of porous media in a non-destructive way by mapping the X-ray attenuation (or absorption) through the sample [34]. Most of the geometrical properties of the pore structure can be determined using micro-CT and the analysis of micro-CT images has been widely used for studying the pore space in different types of rock [34]. The amount of attenuation depends on the density, the atomic number of the material and the energy of X-ray [46]. In X-ray micro-CT, the cross section of a rock sample is reconstructed from projection data obtained by passing a series of X-rays through a the rock and measuring the attenuation of these rays using

detectors placed downstream the sample [21]. The X-ray attenuation coefficients of the sample are measured at different angles and their values are represented in images as pixels (in 2D images) and voxels (in 3D images) [21]. This technique is suitable for rock samples because there is a clear contrast between the rock matrix, which attenuates X-rays strongly, and the pore space, which is more transparent to X-rays; this allows us to distinguish easily between solid rock and pore space [8]. The final output is a set of grey scale images. In Fig. 2.1.a, two examples of rock images with different resolution obtained with micro-CT are showed.

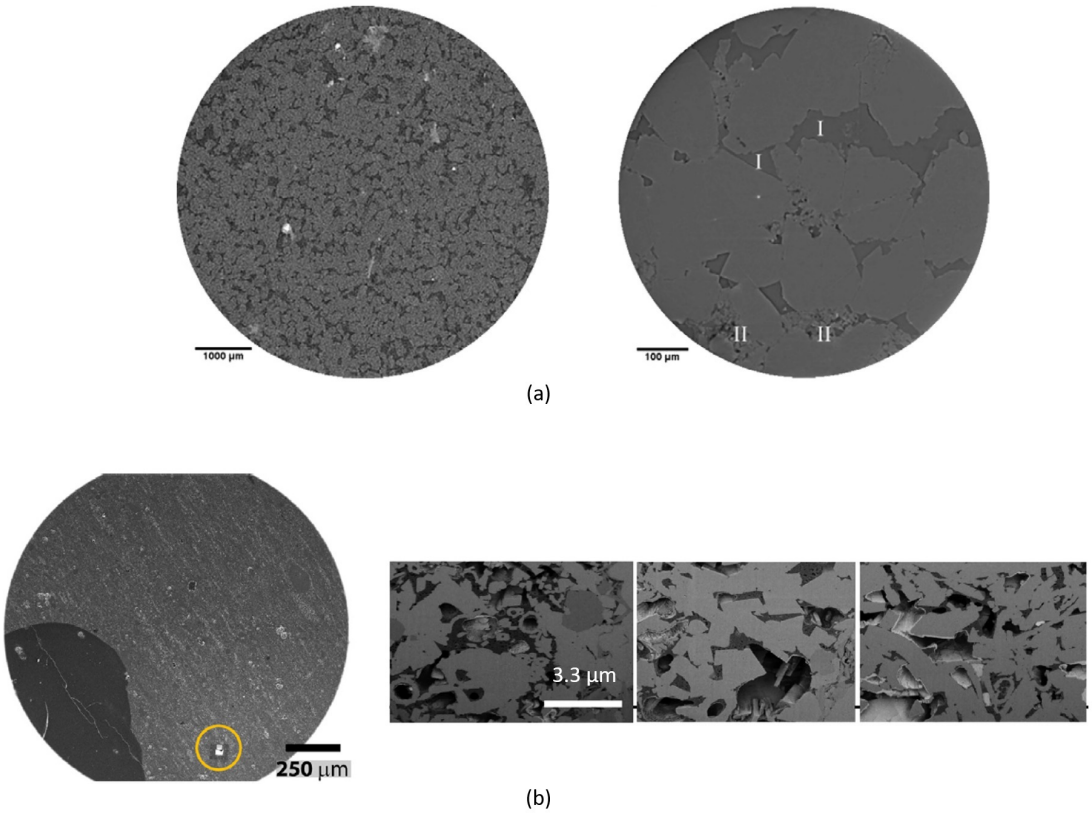

Figure 2.1: a) Example of micro-CT images of Berea sandstone with resolutions of 0.35 μm (left) and 12.7 μm (right); darker gray sections represent pores; on the left image, the roman numbers I and II refer to larger and smaller pores respectively [36]. b) Example of SEM image of a shale sample (left) and FIB-SEM images of the selected side (right) [30].

Besides micro-CT, SEM techniques can be used to acquire sample images both in 2D (using standard methods) and in 3D by taking several slides in a sample (FIB-SEM technique) [8]. However, FIB-SEM is a destructive technique (material is removed by a beam of ions) and therefore the sample cannot be used for fluid flow experiments [8, 35]. The advantage of FIB-SEM over micro-CT is the higher

resolution in the order of nanometers and it can be used for studying micro-porosity, rocks with nano-pores and organic material [30, 35]. Examples of rock images obtained with SEM and FIB-SEM techniques are showed in Fig. 2.1.b.

In Fig. 2.2, the voxel resolutions of images obtained with micro-CT and FIB-SEM are showed. It is visible that when a resolution in the order of nanometers is required, FIB-SEM should be used. On the other hand, when a resolution in the order of micromters is acceptable, images obtained with micro-CT can be used. A detailed description of micro-CT and FIB-SEM techniques is reported in Wildenschild & Sheppard [29] and Kelly *et al.* [30].

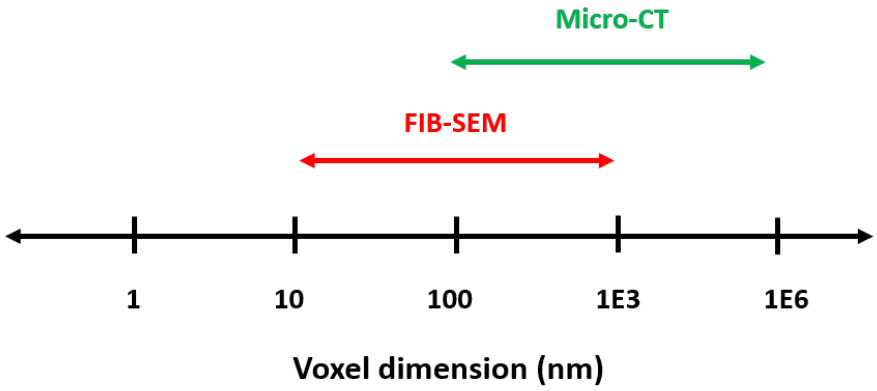

Figure 2.2: Resolutions of modern image acquisition methods are showed as an approximate range. The range of activity of FIB-SEM is around 10 to 1000 nanometers. The range of activity of micro-CT is from 100 nm to 1 mm [42].

.

The raw images obtained from the CT scanner or FIB-SEM cannot be used directly for pore-scale analysis and it is necessary to apply some image processing techniques in order to improve the quality of the images [34]. First of all, the image contrast can be enhanced by applying a brightness/contrast filter, which stretch the grey-scale histograms [34]. Then, another important step is to reduce the noise in the micro-CT images by applying an image filtering algorithm such as gaussian filter, median filter and non-local means filter [41]; Gong *et al.* [34] and Vlahinic *et al.* [41] suggested to use non-local means filter. In Fig. 2.3, the resulting images after contrast enhancement and noise filtering are showed.

The resulting image can be segmented based on the grey-scale contrast and transformed into a binary image with 1 representing the solid matrix and 0 the pore space [34, 41]. One of the most used segmentation methods is thresholding [34, 45]. The thresholding method converts a gray-level image into a binary image based on a threshold value. One threshold value is used for the whole image and typically the threshold value is selected based on the histogram of the image [21], as shown in Fig. 2.4. The threshold value is important for the final result of the

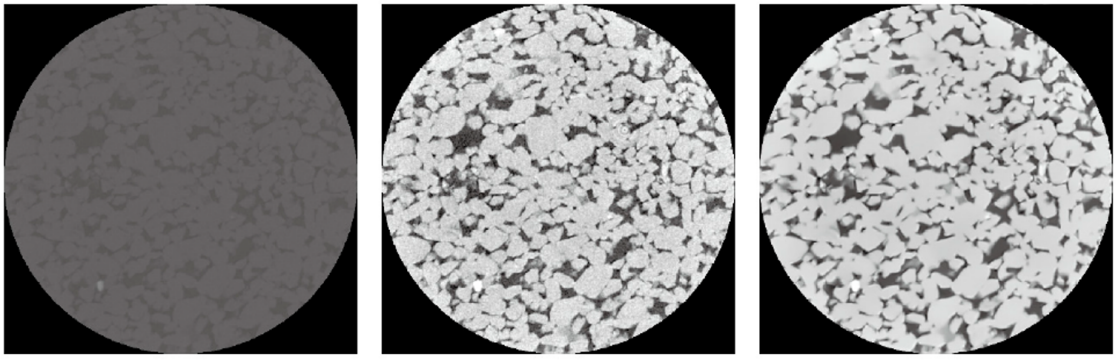

Figure 2.3: a) Original micro-CT image; b) image after brightness/contrast filtering; c) image after noise removal by non-local means filter [34].

pore geometry, therefore it should be chosen carefully [34, 36].

For a complete review on image processing techniques from micro-CT and FIB-SEM images of porous media refer to Kelly *et al.* [30], Shah *et al.* [40], Vlahinic *et al.* [41], and Hashemi *et al.* [45].

2.2 REV concept

Macroscopic fluid flow through porous media is described by defining an average pressure and velocity over a representative elementary volume (REV). Bear [7] defined the REV through the concept of porosity as the smallest volume of porous medium at the continuum scale for which the porosity does not change for volumes larger than the REV. This volume must be enough larger than the size of a single pore to permit the average required in the continuum concept. As REV concepts and averaging procedures look like simple and relatively straightforward in theory, in practice the REV size is not easy to estimate. In fact, its size is dependent on the property that we wish to average and in most cases is not the same. Macroscopic properties are distinguished into static properties such as porosity, and transport properties such as permeability. Transport properties, unlike static properties, are influenced by the interconnections of pores and a larger REV is necessary for the average [39, 47, 48] and this becomes even more evident when multiphase flow occurs [49].

Mostaghimi *et al.* [39] studied the existence of a REV at the pore-scale and compared its size for sandstone and carbonate rocks. They showed that the permeability of Berea sandstone measured experimentally on a core was 0.7 D, which was half of the value computed by numerical simulation. This was due to the influence of heterogeneity, in fact the size of micro-CT sample is 1.5 mm and the core sample

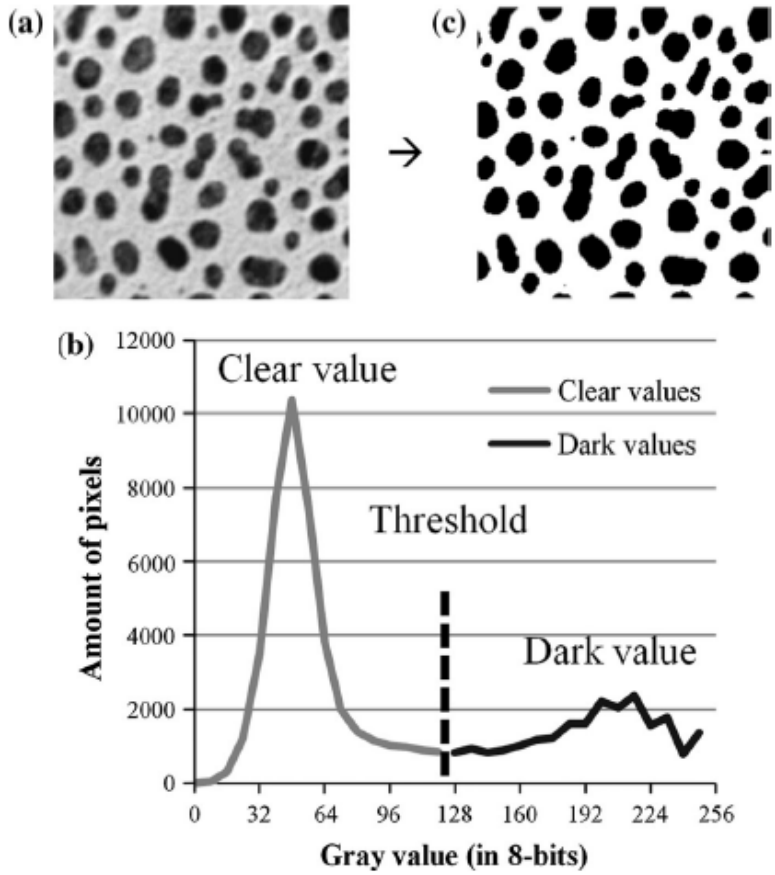

Figure 2.4: a) Grey-scale image; b) threshold value on the histogram; c) segmented binary image [45].

has a length of 7 cm, which is a large difference. This effect is even more higher for carbonates. This analysis showed that the size of REV based on permeability can be up to two times larger than the size of REV based on porosity [39]. Okabe & Oseto [50] showed through lattice Boltzmann simulation that images larger than 1.2 mm can be considered a REV for Berea sandstone in terms of porosity and permeability. In multiphase fluid flow, the relationship between the fluid dynamics within the pores of the rocks and their averaged values still remains an unresolved question [51]. It is not clear how heterogeneity in multiphase flow properties at the pore-scale should be accounted for in continuum models. The REV side length for capillary pressure curves is about 1.25 mm for both heterogeneous and homogeneous samples [51]. In contrast, the REV for saturation varies between 1.5 and 5.4 mm [51]. Even if this discussion still remains a fervent research topic, however, in many practical cases a detailed analysis on the REV size is not possible and only one REV is defined based on porosity and all properties are averaged over this REV

[49]. In general, in order to recover macroscopic quantities it is necessary to have a sample that is at least 10–20 pores in order to provide a reasonable average [8].

Once the appropriate REV is defined, the average quantity of a generic microscopic property ψ is evaluated by the averaging theorem [52]:

$$\langle \psi \rangle = \frac{1}{V} \int_V \psi \, dV, \tag{2.1}$$

where $\psi = 0$ on the solid grains and $\psi \neq 0$ in the pore space. For example, porosity is evaluated over a REV as:

$$\phi = \frac{1}{V} \int_V f \, dV, \tag{2.2}$$

where $f = 1$ in pore space and zero elsewhere. Eq. 2.2 reduces then to $\phi = \frac{V_f}{V}$, which is the common definition of porosity.

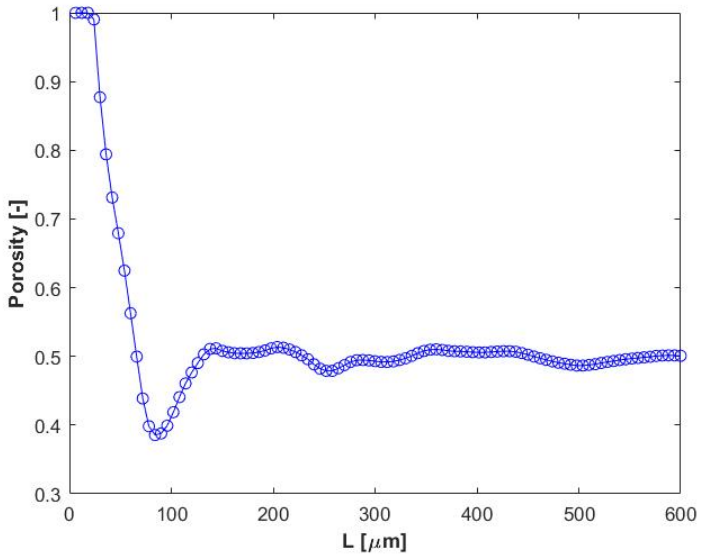

Figure 2.5: Example of porosity variation with respect the length scale. L $\approx$ 250 μm can be considered as the REV length scale because at larger scales porosity is approximately constant around 0.5.

2.3 Porous media characterization

At the macro-scale, the fluid flow is modeled by averaging the microscopic continuity and momentum equations over a REV (Eq. 2.1) and the porous medium is parameterized mainly by porosity and permeability [7, 53, 54]; the fundamental

equation of fluid motion in porous media under the assumption of small Reynolds numbers is the Darcy's equation [7]:

$$\mathbf{U}_D = -\frac{\mathbf{k}}{\mu}\nabla p, \tag{2.3}$$

where $\mathbf{U}_D$ is the Darcy's velocity, $\mathbf{k}$ is the permeability tensor, μ the dynamic viscosity and ∇p the pressure gradient. Darcy's velocity can be upscaled applying Eq. 2.1 as:

$$\mathbf{U}_D = \frac{1}{V}\int_V \mathbf{u}\, dV. \tag{2.4}$$

where $\mathbf{u}$ is the local velocity (i.e. pore-scale fluid velocity inside the pore channels). Inverting Eq. 2.3, the permeability tensor can be computed. In terms of flow rate q, the Darcy's law is written multiplying the Darcy's velocity by the cross section A of the porous medium:

$$q = -A\frac{k}{\mu}\nabla p. \tag{2.5}$$

Natural porous media are extremely complex systems characterized by tortuous structure and significant variability of grains and pores size [54]. Tortuosity (τ) was introduced by Carman [55] to address the tortuous fluid paths in the pore space. Two main types of tortuosity are defined in the literature: geometrical tortuosity (τ_g), calculated as the shortest length between inlet and outlet avoiding the solid obstacles divided by the distance between inlet and outlet Clennell [56], and hydraulic tortuosity (τ_h), calculated as the effective fluid path length taken by the fluid divided by the length of the porous material measured along the flow direction Carman [55]. Mathematically, geometrical and hydraulic tortuosity are expressed respectively as:

$$\tau_g = \frac{L_{shortestPath}}{L} \tag{2.6}$$

and

$$\tau_h = \frac{L_{fluidPath}}{L}, \tag{2.7}$$

where L is the sample length in the flow direction.

For low porosity materials, a large part of the total pore space may be nonconducting [57]. The effective porosity ϕ_e is defined as the percentage of interconnected conductive pore space with respect to the bulk volume [58, 59]:

$$\phi_e = \frac{V_{flow}}{V_b}, \tag{2.8}$$

where V_{flow} is the conductive pore space and V_b is the bulk volume.

In the literature, some analytic expressions were introduced to link permeability to the pore structure as a function of porosity, effective porosity, tortuosity and/or

pore dimension ([55, 57, 60–62]). One of the most used expressions is the Kozeny-Carman equation [55, 62]

$$k = \frac{\phi r_H^2}{c_k \tau^2}, \tag{2.9}$$

where c_k is the Kozeny's constant and r_H is the hydraulic radius, which gives a measure of the average pore dimension and is defined as [7, 63]:

$$r_H = \phi \frac{V_b}{A_w} \tag{2.10}$$

where A_w is the wetted surface.

Furthermore, Berg [64] quantified the reduction in permeability due to the variation in pore cross-sectional area (A) along the pore channel length (L_p) by introducing the constriction factor (C):

$$C = \frac{1}{L_p^2} \int_0^{L_p} A\left(x\right)^2 dx \int_0^{L_p} \frac{1}{A\left(x\right)^2} dx. \tag{2.11}$$

The parameters described above can be estimated by a direct analysis of the pore space using binary images obtained from micro-CT, SEM or FIB-SEM techniques, as described in Section 2.1. In this work, two main approaches are presented and discussed: 1) a geometrical approach based on the direct analysis of the pore space image applying a path-finding algorithm called A*, and 2) an hydrodynamic approach based on the numerical solution of fluid flow equations (i.e. Navier-Stokes equations) directly into the pore space.

Chapter 3

Geometrical analysis of the pore space

Several authors discussed the geometrical analysis of the pore structure from 2D and 3D images of rocks. A common approach is to construct a network model of the pore space starting from a rock image. The idea behind this method is to construct a simplified geometrical representation of the pore space, preserving all the geometrical information needed to understand the fluid flow [8]. The simplification stays in representing the pore space as composed by pore bodies, usually spheres (wider regions), connected by pore throats (narrower regions). In order to distinguish between pore body and pore throat in a rock image, the maximal ball algorithm and image analysis techniques have been proposed [8, 65, 66]. In building network models, three geometrical parameters can be defined [67]: pore throat ratio, coordination number and shape factor. The pore throat ratio is defined as the ratio of the pore diameter to the throat diameter and it gives information about heterogeneity. The absolute permeability decreases with the increase of the pore throat ratio. The coordination number is the number of pore throats connected to a single pore body. It is an average number and calculated as the total number of throats divided by the total number of pore bodies and it usually oscillates between 2 and 6. Finally, the shape factor is defined as the pore sectional area over the squared sectional perimeter. Traditionally, pore bodies and pore throats were assumed to be spherical and cylindrical, but it was not a good approximation of the geometries of real pores. It was found that pores with a triangular shape have similar shape factor as measured for real porous systems and were able to reproduce the roughness and the flow in pore centers [68]. In fact, it is important to point out that in real systems the center of the pore is occupied by the non-wetting fluid and boundary layers of the wetting fluid form in the roughness of the pore. This phenomenon is well represented by the fluid residing in the corners of a triangle pore section. More information about network models can be found in Blunt [8].

Several computational techniques have been used to characterize the geometry of

the pore space. Comparison of three image processing algorithms (Mean Intercept Length, Erosion and Dilation, Watershed Segmentation) to estimate the grain-size distribution of porous rocks from binary 2D images was performed by Rabbani & Ayatollahi [38]. Lock *et al.* [69] developed a network model that allowed predictions of the permeability of consolidated sedimentary rocks, based on image analysis of sections of a rock core sample.

Lindquist *et al.* [37] introduced the use of the medial axis algorithm to analyze structure properties such as pore throat and pore body size distributions and geometric tortuosity of a 3D digitalized image. The medial axis (or skeleton) is formed by the series of points that are more distant from the solid surface. Using this method, the three-dimensional pore space topology is directly extracted. For porous media, the medial axis provides simple basic information about the geometry of the void space [21] and it is obtained directly on the binary image by applying a burn algorithm [37]. A major problem with this method is that it may contain dead ends, which are not representative of the fluid flow path. Al-Raoush & Madhoun [70] presented an algorithm for calculating geometric tortuosity from 3D X-ray tomography images of real rocks based on a guided search for connected paths utilizing the medial surface of the void space of a 3D segmented image.

Furthermore, Keller *et al.* [71] proposed a 3D graph representation to determine the spatial distribution of pore space geometrical properties. Ghanbarian *et al.* [54] proposed geometric tortuosity models based on concepts from finite-size scaling analysis and percolation theory.

Besides these methods, path-finding (or shortest-path) algorithms can be used for geometrical analysis of the pore space and the characterization of the microstructure. The first authors to introduce this method for porous media applications were Sun *et al.* [72], who used a shortest past approach based on the Dijkstra's algorithm to calculate the geometric tortuosity and connected porosity. Then, they applied a multiscale method approach to upscale the permeability. In this Section, we focus a methodology based on on the A* path-finding algorithm, which is more efficient than the Dijkstra's algorithm, to describe the pore structure of 2D and 3D binary images of rock samples. The aim of this research is to compute the parameters introduced in Section 2.3 using geometrical information of the pore space. The methodology for the geometrical characterization discussed in this Chapter was published in Viberti *et al.* [73], Panini *et al.* [74], and Salina Borello *et al.* [75].

3.1 A* algorithm

The A* algorithm is used to compute the shortest paths between each inlet-outlet pair [76–78]. The process is achieved by steps. Starting from an inlet location ($n = n_0$), at each step the algorithm expands the current node n by exploring all nodes n_i, called successors, in the proximity of n. For each successor (n_i), n is set

as the parent node and a cost function $c(n_i)$ is calculated as:

$$c(n_i) = g(n_i) + h(n_i), \tag{3.1}$$

where i indicates the i-th successor of n, $g(n_i)$ is the backward cost, i.e. the distance calculated over the incremental path already identified from the inlet to n_i, and $h(n_i)$ is the forward cost, i.e. a heuristic function representing the estimation of the cost to move from n_i to the target (outlet), as shown in Fig. 3.1. The Euclidean distance was adopted as forward cost $h(n_i)$. Then, the algorithm moves from node n to the node having the lowest cost among all explored and unexpanded nodes (i.e. nodes where the cost function has already been calculated and successors have not been explored yet). The calculation is repeated until the target point is reached. Then, the path is constructed backward from the target point to the inlet point by connecting the parent nodes.

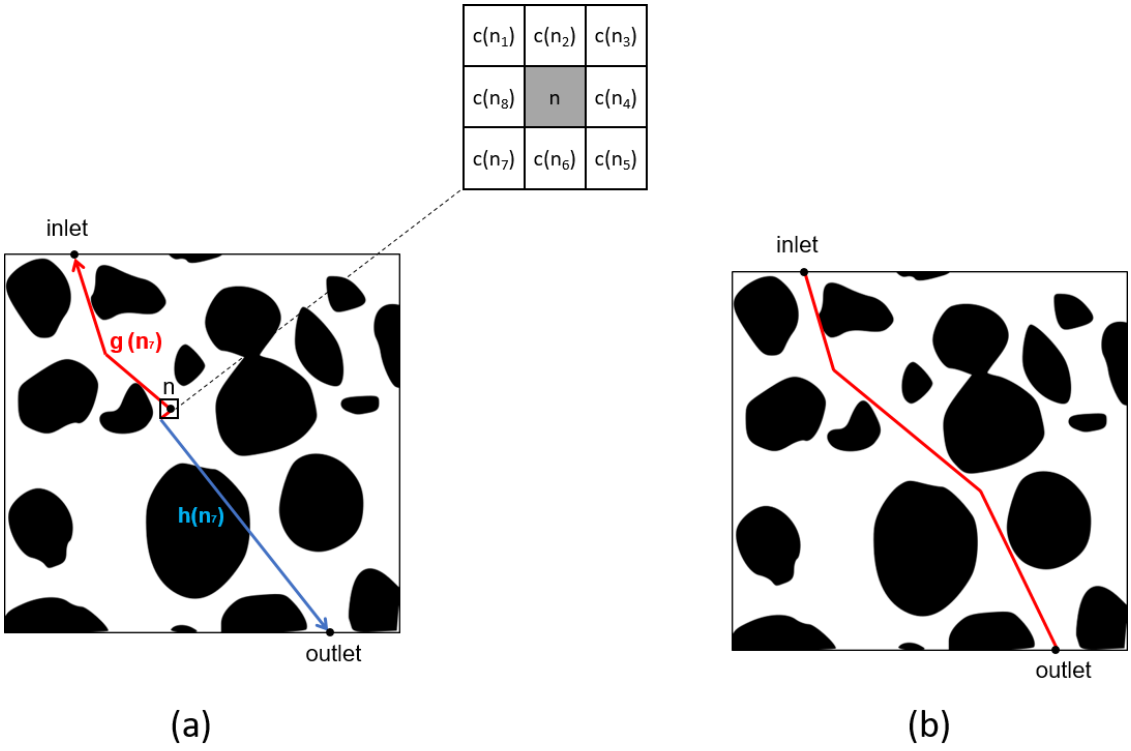

Figure 3.1: Qualitative representation of the A* cost-driving mechanism: a) cost function calculation where n represents the current path node. Cost functions $c(n_i)$ are calculated in the adjacent nodes from 1 to 8 (successors). $g(n_7)$ and $h(n_7)$ are respectively the backward and forward costs calculation of successor 7. (b) A* shortest path [75].

In the implementation, two lists of nodes are created (Fig. 3.2): the Open List, a structure that holds the explored nodes but not the expanded nodes (their

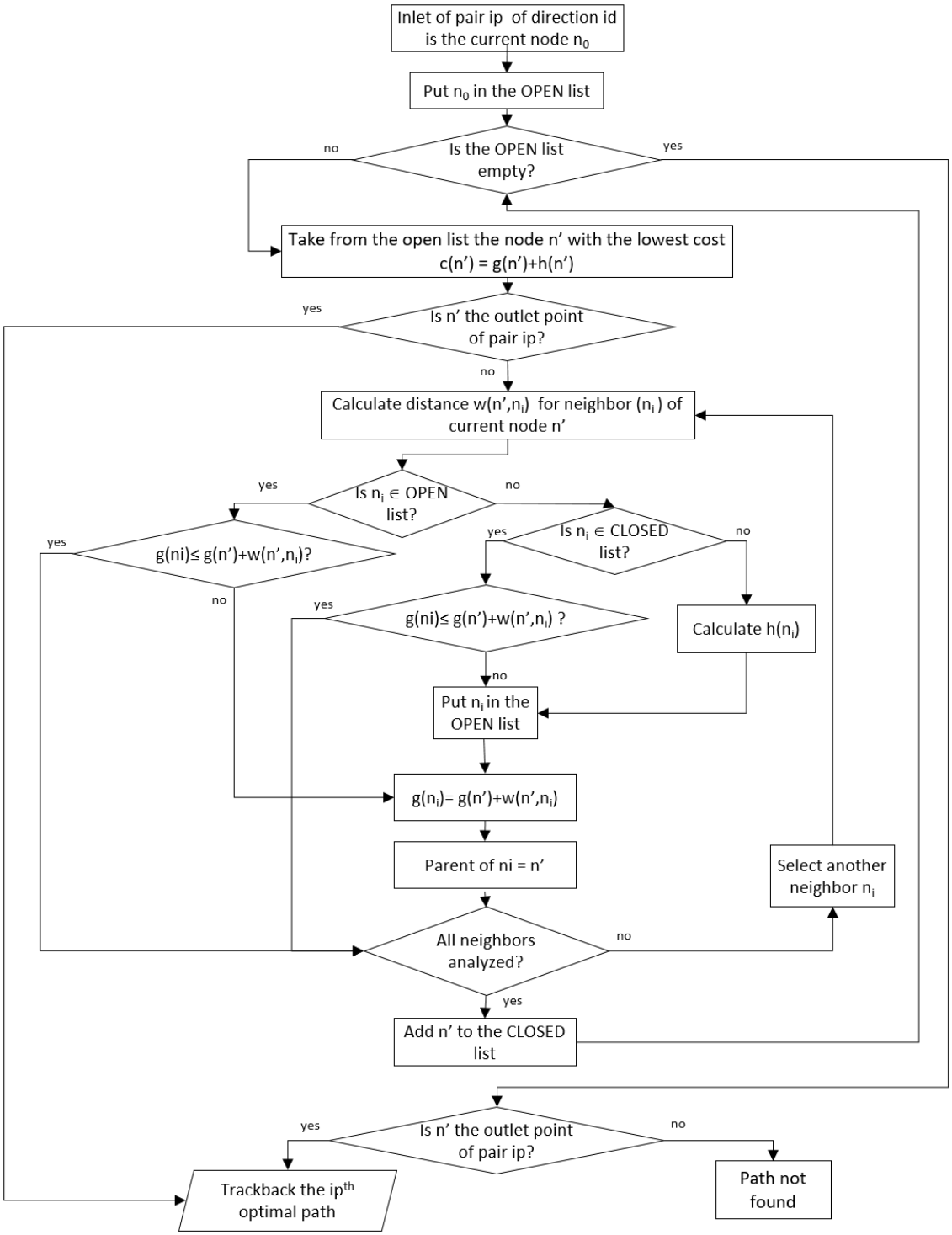

Figure 3.2: A* algorithm [75].

successors have not been explored yet) and the Closed List, a structure that contains every expanded node (their successors have been explored already and stored in the Open List). The presence of obstacles (i.e. grains) might extend or interrupt the path development between the considered node and the target node. In such cases, the algorithm can go back to a promising parent node and expand another successor node to calculate alternative promising paths. In fact, for each explored node n_i the cost value $c(n_i)$, and its parent node n are stored. Additional algorithmic details are contained in Fig. 3.2.

The A* algorithm is complete and therefore the convergence is guaranteed on finite graphs [79]; this means that it will always find a path between inlet and outlet points if at least one exists, and it is guaranteed to terminate if there are no existing paths. Also, the solution is optimal if the heuristic function $h(n)$ is admissible and monotonic [79]. The Euclidean distance is admissible and monotonic because it never overestimates the cost to the target point and the total cost $c(n)$ of a successor is always greater than (or equal to) its parent cost.

The weakness of the A* search is that all explored nodes are kept in memory. The space complexity of the A* is proportional to the number of explored nodes $O(b^d)$ [79], where d is called depth of the solution and refers to number of nodes of the shortest path, and b is called branching factor, which refers to the average number of successors expanded at each state [79]. The branching factor depends on the effectiveness of the heuristic function because more accurate estimates of $h(n)$ decrease the number of times that the algorithm should go back to explore another node. In principle, b should be equal to 1.

The time complexity of the A* is also $O(b^d)$ [79]. Furthermore, the overall time complexity of path searching with the A* algorithm in a porous medium depends on the number of inlet/outlet pairs chosen in the three (or two) directions. Considering the same number of inlet (n_{in}) and outlet (n_{out}) points in each x, y and z direction, the overall time complexity is $O((n_{in}\, n_{out})^3 b^d)$, where d increases when the sample dimension or the image resolution increase. Also, the parameters d and b depends on the complexity of the porous geometry and the connecting distance c_d, which determines the number of successors and directions explored, as shown in Fig. 3.3. In this work, $c_d = 1$ was adopted, which in 2D corresponds to the exploration of 8 successors nodes and in 3D 26 successor nodes. From the point of view of the overall amount of explored nodes, there is no significant difference between $c_d = 1$ and $c_d = 3$, as shown in Fig. 3.4.a. This can be explained because using $c_d = 1$ an optimal path with more nodes is found (Fig. 3.4.b), and with $c_d = 3$ more nodes are explored (Fig. 3.4.c). Finally, $c_d = 1$ is advantageous in porous media because the path edge never crosses the solid grain but it always lies in the pore space.

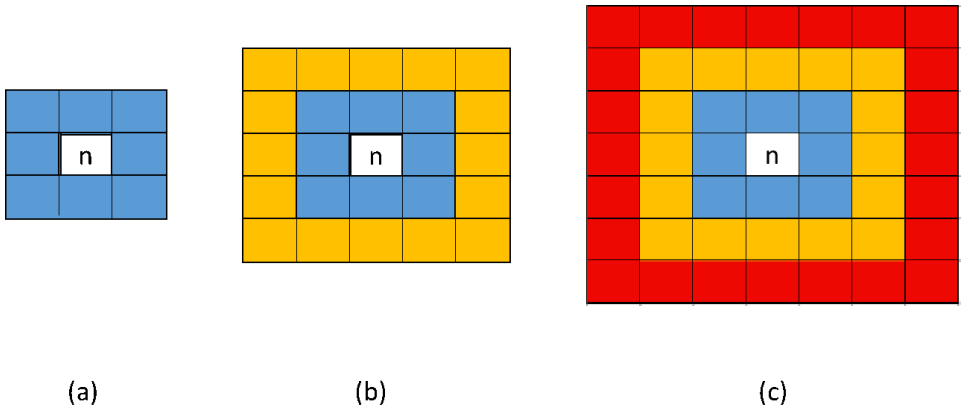

Figure 3.3: Successors construction for the current node n considering three different connecting distances: a) $c_d = 1$, b) $c_d = 2$ and c) $c_d = 3$ [75].

3.2 Estimate of geometrical parameters

The aim of this Section is to propose a geometrical approach based on the application of the A* algorithm to estimate pore-scale parameters of rock images. First of all, the geometrical approach was applied to 2D images of rocks and then integrated and extended to analyze 3D rock images.

The A* algorithm described in Section 3.1 was used to analyze the pore structure by finding the shortest paths connecting sets of inlet and outlet points, called n_{in} and n_{out} respectively, in 2D and 3D pore-scale binary images of rocks.

First of all, along the geometrical paths, the local pore size r_p is estimated. In 2D geometries, the pore size is calculated as the distance between the pore walls orthogonal to to the local path direction in each path node, as represented in Fig. 3.5. In 3D cases, the problem is more complicated. Along the paths identified by the A*, at the point $P_i = (x_i, y_i, z_i)$, the path direction is calculated as the vector v_i connecting P_i and the adjacent point P_{i+1}, i.e. $v_i = (x_{i+1} - x_i, y_{i+1} - y_i, z_{i+1} - z_i)$. The corresponding unit vector $\widehat{v_i} = (a, b, c)$ is calculated dividing v_i by the module $|v_i|$. In order to reduce the computational cost, a finite number of possible directions were considered: 1) 3 main directions x, y, z; 2) 6 directions at 45° belonging to xy, xz and yz planes; 3) 4 directions in the xyz space having equal components. Then, $\widehat{v_i}$ is associated to the closest vector in the discretized set not considering the sign. Successively, the orthogonal plane at P_i is calculated as:

$$a\,(x - x_i) + b\,(y - y_i) + c\,(z - z_i) = 0. \tag{3.2}$$

Two mutual orthogonal directions n_1 and n_2 belonging to the plane are chosen to calculate the pore sizes d_1 and d_2; d_1 and d_2 are calculated from P_i along n_1 and n_2 until the pore walls are reached (Fig. 3.6). The pore radius r_p is evaluated as the

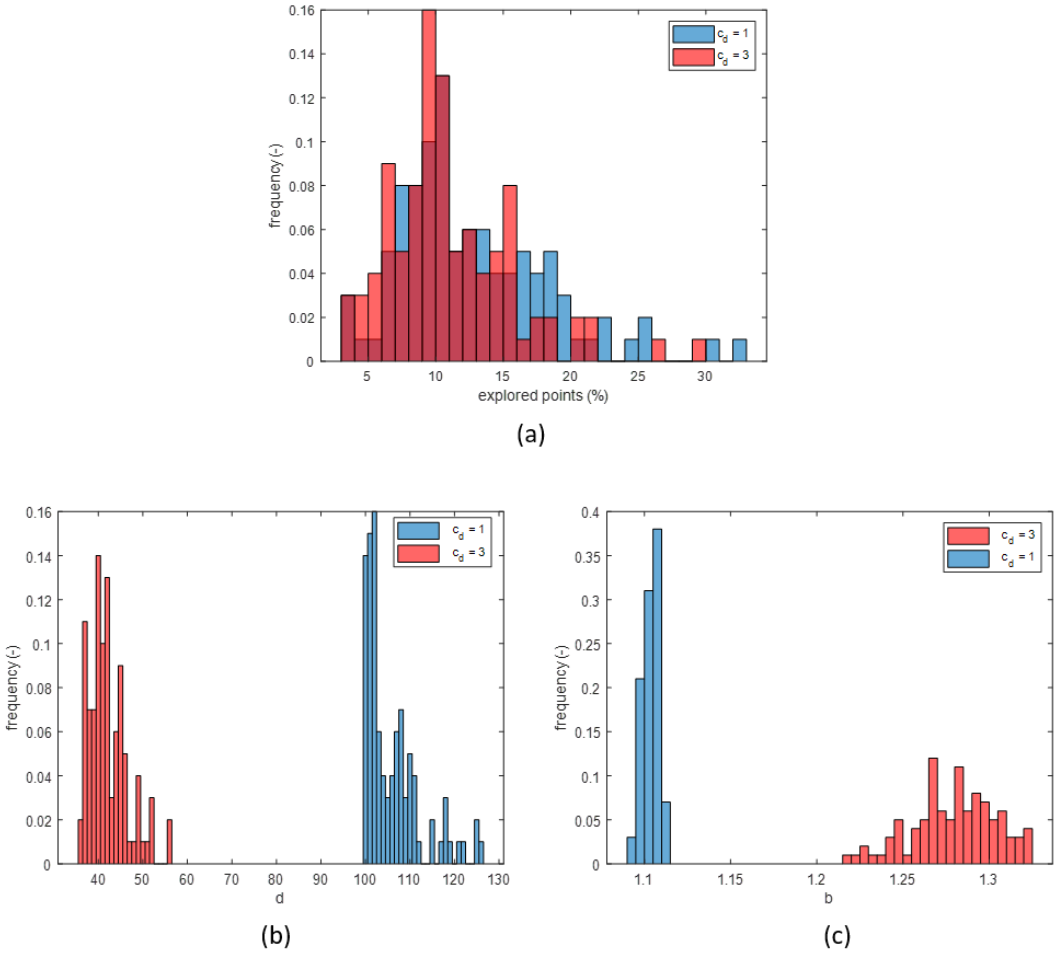

Figure 3.4: Example of analysis of the effect of the connectivity distance on: a) the amount of explored nodes, b) the obtained path depth and c) the branching factor [75].

radius of an equivalent circle having area equal to the ellipse of diameter d_1 and d_2:

$$r_p = \frac{1}{2}\sqrt{d_1 d_2}. \tag{3.3}$$

The information obtained by this methodology can be used to characterize the porous medium in terms of representative pore radius, tortuosity, effective porosity, constriction factor and permeability. All these parameters can be calculated in all the principal directions x, y and z. In this way, directional differences in the parameters can be highlighted.

The geometrical tortuosity $\tau_{g,i}$ in the i direction was calculated by [54, 80, 81]:

$$\tau_{g,i} = \frac{\langle L_{sh,i} \rangle}{L_i} \quad \text{where} \quad i = x, y, z \tag{3.4}$$

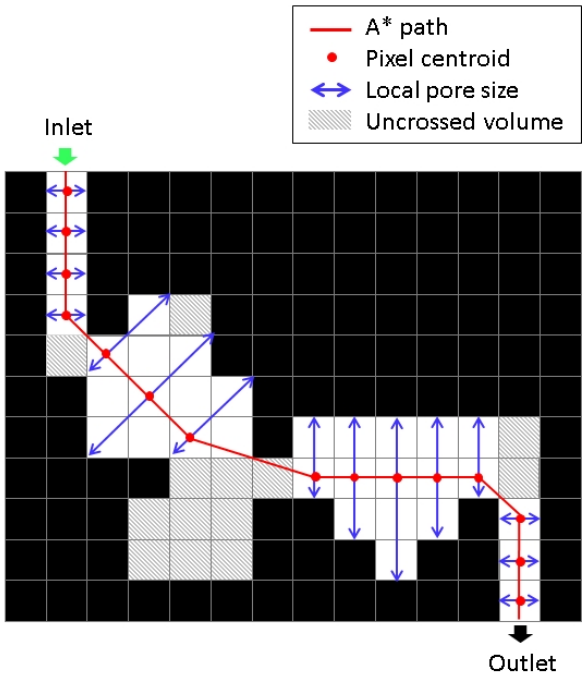

Figure 3.5: Schematic representation of the pore size and effective porosity estimates in 2D binary images [73].

and where $\langle L_{sh,i} \rangle$ is calculated as the average of the shortest path lengths calculated using the A* algorithm and L_i is the length of the sample in i direction.

In order to identify the interconnected pore space, a geometrical calculation of the effective porosity using the geometrical paths is proposed:

$$\phi_{e,i} = \frac{N_{pp,i}}{N_{px}} \quad \text{where} \quad i = x, y, z \tag{3.5}$$

where $N_{pp,i}$ is the number of image pixels belonging to the portion of pore channels crossed by a geometrical path and N_{px} the total number of image pixels. To this end, for each pathway, all pixels comprised in the pore section orthogonal to the local path direction were considered (see Fig. 3.5). The total effective porosity ϕ_{eg} was then calculated merging the identified cells contributing to the flow in i direction.

In order to estimate the permeability, the Kozeny-Carman equation (Eq. 2.9) was used. Starting from the approach proposed by Mauran *et al.* [82], the modified expression of the Kozeny-Carman equation based on geometrical information $k_{g,i}$ and taking into account for geometrical effective porosity and tortuosity is

$$k_{g,i} = \frac{\phi_{eg,i}\, r_i^2}{c_k\, \tau_{g,i}^2} \quad \text{where} \quad i = x, y, z \tag{3.6}$$

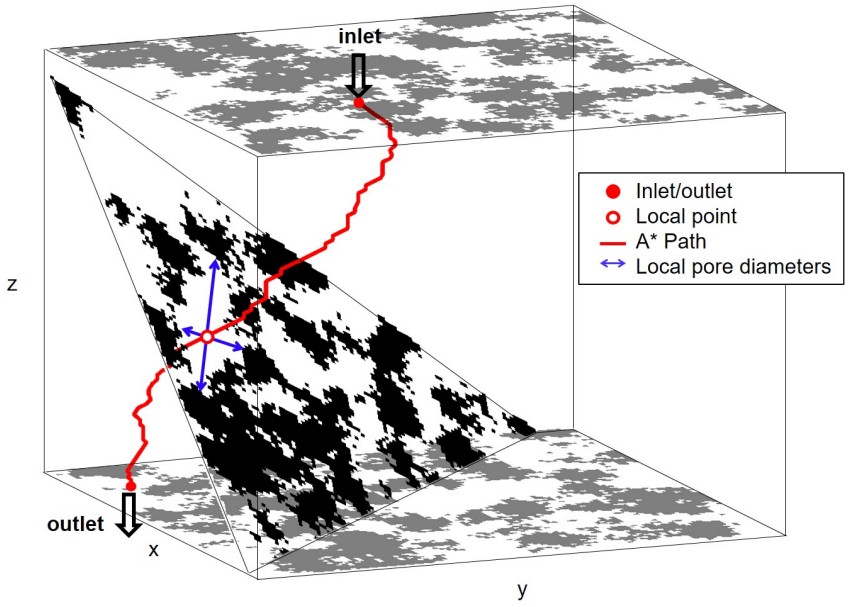

Figure 3.6: Schematic representation of the pore size estimate using the A* algorithm in 3D binary images. The shortest path between an inlet and outlet point found by the A* is represented in red [75].

where c_k the Kozeny-Carman coefficient; the effective porosity $\phi_{eg,i}$, geometrical tortuosity $\tau_{g,i}$ and representative pore radius r_i are calculated by analyzing all the geometrical paths individuated. The representative radius r_i is a sensitive choice and since the pore radius is often characterized by a multimodal distribution [83, 84], the pore radius data are fitted with a kernel distribution and the mode value is extracted. Since $\tau_{g,i}$ (Eq. 3.4), $\phi_{eg,i}$ (Eq. 4.147) and r_i are calculated by using the geometrical approach, the calculation of permeability (Eq. 3.6) is obtained by a purely geometrical analysis of the porous medium.

The Kozeny-Carman coefficient is a dimensionless empirical geometrical parameter in the range of 4-40, which depends on the morphology of the porous medium and on the shape of the pores [85]. For well-structured porous media $c_k = 5$ is an acceptable value [7]; however, for random porous media, c_k is generally determined by back-calculation of Eq. 2.9 [58, 82]. For isotropic cases, it was assumed $c_k = 5.8$, as obtained in Koponen *et al.* [58] for an isotropic porous medium constituted by randomly distributed freely overlapping squares. Conversely, for anisotropic cases, a different value should be considered, due to different pore geometry. As a consequence, for anisotropic or heterogeneous cases, c_k should be obtained by back-calculation. The estimate of c_k in anisotropic rocks is discussed in Chapter 6.

Another parameter that can be estimated with the geometrical approach is the pore constriction factor C (Eq. 2.11), which represents an average of the variation of the cross-sectional area along the path. When the pore constriction increases, the permeability decreases. In 3D, by approximating every single geometrical path in the i direction with a finite number of steps (n_p), one for each crossed pixel, and the local pore cross-section normal to the flow with a circle of equivalent radius r_e, Eq. 2.11 becomes:

$$\mathrm{C}_i = \frac{1}{n_p^2} \sum_{ip=1}^{np} r_{e,ip}(x,y,z)^4 \sum \frac{1}{r_{e,ip}(x,y,z)^4} \quad \text{where} \quad i = x, y, z. \tag{3.7}$$

The mode $\bar{\mathrm{C}}_i$ of constriction distribution is taken as a representative constriction factor for i direction.

The whole procedure designed and implemented for the geometrical characterization of rocks from 2D and 3D binary images is showed in Fig. 3.7.

Finally, the hydraulic radius r_H (Eq. 2.10) is calculated both is 2D and 3D geometries. For the calculation of r_H in 3D, the wetted area A_w is computed with the open-source software ParaView on the 3D mesh of the solid grains by using the Integrate Variables filter, which computes the area of each mesh polygon and then sums them. In 2D, Eq. 2.10 becomes:

$$r_{H,2D} = \phi_{2D} \frac{A_b}{P_w}, \tag{3.8}$$

where ϕ_{2D} is the porosity of the 2D rock section, A_b is the bulk area of the sample and P_w is the wetted perimeter, i.e. the interface between grains and void. P_w was calculated from the binary images using the Image Processing Toolbox of Matlab [86].

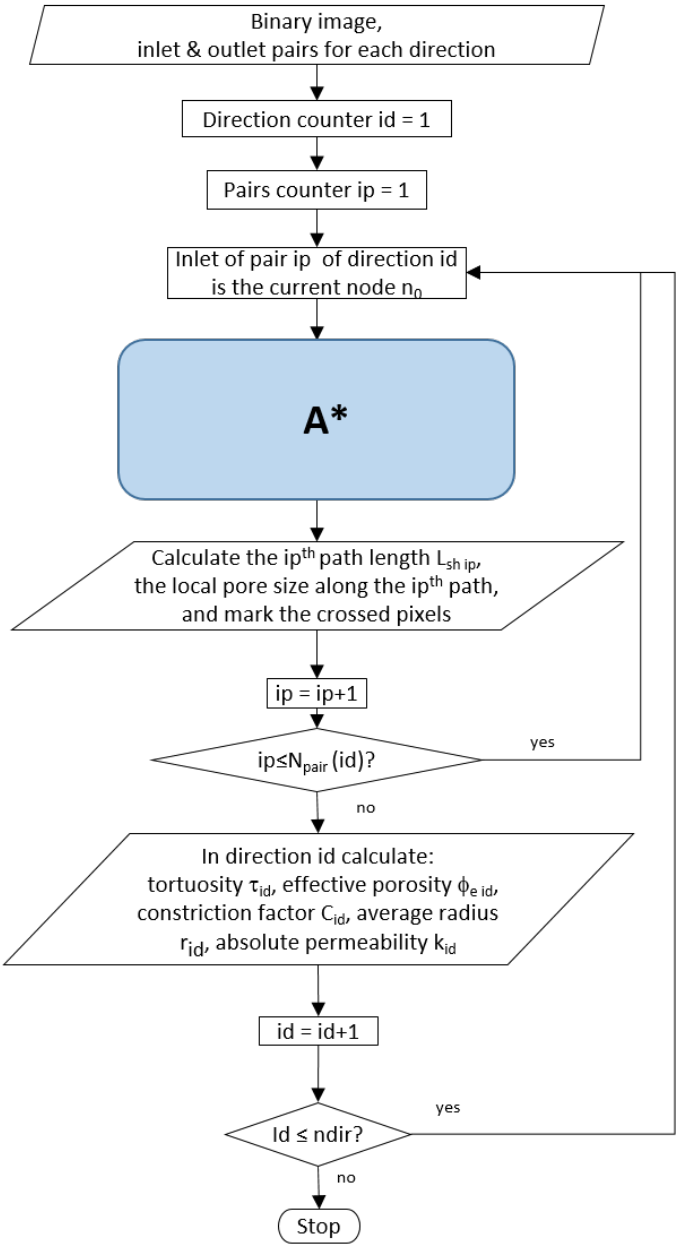

Figure 3.7: Geometrical characterization procedure [75].

Chapter 4

Pore-scale hydrodynamic modeling

In order to compute transport properties in porous media such as hydraulic tortuosity, absolute permeability, relative permeability, capillary pressure, identify pore-scale phenomena such as snap-off and water bypass, and visualize displacement patterns such as piston-like and viscous fingering, hydrodynamic numerical simulation at the pore-scale can be considered as a valid complementary tool to laboratory tests. Two different approaches can be identified: pore-network modeling (PNM), where simplified flow equations are solved in an equivalent geometry extracted from the real geometry, and direct numerical simulations (DNS), where the flow equations are directly solved in the pore space. This work focuses on the DSN.

First of all, a review of the state of the art of fluid flow simulation at the pore-scale is presented and the lattice Boltzmann method and Eulerian grid-based methods are introduced in order to solve the fluid flow directly in the pore space. Then, the fluid flow equations at the pore-scale, i.e. Navier-Stokes equations, are derived. Finally, the lattice Boltzmann method and the Finite Volume method are presented.

4.1 Literature review

First introduced in 1956 by Fatt [87], the PNM has earned popularity in the last thirty years for simulating single-phase and multiphase fluid flow in porous media ([31, 68, 88, 89]). The main advantage of PNM is its geometrical simplicity and consequently computational efficiency. Therefore, PNM can be used to analyze porous media even at the centimeter scale. However, this simplification in the geometry can cause a lack in physical detail [23, 68]. For this reason, direct numerical simulation is preferred in many circumstances. More information about PNM can

be found in Blunt [8].

In hydrodynamic simulation, the fluid flow equations are numerically solved on a grid created discretizing directly the pore space obtained from binary images [31]. There are three main families of algorithms used for solving hydrodynamic equations: 1) the Lattice Boltzmann Method (LBM), which is based on kinetic theory; 2) smoothed particle hydrodynamics (SPH), which is a Lagrangian mesh free method; 3) Eulerian grid-based methods such finite difference (FDM), finite element (FEM) and finite volume (FVM) methods.

In this work, the LBM and Eulerian grid-based methods will be treated in more detail. More information about the application of SPH to fluid flow simulation in porous media can be found in Tartakovsky & Meakin [90], Tartakovsky *et al.* [91], Bandara *et al.* [92], and Kunz *et al.* [93]. An overall review about numerical methods for fluid flow simulation in porous media can be found in Meakin & Tartakovsky [94].

Among numerical methods to solve fluid flow equations, the Lattice Boltzmann Method is well suited to solve single-phase and multiphase fluid flow in complex geometries such as porous media [95–98]. The LBM belongs to the family of discrete mesoscopic computational methods and it is based on the simulation of collision and propagation of groups of particles on a grid. These groups of particles (also called populations) are mathematically described through a density distribution function (f_i). Populations propagate to the neighbor nodes along fixed directions and with fixed velocities, called lattice velocity $\mathbf{c}_i$. The solution of the Navier-Stokes equations,i.e. fluid pressure and velocities, can be recovered by taking the 0th and 1st moments of the density distribution function. The rules governing the collisions are designed such that the time-average motion of the particles is consistent with the macroscopic hydrodynamics. Collision rules constitutes a simplified mesoscopic kinetic model based on a Boltzmann-type equation that incorporate only the essential physics of microscopic or mesoscopic processes, avoiding following each particle as in molecular dynamics simulations [99]. Details of the LBM are presented in Section 4.3. Due to its particulate nature and local dynamics, the LBM has several advantages over other conventional CFD (Computational Fluid Dynamics) methods, especially in dealing with complex boundaries, incorporating of microscopic interactions, and parallelization of the algorithm [100]. The simplest implementation of the LBM adopts the single-relaxation time (SRT) approximation of the collision operator, called Bhatnagar-Gross-Krook model (BGK) [101]. More sophisticated models of the collision operator consider two-relaxation-time (TRT) and multi-relaxation-time (MRT) [98]. Comparison of SRT and MRT in porous media applications for permeability assessment was performed in 2D and 3D synthetic and real porous media by Pan *et al.* [102] and Eshghinejadfard *et al.* [103], who showed a dependency of permeability to viscosity when using SRT. However, Prestininzi *et al.* [104] showed that the SRT is capable of simulating fluid flow in porous media with adequate accuracy if the Knudsen number (defined as the ratio

between the molecular mean free path and the characteristic length at which macroscopic effects can be appreciated [105], and computed as $\mathrm{Kn} = \nu/(l\, c_s)$, where ν is the kinematic viscosity, l a pore characteristic length and c_s the sound speed [104]) is smaller than 10^{-2}, which is the proper region where the LBM is guaranteed to reproduce the hydrodynamics equations. The main drawback of the LBM is that it is memory demanding, making it difficult to be used in large porous domains. More details about this method and its implementation in this work are reported in Section 4.3.

The lattice Boltzmann method can also be used to simulate multiphase flow. Four main models are available: the color-gradient model proposed by Gunstensen *et al.* [106], the Shan-Chen (SC) model (Shan & Chen [107]), the free energy model proposed by Swift *et al.* [108] and the interface tracking model (HCZ model) proposed by He *et al.* [109]. In their primitive forms these methods suffered of numerical problems and they were incapable to model high density ratios [110]. Therefore, all these methods are in constant development and improvement. Lee & Lin [111] improved the HCZ model to handle high density ratios. Fakhari *et al.* [110] developed a method based on phase-field modeling (Jacqmin [112]) to investigate higher density ratios. Leclaire *et al.* [113] proposed a modification to the recoloring operation in the color-gradient model to reduce spurious currents and improve the stability for high density and viscosity ratios. In general, among these models, the most popular is the SC method because it is very efficient and higher density ratio can be reached, however it is less accurate than the others. HCZ and Lee-Lin models are accurate and can reach very high density ratio. However, from some recent works [114, 115], color-gradient and phase-field models were found to be the most popular for porous media applications. A detailed description of multiphase LBM is available in Huang *et al.* [116].

The applications of the LBM to fluid flow in geologic porous systems and microfluidic devices (also called micromodels) are several. First of all, it was used by many authors ([57, 58, 117–119]) to estimate permeability, effective porosity and tortuosity in synthetic porous media and real images of rocks. Ferreol & Rothman [120] simulated single-phase and two-phase flow through three-dimensional tomographic reconstructions of Fontainebleau sandstone. Xu & Liu [121] investigated relative permeability and specific interfacial length by simulating immiscible two-phase flow in 2D sample of Berea sandstone. Wang *et al.* [122] presented a general review of the LBM with a focus on boundary conditions, treatments for relaxation time in isothermal gas flow simulation in shale gas reservoirs both at the pore-scale and REV scale. Benamram *et al.* [123] applied the LBM and adapted the boundary conditions to describe the fluid flow at the REV scale in hydraulically and natural fractured reservoirs. Ahkami *et al.* [124] investigated the pore-scale behavior of single-species mineral precipitation reactions in fractured porous media using a phase field LBM. Liang *et al.* [125] proposed a model to describe three-phase flow systems and they managed to describe a density ratio up to 100 in presence of

small velocities. Zacharoudiou & Boek [126] used the free-energy LBM to investigate Haines jumps events (i.e. pore-scale events due to capillary forces occurring during a drainage process) in simplified and realistic porous media. Venturoli & Boek [127] and Laleian *et al.* [128] used the LBM with SRT to calculate the fluid flow in micromodels taking the third dimension into account by adding a viscous drag force. Boek & Venturoli [129]) used the same approach to study the fluid flow in a quasi-two-dimensional micromodel based on the image of a Berea sandstone. Wu *et al.* [130] calculated the permeability of micromodels based on Voronoi tessellation and found that it was in good agreement with experimental results. Liu *et al.* [131] simulated drainage processes in homogeneous and heterogeneous microfluidic at different capillary numbers. In Chen *et al.* [114] and Fakhari *et al.* [115], the lattice Boltzmann method with a modified color-fluid model and a phase-field model respectively were used to simulate CO_2 invasion in a water saturated micromodel; they performed 3D simulations, rather than 2D with a drag force, to avoid the approximations inherent to 2D simulations. Isfahani & Afrand [132] simulated Al_2O_3 nanofluids flow in etched glass micromodels and compared their predictions with experimental results, finding good agreement.

Besides the lattice Boltzmann method, traditional Eulerian grid-based techniques can be used to simulate single-phase and multiphase fluid flow in porous media. In CFD, the Finite Volume Method (FVM) is usually preferred because it is always locally conservative and it deals with unstructured grids [133]. In the FVM, the domain is subdivided into a finite number of contiguous control volumes whereby the integral form of the conservation laws is applied. Solution algorithms usually rely on predictor-corrector methods to solve for the pressure-velocity coupling. The Pressure-Implicit with Splitting of Operators (PISO) algorithm is one of the most popular to solve transient flow [134]. Algorithms such as Semi-Implicit Method for Pressure Linked Equations (SIMPLE) solve directly for steady state flow [135]. Details about the FVM and predictor-corrector algorithms are showed in Section 4.4.

In multiphase flow, the main difficulties are in modeling the motion of the fluid-fluid interface [94]. The isothermal and incompressible fluid motion is described by the Navier-Stokes equations, consisting of mass and momentum conservation equations. A first attempt to solve this problem for two different immiscible fluids might be writing and solve the equations for each phase, considering interface conditions to couple the fluid flow in space regions and to guarantee mass and momentum conservation across the interface. However, this approach is very difficult and computationally expensive to solve. A better alternative is to employ the whole-domain formulation [49], where the two phases are considered as one phase and the interface condition is replaced by an additional force acting only at the interface. Regardless of the approach chosen, when the governing equations are solved on a grid, the two fluids must be identified in some way and the interface location must be updated in time [49]. Methods to track the evolution of the interface are generally classified

in three categories [136]: moving mesh, surface tracking and volume tracking (or interface capturing) methods.

In moving mesh methods, the mesh might be adjusted to fit the interface or follow the fluids. In this way, a sharp interface is maintained. Surface tracking methods define a sharp interface whose motion is followed and the interface is marked and tracked. Volume tracking methods do not define the interface as a sharp boundary and the different fluids are marked by an indicator function instead. Eulerian algorithms such as level set, phase field and volume of fluid are used to capture the interface. Moving mesh and surface tracking methods have the advantage of maintaining a sharp boundary between the phases, which is independent of the representation of the flow field. This allows different resolutions of the surface and of the flow field and might improve the accuracy of the surface tension model. However, mesh or markers have to be relocated, and eventually re-meshed, when the interface undergoes large deformations increasing complexity and computational costs [136]. Moreover, they do not automatically handle changes in topology, where fluids regions merge or break up, and therefore they are not well suited for flow with interfaces undergoing complex deformations [49, 137]. Volume tracking methods are found to be the more appropriate in presence of complex interface dynamics as occurs in porous media [49].

Among volume tracking methods, the volume of fluid (VOF), first introduced by Hirt & Nichols [138], is the most popular algorithm used to describe multiphase flow in porous media and micromodels [137, 139–144]. In the VOF, the two phases are identified by a color function having values equal to 0 or 1 (arbitrarily assigned to the wetting or non-wetting phase), while the interface is represented by the region where the gradient of color function is non-zero. In order to take into account capillary forces, an interfacial tension model must be defined and it consists in an additional term in the momentum equation. The two following approaches are the most common for interfacial tension modeling: 1) Continuum Surface Force (CSF) method first introduced by Brackbill *et al.* [145] and 2) Sharp Surface Force (SSF), introduced by Renardy & Renardy [146] and improved by Raeini *et al.* [137]. In order to reduce spurious currents existing in the CSF formulation [145, 147], the volume fraction can be smoothed with a Laplacian filter, as proposed by Lafaurie *et al.* [147]. The SSF approach as proposed by Raeini *et al.* [137] reduces considerably the impact of spurious currents. In Pavuluri *et al.* [148], the authors discussed the accuracy of CSF and SSF models for spontaneous in a microchannel, comparing the results with an analytical solution. Moreover, in this paper, the initialization and boundary conditions to set in multiphase simulations are well discussed. Finally, wettability and contact angle must be taken into account in the simulations as described in Raeini *et al.* [137].

4.2 Equations of fluid motion

This Section shows the Navier-Stokes equations for single-phase incompressible fluid flow, the Navier-Stokes equations in dimensionless form, and the analytical solution of these equations in simple geometries (i.e. Poiseuille's solution).

4.2.1 Continuity equation

Consider a generic control volume Ω fixed in time and a quantity of fluid mass passing through it. The infinitesimal portion of mass m inside the control volume is $dm_\Omega = \rho\, dV$, where ρ is the fluid density, and the total mass in the control volume is $m_\Omega = \int_{V_\Omega} \rho\, dV$. The balance of all the mass entering and leaving Ω (no source term) must be equal to the mass flowing through the control volume boundary S_Ω:

$$\frac{\partial}{\partial t}\int_{V_\Omega} \rho\, dV = -\oint_{S_\Omega} \rho\mathbf{u}\cdot\hat{\mathbf{n}}\, dS, \tag{4.1}$$

where $\mathbf{u}$ is the fluid velocity, $\hat{\mathbf{n}}$ the outward unit vector normal to the surface and $\oint$ indicates that the integral is taken around a closed surface. By the use of the divergence theorem, the surface integral on the right hand side of the equation is transformed into a volume integral. Since the control volume is fixed in time and this expression is valid for an infinite number of control volumes, the integral must be zero, leading to the continuity equation in the differential form:

$$\frac{\partial \rho}{\partial t} + \nabla\cdot(\rho\mathbf{u}) = 0. \tag{4.2}$$

In all the cases discussed in this work, the fluid can be considered as incompressible. In fact, liquids such as oil and water are incompressible and gases with very low velocity (in the order of 10^{-4} m/s) can be considered incompressible as well.

For incompressible fluids, the density is a constant value ($\rho = \text{const}$), and the continuity equation reduces to

$$\nabla\cdot\mathbf{u} = 0 \tag{4.3}$$

4.2.2 Momentum equation

The same procedure can be used to derive the momentum equation. The average momentum in Ω is defined as:

$$m_\Omega\mathbf{u} = \int_{V_\Omega} \rho\mathbf{u}\, dV. \tag{4.4}$$

The total balance of momentum in the control volume is

$$\frac{\partial\,(m_\Omega\mathbf{u})}{\partial t} = \frac{\partial}{\partial t}\int_{V_\Omega}\rho\mathbf{u}\, dV + \oint_{S_\Omega}(\rho\mathbf{u}\otimes\mathbf{u})\cdot\hat{\mathbf{n}}\, dS = \oint_{S_\Omega}\mathbf{T}\cdot\hat{\mathbf{n}}\, dS + \int_{V_\Omega}\rho\mathbf{a}\, dV, \tag{4.5}$$

where $\mathbf{T}$ is the stress tensor, $\mathbf{a}$ is an acceleration vector and the symbol $\otimes$ represents the dyadic product. This equation has the same form of the Newton's second law $\mathbf{f} = m\mathbf{a}$ and

$$\oint_{S_\Omega} \mathbf{T} \cdot \hat{\mathbf{n}}\, dS + \int_{V_\Omega} \rho \mathbf{a}\, dV = \mathbf{f}_{surf} + \mathbf{f}_{body}, \tag{4.6}$$

where $\mathbf{f}_{surf}$ is the resultant of the surface forces and $\mathbf{f}_{body}$ a body force. Generally $\mathbf{a} = \mathbf{g}$, where $\mathbf{g}$ is the gravity acceleration. Now, the constitutive law for Newtonian fluids is introduced:

$$\mathbf{T} = -p\mathbf{I} + \mu\left(\nabla\mathbf{u} + (\nabla\mathbf{u})^T\right) - \frac{2}{3}\mu\nabla\left(\nabla\cdot\mathbf{u}\right), \tag{4.7}$$

where μ is the dynamic viscosity of the fluid and $\mathbf{I}$ is the identity matrix. Applying the divergence theorem, Eq. 4.5 becomes

$$\frac{\partial\left(\rho\mathbf{u}\right)}{\partial t} + \nabla\cdot\left(\rho\mathbf{u}\otimes\mathbf{u}\right) = -\nabla p + \mu\nabla^2\mathbf{u} + \frac{1}{3}\mu\nabla\left(\nabla\cdot\mathbf{u}\right) + \rho\mathbf{g}, \tag{4.8}$$

where the convective term can also be rewritten as $\nabla\cdot(\rho\mathbf{u}\otimes\mathbf{u}) = \mathbf{u}\cdot\nabla(\rho\mathbf{u}) + \rho\mathbf{u}\nabla\cdot\mathbf{u}$.

The continuity equation (Eq. 4.2) together with momentum equations (Eq. 4.8) form a system of equations called Navier-Stokes equations (NSEs).

For incompressible fluids, Eq. 4.8 can be expressed as:

$$\rho\left[\frac{\partial\mathbf{u}}{\partial t} + \mathbf{u}\nabla\cdot\mathbf{u}\right] = -\nabla p + \mu\nabla^2\mathbf{u} + \rho\mathbf{g}. \tag{4.9}$$

Adopting the total derivative $\frac{D()}{Dt} = \frac{\partial()}{\partial t} + \mathbf{u}\cdot\nabla()$, Eq. 4.9 can also be expressed as:

$$\frac{D(\rho\mathbf{u})}{Dt} = -\nabla p + \mu\nabla^2\mathbf{u} + \rho\mathbf{g}. \tag{4.10}$$

Moreover, for very small velocities the inertial term becomes negligible and Eq. 4.8 can be further simplified to obtain the so-called Stokes equation:

$$\rho\frac{\partial\mathbf{u}}{\partial t} = -\nabla p + \mu\nabla^2\mathbf{u} + \rho\mathbf{g}. \tag{4.11}$$

Finally, if the flow is steady-state the equation reduces to:

$$0 = -\nabla p + \mu\nabla^2\mathbf{u} + \rho\mathbf{g}. \tag{4.12}$$

Eq. 4.11 and Eq. 4.12 are significant in the description fluid flow in porous media.

4.2.3 Dimensionless Navier-Stokes equations

A further step is to write incompressible NSEs (Eqs. 4.3 and 4.9) in a dimensionless form. We define a characteristic length scale l_0 and time scale t_0. A characteristic fluid velocity is obtained as $U_0 = \frac{l_0}{t_0}$. Physical variables present in the Eqs. 4.3 and 4.9 are substituted by dimensionless variables

$$t^* = \frac{t}{t_c}, \quad \mathbf{u}^* = \frac{\mathbf{u}}{U_c}, \quad \frac{\partial}{\partial t^*} = \frac{l}{U_c}\frac{\partial}{\partial t} \tag{4.13}$$

and

$$p^* = p\frac{1}{\rho U_c}, \quad \nabla^* = l_c\nabla, \quad \mathbf{a}^* = \mathbf{a}\frac{l_c}{U_c^2}. \tag{4.14}$$

Substituting Eqs. 4.13 and 4.14 into Eqs. 4.3 and 4.9, we obtain the NSEs in dimensionless form as

$$\nabla^* \cdot \mathbf{u}^* = 0 \tag{4.15}$$

and

$$\frac{\partial \mathbf{u}^*}{\partial t^*} + \mathbf{u}^*\nabla^* \cdot \mathbf{u}^* = -\nabla^* p^* + \frac{1}{\mathrm{Re}}\nabla^{*2}\mathbf{u}^* + \mathbf{g}^*, \tag{4.16}$$

where

$$\mathrm{Re} = \frac{U_c\, l_c}{\nu} \tag{4.17}$$

is a dimensionless number called Reynolds number and $\nu = \mu/\rho$ is the kinematic viscosity. The advantage of expressing NSEs in a dimensionless form is that fluid flows with same Re are equivalent, even if they have different velocity, viscosity or length scale (law of similarity).

4.2.4 Poiseuille's flow

In this Section, two examples of analytical solutions of the NSEs are reported. These two cases are used in this work as a benchmark for the solutions obtained by numerical simulation.

NSEs are complex equations and they are generally solved numerically. However, analytical solutions of NSEs exist in simple geometries and making some assumptions. Two examples of typical applications are: fluid flow 1) between two parallel plates and 2) in a cylinder. In both cases, incompressible fluid, steady-state flow, negligible gravity effects, and laminar flow are assumed. Finally, no-slip boundary conditions (i.e. $u = 0$) are applied at the fluid-solid interface. The two cases are represented in Fig. 4.1.

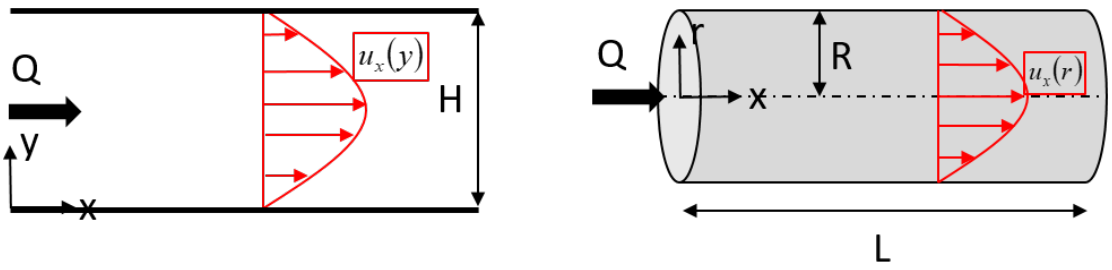

Figure 4.1: Representation of Poiseuille's flow between two parallel plates and in a cylinder.

In case 1, the Navier-Stokes system of equations reduces to

$$\begin{aligned} -\frac{\partial p}{\partial x} + \mu \frac{\partial}{\partial y}\left(\frac{\partial u_x}{\partial y}\right) = 0, \\ -\frac{\partial p}{\partial y} = 0 \end{aligned} . \tag{4.18}$$

No-slip boundary conditions are $u_x = 0$ at $y = 0$ and $u_x = 0$ at $y = H$. Solving Eq. 4.18, the velocity profile on the cross section is parabolic and equal to

$$u_x(y) = \frac{1}{2\mu} y\,(y - H)\,\frac{\Delta p}{L}, \tag{4.19}$$

where H is the distance between the plates and L is the length of the channel. From Eq. 4.19, equations for maximum velocity (u_{max}), average velocity (u_{avg}) and flow rate (Q) can be obtained as:

$$u_{\max} = -\frac{H^2}{8\mu}\frac{\Delta p}{L}, \tag{4.20}$$

$$u_{avg} = -\frac{H^2}{12\mu}\frac{\Delta p}{L} \tag{4.21}$$

and

$$Q = -\frac{H^3}{12\mu}\frac{\Delta p}{L}. \tag{4.22}$$

In case 2, radial symmetry is assumed and NSEs becomes

$$\begin{aligned} -\frac{\partial p}{\partial x} + \mu \frac{1}{r}\frac{\partial}{\partial r}\left(r\frac{\partial u_x}{\partial r}\right) = 0, \\ -\frac{\partial p}{\partial r} = 0 \end{aligned} . \tag{4.23}$$

In this case the no-slip boundary condition is $u_x = 0$ at $r = 0$ and the solution is

$$u_x(r) = \frac{(r^2 - R^2)}{4\mu}\frac{\Delta p}{L}. \tag{4.24}$$

From here, the maximum velocity (at $r = 0$), average velocity and flow rate are respectively

$$u_{\max} = -\frac{R^4}{4\mu}\frac{\Delta p}{L}, \tag{4.25}$$

$$u_{avg} = -\frac{R^2}{8\mu}\frac{\Delta p}{L} \tag{4.26}$$

and

$$Q = -\frac{\pi R^4}{8\mu}\frac{\Delta p}{L}. \tag{4.27}$$

4.3 The Lattice Boltzmann Method: theory and implementation

The Lattice Boltzmann Method (LBM) is a relatively new CFD method, first introduced in the late 1980s by McNamara & Zanetti [149], successively developed by several authors [105–107, 109, 150–152] and still subject of research activity [98, 110, 124]. Historically, the lattice Boltzmann method has its origin in cellular automata (CA), which were developed considering that different microscopic interactions can lead to the same form of macroscopic equations. In general, CA consist of a discretization of space in which individual nodes may be empty ($m = 0$) or occupied by one particle having unit mass ($m = 1$). A velocity can be assigned to each particle by the vector connecting the node to its next neighbor node along the link where the particle is located. The microscopic interaction is strictly local and at each time step, each particle moves forward to the next node in the direction of the velocity vector. When two or more particles meet at the same node, collision occurs: particles exchange momentum and each node updates its state. Conservation of mass and momentum is kept summing up mass over the each node and verifying that the number of particles and the total velocity of the particles is the same before and after the collision. The repetition of collision and propagation constitutes the microdynamics. Macroscopic properties are calculated averaging mass and momentum over a large number of nodes.

The first authors to study CA were Ulam [153], Neumann & Burks [154] and Zuse [155]. Later, Hardy *et al.* [156] proposed a model (called HPP from the names of the authors), where the grid was square and the particles had only four possible velocities. In this model, each collision had only one possible result. However, the main disadvantage of the HPP model is that it was not able to the recover the

macroscopic NSEs solutions and for this reason it was not usable in fluid dynamics. Later, Frisch *et al.* [157] discovered that CA over a lattice with hexagon symmetry were able to recover the NSEs in the macroscopic limit. This was the first example of lattice gas cellular automata (LGCA) and their model is called FHP. However, their model suffered of statistical noise, which is a general problem when trying to recover macroscopic quantities from a microscopic model. A few years later, McNamara & Zanetti [149] fixed the noise problem in LGCA replacing the individual particles with an averaged directional discrete distribution function. This was the first example of the LBM. A major simplification was introduced by Qian *et al.* [150], who introduced the single relaxation time model based on the BGK collision model proposed by Bhatnagar *et al.* [101].

In this Section, the kinetic theory, which is at the base of the Lattice Boltzmann Method, is briefly discussed, then the numerical method and its implementation are explained and finally three examples are reported.

4.3.1 Elements of gas kinetic theory

The kinetic theory is a description of fluids at the mesoscopic scale, which lies between the microscopic scale where the motion of individual molecules is tracked and the macroscopic scale based on continuum theory [98]. The kinetic theory is based on the evolution of particle distributions in a gas on time scales around the mean collision time. Most of the physical quantities such as fluid velocity, pressure and temperature originate from a statistical average over a large number of particles. The cornerstone of the kinetic theory is the Boltzmann equation [105].

The fundamental variable in kinetic theory is the particle distribution function $f(\mathbf{x}, \mathbf{c}, t)$. The particle distribution function represents the density of particles with velocity $\mathbf{c}$ (called microscopic velocity) at position $\mathbf{x}$ and time t [98]. $f(\mathbf{x}, \mathbf{c}, t)$ is a probability density function and $f(\mathbf{x}, \mathbf{c}, t)\,\mathrm{d}\mathbf{x}\mathrm{d}\mathbf{c}$ is the probability to find a particle at time t positioned between $\mathbf{x}$ and $\mathbf{x} + \mathrm{d}\mathbf{x}$ with a microscopic velocity between $\mathbf{c}$ and $\mathbf{c} + \mathrm{d}\mathbf{c}$ [158].

The Boltzmann equation describes the evolution in time of $f(\mathbf{x}, \mathbf{c}, t)$ in terms of collisions which redistribute the distribution function at the considered time [98]. Collisions are elementary binary interactions between couples of particle distributions and are treated as they occur instantly [105, 158]. The Boltzmann equation is expressed as:

$$\frac{\partial f}{\partial t} + \mathbf{c} \cdot \nabla f + \mathbf{F} \cdot \nabla_{\mathbf{c}} f = \Omega(f, f), \tag{4.28}$$

where $\mathbf{F}$ is the external force contribution and $\Omega(f, f)$ is called collision operator.

Macroscopic hydrodynamic quantities can be calculated from moments of f. These moments are integrals of f, weighted with $\mathbf{c}$ over the entire velocity space

[98]. Macroscopic fluid density, momentum and energy are calculated as:

$$\rho\left(\mathbf{x},t\right)=\int f\left(\mathbf{x},\mathbf{c},t\right)\mathrm{d}\mathbf{c}, \tag{4.29}$$

$$\rho\left(\mathbf{x},t\right)\mathbf{u}\left(\mathbf{x},t\right)=\int \mathbf{c}f\left(\mathbf{x},\mathbf{c},t\right)\mathrm{d}\mathbf{c} \tag{4.30}$$

and

$$\rho\left(\mathbf{x},t\right)E\left(\mathbf{x},t\right)=\frac{1}{2}\int\left|\mathbf{c}\right|^{2}f\left(\mathbf{x},\mathbf{c},t\right)\mathrm{d}\mathbf{c} \tag{4.31}$$

where $\mathbf{u}$ is the average velocity of the particles, which corresponds to the macroscopic fluid velocity. By integrating over the velocity space in this way, particles of all possible velocities at position $\mathbf{x}$ and time t are contributing to the calculation of macroscopic density, momentum and energy. The random thermal velocity $\boldsymbol{\xi}$ is defined as the velocity of the particles with respect the fluid $\boldsymbol{\xi}=\mathbf{c}-\mathbf{u}$ and the magnitude value $|\boldsymbol{\xi}|$ is called peculiar speed [105]. The energy associated to $\boldsymbol{\xi}$ is called internal energy e, which is defined as

$$\rho\left(\mathbf{x},t\right)e\left(\mathbf{x},t\right)=\frac{1}{2}\int\left|\boldsymbol{\xi}\right|^{2}f\left(\mathbf{x},\mathbf{c},t\right)\mathrm{d}\mathbf{c}. \tag{4.32}$$

The internal energy is only related to translational kinetic energy because in kinetic theory we deal only with monoatomic perfect gases with no rotational or vibrational degrees of freedom [98].

An expression of the macroscopic fluid pressure can be found through the ideal gas law [98]:

$$p\left(\mathbf{x},t\right)=\rho\left(\mathbf{x},t\right)RT, \tag{4.33}$$

where R is the gas constant and T the temperature. The ideal equation of state can be also expressed based on the speed of sound c_s. The speed of sound in a fluid is the velocity at which a weak pressure wave propagates isoentropically (i.e. the entropy S is constant) in the medium and it is defined as [159]

$$c_s=\left(\frac{\partial p}{\partial\rho}\right)_S. \tag{4.34}$$

In isothermal conditions c_s is a constant and Eq. 4.33 can be written as

$$p\left(\mathbf{x},t\right)=c_s^2\rho\left(\mathbf{x},t\right), \tag{4.35}$$

where $c_s=\sqrt{RT}$. Eq. 4.35 is widely used in the isothermal LBM.

Any solution of the Boltzmann equation requires an expression of the collision operator. Under the condition of binary collisions, the collision term can be split into gain and loss components, corresponding to direct/inverse collisions taking molecules in/out a volume element [105].

In order to simplify the expression of the collision operator, the concept of equilibrium distribution function f^{eq} must be introduced. f^{eq} is a particular particle distribution such that $\Omega\left(f^{eq}, f^{eq}\right) = 0$. This condition is called local equilibrium. In other words, a distribution function f^{eq} is defined such that gain and losses are in exact balance so that the collision term is annihilated [105]. In D spatial dimensions it is expressed as [152]:

$$f^{eq} = \frac{\rho}{(2\pi RT)^{D/2}} \exp\left[-\frac{(\mathbf{c}-\mathbf{u})^2}{2RT}\right], \tag{4.36}$$

where R is the ideal gas constant and T is the temperature. The distribution function reported in Eq. 4.36 is also called Maxwellian distribution function and it represented in Fig. 4.2.

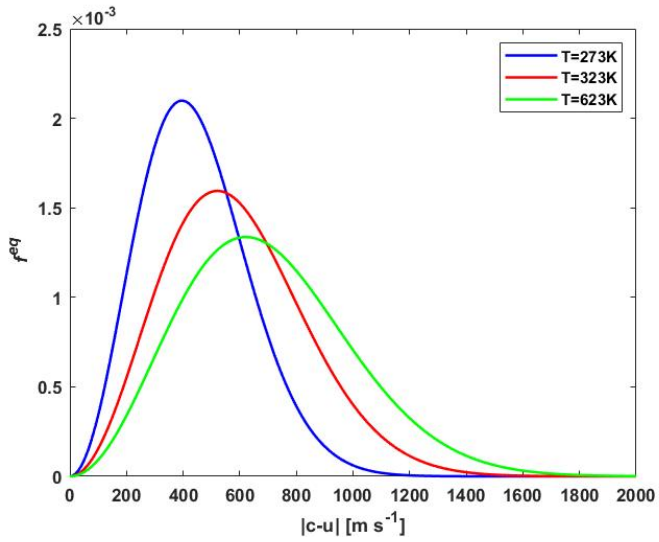

Figure 4.2: Maxwellian distribution function for air as a function of the peculiar speed $|\mathbf{c}-\mathbf{u}|$. Here, $D = 3$ in Eq. 4.36 because a three dimensional space is considered. Increasing the temperature, the peculiar velocity increases because the particles are at a higher state of internal energy.

Originally, the collision operator was expressed as a complicated nonlinear integral over the velocity space. However, in order to facilitate numerical solutions of the Boltzmann equation through the LBM, the collision operator can be expressed in a simpler way without loosing the basic physics [105]. This collision operator is called BGK (Bhatnagar-Gross-Krook) and it is expressed as [101]

$$C_{BGK}(f) = -\frac{f - f^{eq}}{\tau}, \tag{4.37}$$

where τ in this context is called relaxation time. τ is a typical time-scale associated with collisional relaxation to the local equilibrium. Physically, Eq. 4.37 can be seen

as the tendency of f to approach its equilibrium state f^{eq} after a time τ. In principle, the relaxation time τ is a complicated functional of the distribution function f. The drastic simplification associated with BGK is the assumption of a constant value for this relaxation scale, which is equivalent to lumping the whole spectrum of relaxation scales into a single value [105]. Introducing the BGK collision operator into the Boltzmann equation, Eq. 4.28 becomes

$$\frac{\partial f}{\partial t} + \mathbf{c} \cdot \nabla f + \mathbf{F} \cdot \nabla_{\mathbf{c}} f = -\frac{f - f^{eq}}{\tau}. \tag{4.38}$$

Eq. 4.38 is the starting point to derive the lattice Boltzmann equation in Section 4.3.2.

Collisions conserve the quantities of mass and momentum and they can be expressed by the statistical moments of the collision operator as

$$\int \Omega\left(f, f\right) \mathrm{d}\mathbf{c} = 0, \tag{4.39}$$

and

$$\int \mathbf{c}\ \Omega\left(f, f\right) \mathrm{d}\mathbf{c} = \mathbf{0}. \tag{4.40}$$

Phenomena of viscous dissipation are connected to the non-equilibrium, i.e. the deviation of f from f^{eq}. The non-equilibrium distribution function f^{neq} is calculated as

$$f^{neq} = f - f^{eq}. \tag{4.41}$$

The Chapman-Enskog analysis [160] is the method used to connect the mesoscopic and macroscopic scales through f^{neq}.

4.3.2 The Lattice Boltzmann Equation

As shown Section 4.3.1, solutions of the Boltzmann equation (Eq. 4.28) are able to recover macroscopic hydrodynamic properties. The idea behind the lattice Boltzmann method is to solve the equation numerically and recover macroscopic fluid flow information [98]. In fact, the numerical scheme to solve the Boltzmann equation turns out to be simpler to implement than traditional methods used to solve numerically the Navier-Stokes equations.

In single-phase fluid flow in porous media at the pore-scale, the force term appearing in Eq. 4.38 is not present. Then, Eq. 4.38 simplifies to

$$\frac{\partial f}{\partial t} + \mathbf{c} \cdot \nabla f = -\frac{f - f^{eq}}{\tau}. \tag{4.42}$$

Using the definition of total derivative (Section 4.2.2), Eq. 4.42 can be rewritten as

$$\frac{Df}{Dt} = -\frac{1}{\tau}\left(f - f^{eq}\right), \tag{4.43}$$

where

$$\frac{Df}{Dt} = \frac{f\left(\mathbf{x}+\mathbf{c}\Delta t, \mathbf{c}, t+\Delta t\right) - f\left(\mathbf{x}, \mathbf{c}, t\right)}{\Delta t} + O\left(\Delta t^2\right). \tag{4.44}$$

Neglecting terms of order higher than Δt, Eq. 4.43 is rewritten using Eq. 4.44 and becomes

$$\frac{f\left(\mathbf{x}+\mathbf{c}\Delta t, \mathbf{c}, t+\Delta t\right) - f\left(\mathbf{x}, \mathbf{c}, t\right)}{\Delta t} = -\frac{1}{\tau}\left(f - f^{eq}\right), \tag{4.45}$$

or, rearranging,

$$f\left(\mathbf{x}+\mathbf{c}\Delta t, \mathbf{c}, t+\Delta t\right) - f\left(\mathbf{x}, \mathbf{c}, t\right) = -\frac{\Delta t}{\tau}\left(f - f^{eq}\right). \tag{4.46}$$

In order to evaluate numerically the hydrodynamic moments reported in Eq. 4.29 and 4.30, the microscopic velocity $\mathbf{c}$ must be discretized. A set of discrete microscopic velocities $\mathbf{c}_i$ are defined and the distribution function will be evaluated only for the selected velocities. This set of microscopic velocities is called lattice.

Space and time are discretized on the lattice obtaining the lattice Boltzmann equation (LBE):

$$f_i\left(\mathbf{x}+\mathbf{c}_i\Delta t, t+\Delta t\right) - f_i\left(\mathbf{x}, t\right) = -\frac{\Delta t}{\tau}\left[f_i\left(\mathbf{x}, t\right) - f_i^{eq}\left(\mathbf{x}, t\right)\right], \tag{4.47}$$

where $f_i\left(\mathbf{x}, t\right)$ is the density distribution function related to the discrete velocity direction i. $f_i\left(\mathbf{x}, t\right)$ is called discrete velocity distribution function or population. This equation expresses that the discrete particle distribution $f_i\left(\mathbf{x}, t\right)$ moves with velocity $\mathbf{c}_i$ to a neighbor point $\mathbf{x}+\mathbf{c}_i\Delta t$ at the next time step $t+\Delta t$. At time t, the particles are affected by collision, modeled using the BGK collision operator. This operator models particle collisions by redistributing particles among the populations f_i at each site and it relaxes the populations towards an equilibrium f_i^{eq} at a rate determined by the relaxation time τ. Since the BGK collision operator is used, sometimes Eq. 4.47 is also called LBGK (lattice BGK) equation. The lattice Boltzmann method refers to the numerical procedure used to solve Eq. 4.47.

The BGK is not the only possible collision operator. For example, two-relaxation-times (TRT) and multi-relaxation-times (MRT) collision operators exist and they use more than one relaxation time [98, 158]. TRT and MRT collision operators can reduce some limitations of the BGK model, such as problems related to the application of some boundary conditions or accuracy or stability problems [98], however they will not be discussed in this work.

Usually in the LBM, physical space, time and velocity are replaced with non-dimensional quantities called lattice units such that $|\mathbf{c}_i| = \frac{\Delta x}{\Delta t} = 1$ and $\Delta t = 1$, where $|\mathbf{c}_i|$ is called lattice speed. More details about the non-dimensionalization process and lattice units are given in the Section 4.3.3. In lattice units, Eq. 4.47 can be rewritten as

$$f_i\left(\mathbf{x}+\mathbf{c}_i, t+1\right) = \left(1-\frac{1}{\tau}\right) f_i\left(\mathbf{x}, t\right) + \frac{1}{\tau} f_i^{eq}\left(\mathbf{x}, t\right). \tag{4.48}$$

For small Mach numbers ($\mathrm{Ma} = u/c_s$), the exponential function in Eq. 4.36 can be approximated with a polynomial function ($e^x \approx 1 + x + \frac{x^2}{2}$), and the discrete equilibrium distribution function f_i^{eq} becomes [150, 152]

$$f_i^{eq} = w_i \rho \left[1 + \frac{\mathbf{c}_i \cdot \mathbf{u}}{c_s^2} + \frac{(\mathbf{c}_i \cdot \mathbf{u})^2}{2c_s^4} - \frac{\mathbf{u}^2}{2c_s^2} \right], \tag{4.49}$$

where and w_i are weights depending on the lattice velocity direction, ρ is the macroscopic density, $\mathbf{u}$ the macroscopic velocity vector and c_s the sound speed.

Velocity sets are usually named by the number of spatial dimensions (d) and the number of discrete velocities (q), using the notation DdQq. The two most common lattice velocity sets are D2Q9 in two-dimensional cases and D3Q19 in three-dimensional problems; they are illustrated in Fig. 4.3. Most velocity sets have one rest velocity with zero magnitude that represents stationary populations (i.e. these populations do not propagate to neighbor lattice sites) and it is often assigned the index $i = 0$ (i.e. $\mathbf{c}_0 = 0$). In this work, this convention counting from 0 to $q - 1$ was adopted. For example, D2Q9 means 9 discrete velocities in 2D and velocities are numbered from 0 to 8.

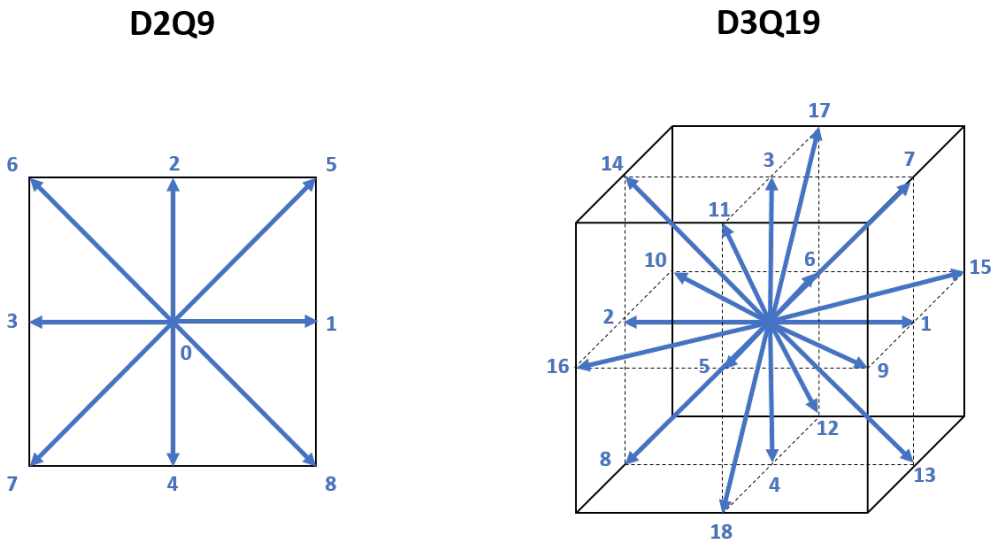

Figure 4.3: Discrete velocity models D2Q9 and D3Q19

As briefly mentioned at the beginning of this Chapter, a lattice cell has to have sufficient symmetry to be able to recover macroscopic density and momentum [157]. For this reason, constraints on the velocity sets must be fulfilled [98]:

$$\sum_i w_i = 1, \tag{4.50}$$

$$\sum_i w_i c_{i\alpha} = 0, \tag{4.51}$$

$$\sum_i w_i c_{i\alpha} c_{i\beta} = c_s^2 \delta_{\alpha\beta}, \tag{4.52}$$

$$\sum_i w_i c_{i\alpha} c_{i\beta} e_{i\gamma} = 0, \tag{4.53}$$

$$\sum_i w_i c_{i\alpha} c_{i\beta} c_{i\gamma} c_{i\delta} = c_s^4 \left(\delta_{\alpha\beta}\delta_{\gamma\delta} + \delta_{\alpha\gamma}\delta_{\beta\delta} + \delta_{\alpha\delta}\delta_{\beta\gamma}\right), \tag{4.54}$$

$$\sum_i w_i c_{i\alpha} e_{i\beta} c_{i\gamma} c_{i\delta} c_{i\epsilon} = 0, \tag{4.55}$$

where $c_{i\alpha}, c_{i\beta}, c_{i\gamma}, e_{i\delta}, c_{i\epsilon}$ are lattice velocity vectors written using the Einstein notation and $\delta_{\alpha\beta}, \delta_{\gamma\delta}, \delta_{\alpha\gamma}, \delta_{\beta\delta}, \delta_{\alpha\delta}, \delta_{\beta\gamma}$ are the Kronecker deltas. For example, $\delta_{\alpha\beta} = 1$ if $\alpha = \beta$ and $\delta_{\alpha\beta} = 0$ otherwise.

Since there is symmetry, in D2Q9 we can set $w_1 = w_2 = w_3 = w_4 = w_m$ and $w_5 = w_6 = w_7 = w_8 = w_s$. For isothermal LBM, using the D2Q9, the speed of sound is expressed in lattice units as $c_s = 1/\sqrt{3}$ [98] and using Eqs. 4.50, 4.51 and 4.54, the following equations can be written:

$$\sum_i w_i = w_0 + 4w_m + 4w_s = 1, \tag{4.56}$$

$$\sum_i w_i c_{ix} c_{ix} = 2w_m + 4w_s = \frac{1}{3}, \tag{4.57}$$

$$\sum_i w_i c_{ix} c_{ix} c_{iy} c_{iy} = 4w_s = \frac{1}{9}. \tag{4.58}$$

Then, the following system of equations has to be solved in order to obtain the weights w_i comparing in Eq. 4.49:

$$\begin{cases} w_0 + 4w_m + 4w_s = 1 \\ 2w_m + 4w_s = \frac{1}{3} \\ 4w_s = \frac{1}{9} \end{cases}. \tag{4.59}$$

From the system of equations 4.59, the weights are

$$w_i = \begin{cases} 4/9 & i = 0 \\ 1/9 & i = 1,2,3,4 \\ 1/36 & i = 5,6,7,8 \end{cases}. \tag{4.60}$$

In Tables 4.1 and 4.2 are summarized the properties of D2Q9 and D3Q19 velocity sets respectively.

Table 4.1: Weights (w_i) and lattice velocities (c_i) for the D2Q9 model

i	0	1	2	3	4	5	6	7	8
w_i	$\frac{4}{9}$	$\frac{1}{9}$	$\frac{1}{9}$	$\frac{1}{9}$	$\frac{1}{9}$	$\frac{1}{36}$	$\frac{1}{36}$	$\frac{1}{36}$	$\frac{1}{36}$
$c_{i,x}$	0	1	0	-1	0	1	-1	-1	1
$c_{i,y}$	0	0	1	0	-1	1	1	-1	-1

Table 4.2: Weights (w_i) and lattice velocities (c_i) for the D3Q19 model

i	0	1	2	3	4	5	6	7	8	9	10	11	12	13	14	15	16	17	18
w_i	$\frac{1}{3}$	$\frac{1}{18}$	$\frac{1}{18}$	$\frac{1}{18}$	$\frac{1}{18}$	$\frac{1}{18}$	$\frac{1}{18}$	$\frac{1}{18}$	$\frac{1}{36}$	$\frac{1}{36}$	$\frac{1}{36}$	$\frac{1}{36}$	$\frac{1}{36}$	$\frac{1}{36}$	$\frac{1}{36}$	$\frac{1}{36}$	$\frac{1}{36}$	$\frac{1}{36}$	$\frac{1}{36}$
$c_{i,x}$	0	1	-1	0	0	0	0	1	-1	1	-1	0	0	1	-1	1	-1	0	0
$c_{i,y}$	0	0	0	1	-1	0	0	1	-1	0	0	1	-1	-1	1	0	0	1	-1
$c_{i,z}$	0	0	0	0	0	1	-1	0	0	1	-1	1	-1	0	0	-1	1	-1	1

After the LBE is solved and f_i^{eq} are calculated, macroscopic fluid density ρ and momentum $\rho\mathbf{u}$ can be calculated respectively as

$$\rho\left(\mathbf{x},t\right)=\sum_i f_i \tag{4.61}$$

and

$$\rho\left(\mathbf{x},t\right)\mathbf{u}\left(\mathbf{x},t\right)=\sum_i f_i\mathbf{c}_i. \tag{4.62}$$

Fluid pressure can be computed from Eq. 4.61 through an equation of state. In isothermal conditions, the fluid pressure can be computed from Eq. 4.61 through the speed of sound as

$$p=c_s^2\rho. \tag{4.63}$$

In the LBM, Eq. 4.47 is decomposed into two distinct parts and is solved in two consecutive steps: 1) collision (or relaxation) and 2) streaming (or propagation). This two steps are represented in Fig. 4.4. The two operations can be respectively expressed mathematically as

$$f_i^{post}(\mathbf{x},t)=f_i(\mathbf{x},t)-\frac{1}{\tau}\left(f_i(\mathbf{x},t)-f_i^{eq}(\mathbf{x},t)\right) \tag{4.64}$$

and

$$f_i(\mathbf{x}+\mathbf{c}_i,t+1)=f_i^{post}(\mathbf{x},t), \tag{4.65}$$

where f_i^{post} is the distribution function after collision.

The collision is a local operation and post-collision populations f_i^{post} are evaluated applying Eq. 4.64. Then, the results are streamed to the neighbor locations as in Eq. 4.65. When these two operations are complete, one time step has elapsed and the procedure moves to the next time.

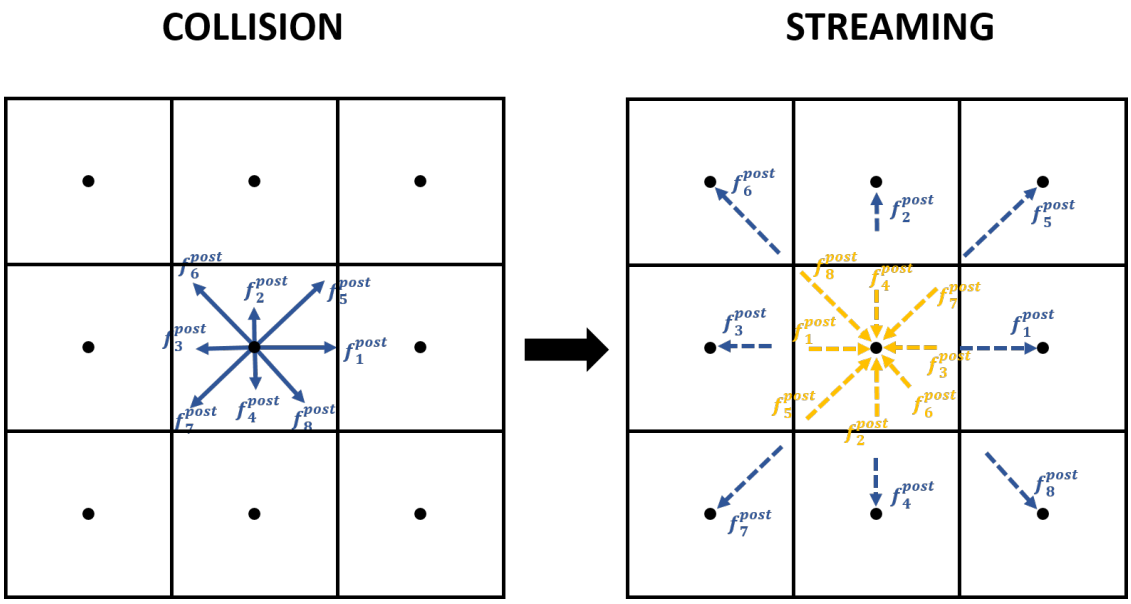

Figure 4.4: Representation of collision and streaming steps. On this grid, the attention is focused on the central node. After collision, populations are in a state called post-collision (f_i^{post}), represented as solid arrows on the left picture. Each population has a different value and this is represented by the length of the arrow. After collision, the streaming step occurs and f_i^{post} propagate to their neighbor nodes where they collide with the populations incoming from the other nodes. The streamed populations are represented as dashed arrows. On the right picture, populations incoming from the neighbor nodes to the considered node are represented in orange.

4.3.3 Lattice units

Lattice Boltzmann simulations are usually performed using dimensionless units, that are related to physical units through units conversions or dimensionless numbers [98]. In the LBM, dimensionless units are called lattice units (l.u.).

In general, non-dimensionalization is achieved by dividing a physical quantity by a reference quantity, which must be properly chosen and have the same dimensions of the physical quantity. The reference quantity is also called conversion factor. In the following, we refer to physical quantities using the subscript p and to quantities in lattice units withe the subscript lb. Even if basic conversion factors are arbitrary, it is important that all the physical quantities involved in the problem are non-dimensionalized in a consistent way. In the conversion from physical units to lattice units, an important role is played by the Reynolds number, which is identical in

both units systems, i.e.

$$\mathrm{Re} = \frac{U_p\, l_p}{\nu_p} = \frac{U_{lb}\, l_{lb}}{\nu_{lb}}. \tag{4.66}$$

This is related to the law of similarity (paragraph 4.2.3), which states that two incompressible flow systems are similar if they have the same Reynolds number and geometry [98]. In the following part of the paragraph, conversions used in our simulations are showed and an example based on the fluid flow between two parallel plates is given.

In order to set the simulation parameters, space, time and density in physical units are related each other through the cell and time steps:

$$\mathbf{x}_p = \mathbf{x}_{lb}\, \Delta x, \tag{4.67}$$

$$t_p = t_{lb}\, \Delta t, \tag{4.68}$$

and

$$\rho_p = \rho_{lb}\, \Delta \rho, \tag{4.69}$$

where Δx, Δt and $\Delta \rho$ are the conversion factors and their units are respectively m, s and kg/m^3. As already mentioned in the previous paragraph, it is common in the LBM to set the cell size and the time step in lattice units are equal to unity, i.e. $\Delta x_{lb} = 1$ and $\Delta t_{lb} = 1$. The non-dimensionalization process starts obtaining Δx. A physical system having a characteristic space length l_p discretized by N cells is considered; in this case, the cell size is

$$\Delta x = \frac{l_p}{N}. \tag{4.70}$$

For density, the calculation is straightforward as well because in the LBM $\rho_{lb} = 1$ and therefore $\Delta \rho = \rho_p$. For calculating Δt there are two ways, depending on the problem and the data available, using either the velocity or the kinematic viscosity. The velocity (m/s) can be converted to lattice units by

$$u_p = u_{lb} \frac{\Delta x}{\Delta t}, \tag{4.71}$$

and the kinematic viscosity (m^2/s) by

$$\nu_p = \nu_{lb} \frac{\Delta x^2}{\Delta t}. \tag{4.72}$$

Since in our application it is not easy to know the characteristic fluid velocity *a priori*, the kinematic viscosity is used for the conversion and therefore

$$\Delta t = \frac{\nu_{lb}}{\nu_p} \Delta x^2. \tag{4.73}$$

Now the problem is reduced to the calculation of ν_{lb}, which is related to the relaxation time (τ) through

$$\nu_{lb} = c_s^2(\tau - 0.5)\Delta t_{lb}, \tag{4.74}$$

where $c_s^2 = 1/3$ and τ must be imposed. In this way, the kinematic viscosity and the relaxation time must be given as inputs to the simulation. From Eq. 4.74 originates the condition $\tau > \frac{1}{2}$ to have positive viscosity.

It should be recalled from paragraph 4.3.2 that the equilibrium distribution function can be approximated to Eq. 4.49 for small Mach numbers (i.e. if $u_{lb} << c_s$) and typically it is set $u_{lb} < 0.1$. For this reason, in order to avoid the simulation diverging, this requirement must be satisfied and u_{lb} is calculated through the Reynolds number:

$$u_{lb} = \frac{\mathrm{Re}\,\nu_{lb}}{l_{lb}}. \tag{4.75}$$

Note that in this way the Reynolds number must be calculated using physical units or imposed, as it usually happens.

Finally, the pressure must be converted to lattice units. To facilitate the calculations, the kinematic pressure (i.e. pressure/density), which has units $\mathrm{m}^2/\mathrm{s}^2$, is used:

$$p_{lb} = \frac{p_p}{\left(\frac{\Delta x}{\Delta t}\right)^2}. \tag{4.76}$$

Also, pressure and density are related though the sound speed:

$$p_{lb} = c_s^2\,\rho_{lb}. \tag{4.77}$$

When the simulation ends, the same expressions inverted can be used to convert the resulting quantities from lattice units to physical units. In the next paragraph, an example is proposed to facilitate the understanding of lattice units and how the conversion was performed in this work.

Example of lattice units conversion

Consider a 2D microchannel having length $L = 6 \times 10^{-4}$ m and height $H = 1.5 \times 10^{-4}$ m. The characteristic length of the system is $l = H/2 = 7.5 \times 10^{-5}$ m. The fluid has a density $\rho = 1050$ kg/m^3 and viscosity $\mu = 1 \times 10^{-3}$ Pa s, therefore the kinematic viscosity is $\nu = 9.52 \times 10^{-7}$ m^2/s. The pressure gradient across the channel is $\Delta p/L = 80$ Pa/m, which results in a pressure difference between inlet and outlet of $\Delta p = 4.8 \times 10^{-2}$ Pa and a kinematic pressure of $\Delta p_{kin} = 4.57 \times 10^{-5}$ m^2/s^2. In this case the maximum velocity is known analytically from Eq. 4.20 and it is $u_{max} = 2.25 \times 10^{-3}$ m/s. Using the maximum velocity as characteristic velocity, the Reynolds number can be calculated and $\mathrm{Re} = 1.77 \times 10^{-2}$. In porous media application, $\mathrm{Re} \leq 2$ is a condition to satisfy in order to apply the Darcy's law. For

the space discretization, 240 cells are placed in the x direction (i.e. $N_x = 240$) and 60 cells in the y direction (i.e. $N_y = 60$). The relaxation time is $\tau = 0.75$.

The non-dimensionalization starts applying Eq. 4.70, obtaining $\Delta x = 2.5 \times 10^{-6}$ m and the characteristic length $l_{lb} = 30$ l.u. The kinematic viscosity is calculated from Eq. 4.74 and it is equal to $\nu_{lb} = 0.083$ l.u. The time step is calculated using Eq. 4.73 and it is equal to $\Delta t = 5.47 \times 10^{-7}$ s. The maximum velocity calculated by Eq. 4.75 is $u_{lb} = 4.92 \times 10^{-5} < 0.1$ l.u. (the condition for the incompressibility limit is satisfied). Finally, the pressure difference is converted to $\Delta p_{lb} = 2.19 \times 10^{-6}$ l.u., using Eq. 4.76.

4.3.4 Boundary conditions

Boundary conditions in the LBM are more complicated than in traditional CFD methods where usually velocity or pressure values are fixed in order to close the system. In fact, in the LBM there are higher degrees of freedom related to the populations f_i that must be determined. At boundaries such as fluid-solid boundaries or inlets and outlets, after the streaming step populations belonging to fluid nodes propagate to neighbor nodes. On the contrary, this behavior is not possible for populations on boundary sites pointing to the inner domain. These incoming populations are not specified by the LBE and they must be evaluated in a different way [161]. The role of LB boundary conditions is to prescribe adequate values for the incoming populations, i.e. those propagating from the solid object into fluid region [98, 161].

The next two paragraphs discuss the bounce-back method [98] to treat fluid-solid boundaries and the Zou-He method [162] for inlet and outlet flow boundaries. These two boundary conditions are used to model fluid-solid grains interactions and pressure difference between inlet and outlet as in laboratory flow experiments. At the end of the paragraph, periodic boundary conditions, which are useful in simple cases and numerical tests, are briefly discussed.

Bounce-back boundary condition at solid boundaries

In pore-scale fluid flow simulation, the most common fluid-solid boundary condition is the no-slip velocity boundary condition. The most popular way to include this boundary condition in the LB framework is through the bounce-back method, due to its simplicity of implementation. Basically, populations hitting a rigid wall during the streaming step are reflected back to where they came from.

The bounce-back method can be realized in two different ways: fullway bounce-back and halfway bounce-back. In fullway bounce-back, populations travel the complete link path to the solid node and then they are inverted during the collision step in the next time step. In halfway bounce-back, populations travel only half of the link distance and the inversion occurs during the streaming step in the current

time step. In this work, the halfway bounce-back is implemented because it is more accurate [98]. Quantitatively, in the halfway bounce-back method, populations leaving the boundary node $\mathbf{x}_b$ at time t meet the solid surface at time $t+\frac{\Delta t}{2}$ where they are reflected back with a velocity $\mathbf{c}_{\bar{i}} = -\mathbf{c}_i$, going back to the node $\mathbf{x}_b$ at time $t+\Delta t$ at the node $\mathbf{x}_b$. For these populations, the standard streaming step is replaced by

$$f_{\bar{i}}\left(\mathbf{x}_b, t+\Delta t\right) = f_i^{post}\left(\mathbf{x}_b, t\right). \tag{4.78}$$

The bounce-back boundary condition can be applied in the same way to 2D and 3D cases. In order to explain in a clearer way this boundary condition, an example is proposed. Consider the case of a resting wall in 2D with the D2Q9 velocity scheme, as illustrated in Fig. 4.5. Populations f_2, f_5 and f_6 (in red) are unknown after the streaming step because they should come from the solid, while the remaining populations (in green) are known because they income from a neighbor lattice node. Unknown populations can be calculated via half bounce-back as:

$$f_2\left(\mathbf{x}_b, t+\Delta t\right) = f_4^{post}\left(\mathbf{x}_b, t\right), \tag{4.79}$$

$$f_5\left(\mathbf{x}_b, t+\Delta t\right) = f_7^{post}\left(\mathbf{x}_b, t\right), \tag{4.80}$$

$$f_6\left(\mathbf{x}_b, t+\Delta t\right) = f_8^{post}\left(\mathbf{x}_b, t\right), \tag{4.81}$$

Zou-He boundary condition at open boundaries

Zou & He [162] proposed a method to specify density (pressure) or velocity on flow boundaries such as inlet and outlet, based on the idea of bounce-back of the non-equilibrium distribution function. For this reason, the Zou-He method is also called non-equilibrium bounce-back (NEBB) method.

Let us consider a Poiseuille's flow in a 2D channel. The situation at the inlet is depicted in Fig. 4.6. After streaming, f_0, f_2, f_3, f_4, f_6, f_7 (in green) are known. The objective is to determine f_1, f_5, f_8 populations (in red), supposing that $u_{x,in}$ or ρ_{in} are specified at the inlet boundary, through Eqs. 4.61 and 4.62 in a reverse way (i.e. density and velocity are known and the populations has to be recovered).

As a first case, we consider that a constant density ρ_{in} is imposed at the inlet. Populations f_1, f_5 and f_8 and $u_{x,in}$ has to be calculated. Using Eqs. 4.61 and 4.62, the equations are:

$$\rho_{in} = f_0 + f_1 + f_2 + f_3 + f_4 + f_5 + f_6 + f_7 + f_8, \tag{4.82}$$

$$\rho_{in} u_{x,in} = f_1 - f_3 + f_5 - f_6 - f_7 + f_8 \tag{4.83}$$

and, considering that the y-direction velocity component is zero,

$$\rho_{in} u_{y,in} = 0 = f_2 - f_4 + f_5 + f_6 - f_7 - f_8. \tag{4.84}$$

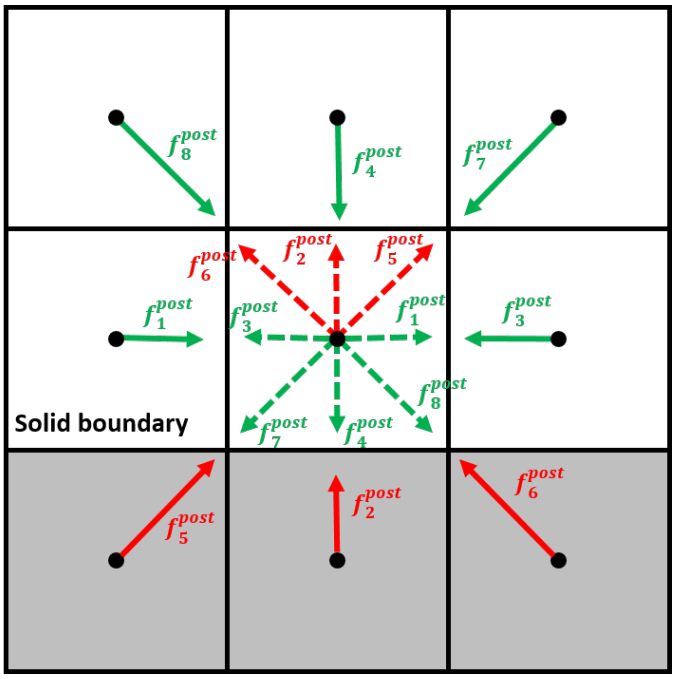

Figure 4.5: Bounce-back boundary condition on fluid-solid boundaries. The solid arrows represent the post-collision populations, while the dashed ones are the populations after streaming. After streaming, f_1, f_3, f_4, f_7, f_8 (in green) income from the neighbor fluid nodes, while f_2, f_5, f_8 (in red) are unknown because they should propagate from outside the computational domain. The unknown populations are computed by Eq. 4.78.

Since one equation is missing to close the system, it is assumed that the bounce-back rule is still correct for the non-equilibrium part of the populations normal to the boundary [162]. For example, the non-equilibrium bounce-back method is applied to population f_1. In order to compute the non equilibrium function f_1^{neq}, the equilibrium function f_1^{eq} must be known. For this reason, using Eqs. 4.82 and 4.83 the inlet velocity $u_{x,in}$ is calculated as

$$u_{x,in} = 1 - \frac{f_0 + f_2 + f_4 + 2\left(f_3 + f_6 + f_7\right)}{\rho_{in}}. \tag{4.85}$$

Now, the non-equilibrium bounce-back equation can be written at the inlet as

$$f_1 - f_1^{eq} = f_3 - f_3^{eq}. \tag{4.86}$$

The equilibrium distribution functions f_1^{eq} and f_3^{eq} are

$$f_1^{eq} = \rho_{in}\left(\frac{1}{9} + \frac{u_{x,in}}{3} - \frac{u_{x,in}^2}{6}\right) \tag{4.87}$$

and

$$f_3^{eq} = \rho_{in}\left(\frac{1}{9} - \frac{u_{x,in}}{3} - \frac{u_{x,in}^2}{6}\right). \tag{4.88}$$

From Eqs. 4.86, 4.87 and 4.88 f_1 results

$$f_1 = f_3 + \frac{2}{3}\rho_{in}u_{x,in} \tag{4.89}$$

and from Eqs. 4.83 and 4.84

$$f_5 = f_7 - \frac{1}{2}(f_2 - f_4) + \frac{1}{6}\rho_{in}u_{x,in}, \tag{4.90}$$

$$f_8 = f_8 - \frac{1}{2}(f_2 - f_4) + \frac{1}{6}\rho_{in}u_{x,in}. \tag{4.91}$$

A similar procedure can be applied if a constant velocity $u_{x,in}$ is imposed at the inlet boundary. However, in Eqs. 4.82 and 4.83 ρ_{in} (instead of $u_{x,in}$) is unknown and it can be calculated in the same way of Eq. 4.85 and becomes

$$\rho_{in} = \frac{f_0 + f_2 + f_4 + 2(f_3 + f_6 + f_7)}{1 - u_{x,in}}. \tag{4.92}$$

Then the non-equilibrium bounce-back method is applied in the same way as reported above and results of f_1, f_5 and f_8 reported in Eqs. 4.89 - 4.91 are still valid.

Periodic boundary condition

Periodic boundary conditions apply only to situations where the flow solution is periodic. Applying this boundary condition, the fluid leaving the domain on one side will, instantaneously, reenter at the opposite side. Consequently, periodic boundary conditions conserve mass and momentum at all times.

For the NSEs, periodic boundary conditions are:

$$\rho(\mathbf{x}, t) = \rho(\mathbf{x} + L, t) \tag{4.93}$$

and

$$\rho\,\mathbf{u}(\mathbf{x}, t) = \rho\,\mathbf{u}(\mathbf{x} + L, t), \tag{4.94}$$

where L describes the periodicity direction and length of the flow pattern. The periodic condition is straightforward in the LBM. During propagation, the unknown incoming populations f_i^{post} on one side are given by those leaving the domain at the opposite side:

$$f_i^{post}(\mathbf{x}, t) = f_i^{post}(\mathbf{x} + L, t). \tag{4.95}$$

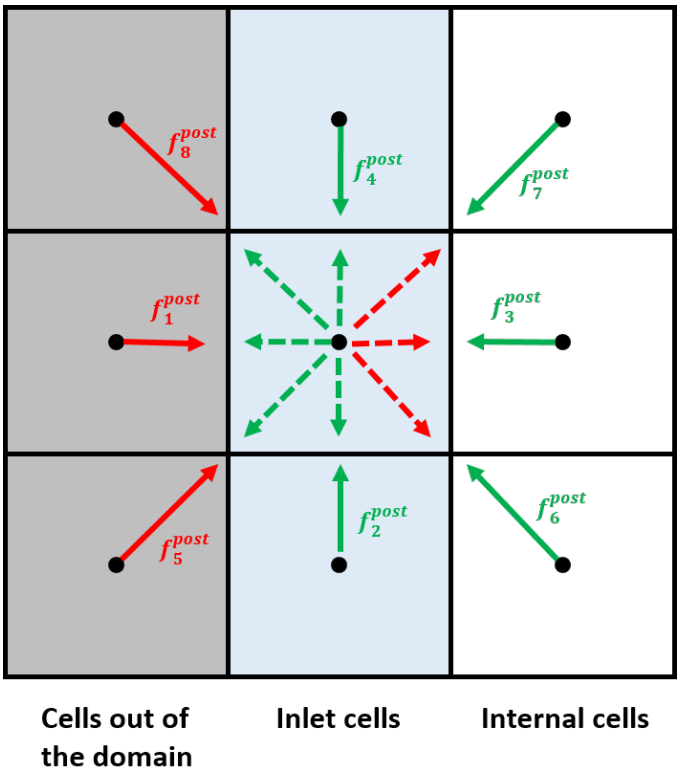

Figure 4.6: Zou-He boundary condition on a inlet boundary. In this case, the first column of cells are the inlet cells and on these cells the boundary condition is applied. After streaming f_2, f_3, f_4, f_6, f_7 (in green) income from the neighbor fluid nodes, while f_1, f_5, f_8 (in red) are unknown. Unknown populations are computed by Eqs. 4.89-4.91. The same approach can be applied to outlet boundaries.

4.3.5 LBM procedure for single-phase fluid flow simulation

In this paragraph it is shown how the LBM was implemented with application to 2D single-phase fluid flow simulation in porous media. We are interested in reaching steady state flow conditions, which are needed for the calculation of tortuosity, effective porosity and permeability (Section 2.3). All the procedure, formed by pre-processing, processing and post-processing, is reported in Fig. 4.8 and discussed in more detail in the following paragraphs.

Pre-processing

In the pre-processing step, the computational grid is generated and the fluid properties such as density, viscosity and relaxation time are assigned. Usually, as represented in Fig. 4.9 for fluid flow simulation in porous media, the geometry is a

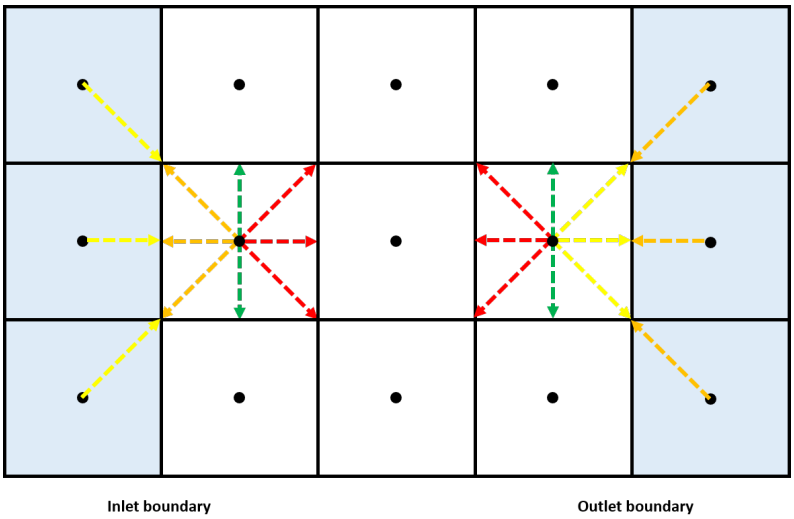

Figure 4.7: Periodic boundary conditions. Unknown populations are computed by Eq. 4.95

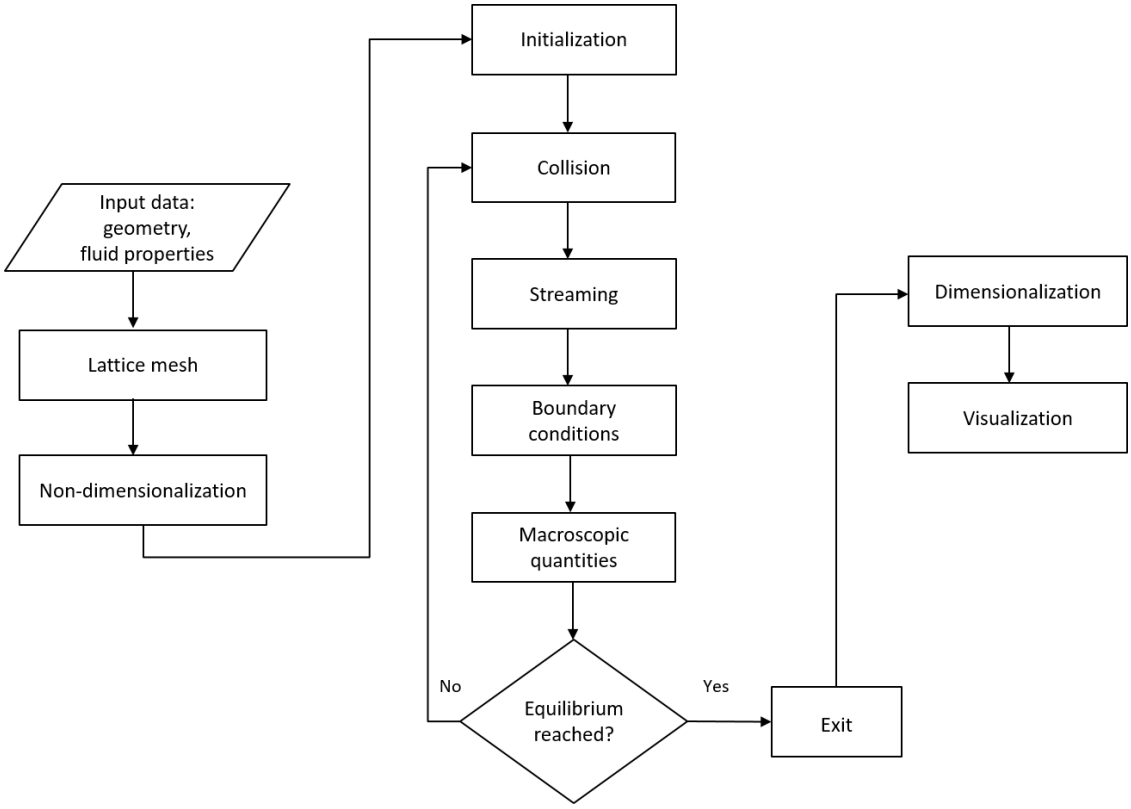

Figure 4.8: Algorithm for single-phase incompressible fluid flow simulation based on the LBM.

binary matrix where 0 is represents the pore space and 1 the solid grains. Furthermore, additional cells are inserted at the inlet and outlet boundaries to facilitate inlet/outlet boundary conditions (Fig. 4.10). At the end of the pre-processing step, all the physical quantities are converted into dimensionless quantities as described in the Section 4.3.3.

In all simulations, the grid is structured and the lattice is squared, as shown in Fig. 4.4, because during the streaming each population has to reach the same position in the neighbor lattice. At each lattice, the D2Q9 velocity scheme (Table 4.1) is used (Fig. 4.9).

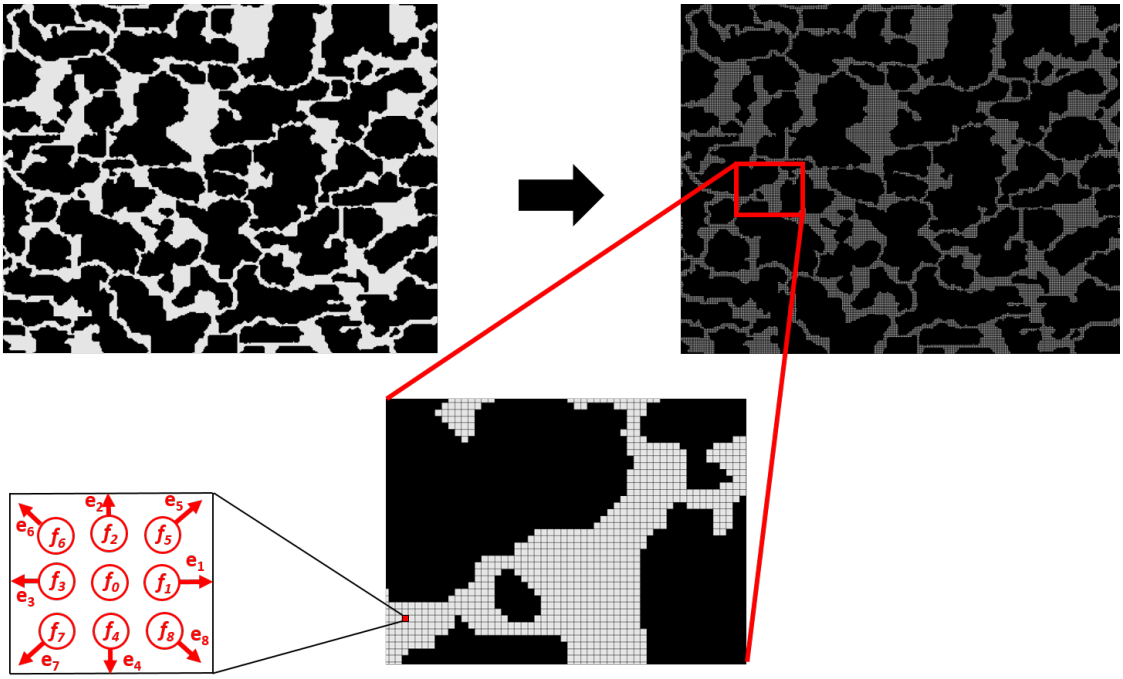

Figure 4.9: LBM grid generated from a binary image. Solid grains (in black) are not considered as computational domain for the calculations. The D2Q9 scheme is used as discrete velocity model.

Simulation

At the beginning of the simulation ($t = 0$), the model is initialized with zero velocity and density everywhere except for the inlet cells, where a nonzero constant density or velocity is imposed (Fig. 4.10).

After the initialization, time iterations start and the following operations are performed during a single time step:

1) Collision (Eq. 4.64), using populations and macroscopic properties from the previous time step.

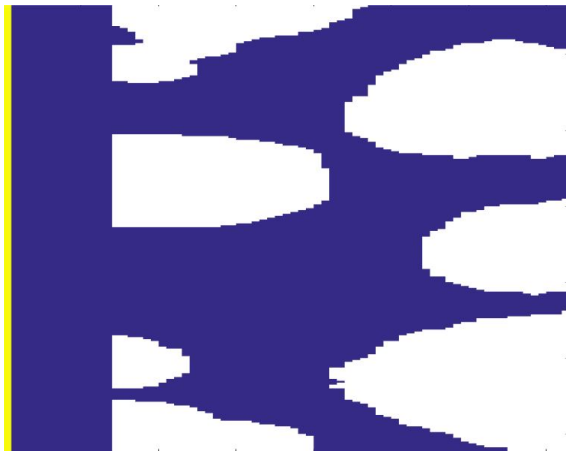

Figure 4.10: Example of simulation initialization with $\rho = 0$ (blue) everywhere except that at the inlet cells where a constant $\rho > 0$ (yellow) is imposed. In this picture the solid grains are represented in white.

2) Streaming of the new post-collision populations f_i^{post} to the neighbor nodes (Eq. 4.65).

3) Boundary conditions are applied for computing missing populations at the fluid-solid and inlet/outlet boundaries (Eqs. 4.78, 4.89-4.91 or 4.95).

4) Calculation of macroscopic properties using Eqs. 4.61, 4.62 and 4.63. Every n iterations specified by the user, density, pressure and velocity values in both x and y directions are saved in a database for post-processing purposes.

5) Check if steady state flow conditions are reached (i.e. the velocity does not change with time), using the velocity criterion [163]

$$\frac{\sum_{i,j}\left|\left(\sqrt{u_i^2+u_j^2}\right)^t-\left(\sqrt{u_i^2+u_j^2}\right)^{t-1}\right|}{\sum_{i,j}\left(\sqrt{u_i^2+u_j^2}\right)^t} < tol, \tag{4.96}$$

where t is the current time step, $t-1$ the previous time step, i and j the two velocity directions and tol is a tolerance to reach for having steady-state flow. If the criterion is satisfied, the algorithm exits the loop, otherwise it continues to iterate and go to $t+1$. Data at the last iteration are automatically saved before leaving the loop. The simulation stops also if the maximum number of iterations is reached.

Post-processing

After the simulation stops, two operations has to be performed:

1) Convert all the quantities from lattice units to physical units.

2) Visualize the results.

At this point the simulation procedure ends and all the data are available.

4.3.6 Validation case: single-phase flow in a 2D microchannel

In order to validate the numerical method for simulating single-phase flow of incompressible fluids, the Poiseuille's flow in a 2D microchannel (Eq. 4.19) was considered. The microchannel has length $L = 6 \times 10^{-4}$ m and height $H = 1.5 \times 10^{-4}$ m. The fluid has a density $\rho = 1050$ kg/m^3 and a viscosity of 1×10^{-3} Pa s (1 cP). A pressure gradient of 80 Pa/m is imposed between the inlet and the outlet in order to induce the fluid flow. Constant pressure boundary conditions were applied by using the Zou-He method. The bounce back boundary conditions was used at fluid-solid boundary. The relaxation time was $\tau = 0.75$. The average velocity is $u_{avg} = 1.5 \times 10^{-4}$ m/s, the maximum velocity $u_{max} = 2.25 \times 10^{-4}$ m/s, the characteristic length $l = H/2 = 7.5 \times 10^{-5}$ m and the Reynolds number Re $= 1.77 \times 10^{-2}$. The non-dimensionalization process is performed using the equations reported in paragraph 4.3.3. In this test, maximum and average velocity are calculated varying the number of lattices in the y direction. Input data and analytical solutions of the quantities of interest are reported in Table 4.3. Five cases are considered: $N_y = 4, 6, 12, 30, 60$ l.u. In Fig. 4.11, the numerical solution is compared to the analytical solution (Eq. 4.19) over a cross section of the channel for $N_y = 60$.

Table 4.3: Input parameters for the simulation of Poiseuille's flow in a 2D microchannel.

H (m)	1.5×10^{-4}
L (m)	6×10^{-4}
$\Delta p/L$ (Pa/m)	80
ρ (kg/m^3)	1050
μ (Pa s)	1×10^{-3}
u_{max} (m/s)	2.25×10^{-4}
u_{avg} (m/s)	1.5×10^{-4}
Re (-)	1.77×10^{-2}

In Fig. 4.11, it is visible that the numerical solution approximates accurately the theoretical behavior of the fluid flow. An estimate of the accuracy was obtained calculating the numerical error of the maximum and average velocities with respect

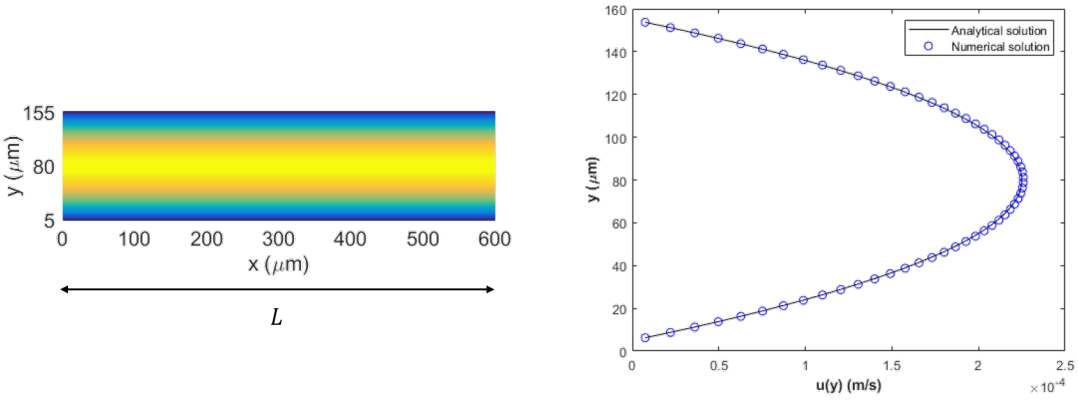

Figure 4.11: Validation of the LBM code for Poiseuille's flow in a 2D microchannel using $N_y = 60$. On the left, the velocity field is represented over the whole domain. On the right, a cross section along y axis where a parabolic velocity profile occurs.

the analytical solution as:

$$E(u) = \left| \frac{u_{an} - u_{num}}{u_{an}} \right| \times 100, \tag{4.97}$$

where $u = u_{max}$ or $u = u_{avg}$. The results are reported in Table 4.4 and Fig. 4.12. The Mach number is calculated by $\mathrm{Ma} = u_{max}/c_s = u_{max}\sqrt{3}$ in lattice units and it was verified to be much smaller than 1 in all the cases, guaranteeing the flow to be into the incrompressible limit. In this test, the minimum resolution able to resolve and describe the fluid flow was investigated. As expected, the results show that that the numerical error decreases increasing the resolution for the two quantities of interest. For resolutions higher than $N_y = 6$ l.u., the numerical error is below 1% in the maximum velocity and smaller than 3% in the average velocity. It should be pointed out that in fluid flow in porous media the average velocity is more significant because it influences the permeability, therefore it must be estimated accurately. For resolutions higher than $N_y = 12$ l.u., the numerical error on the average velocity is smaller than 2% and for $N_y > 30$ smaller than 1%. Since in pore-scale simulations it is rarely possible to have 30 cells on the smallest pore throat because it would be too computationally expensive, an accuracy of around 3% is enough to obtain reliable results and therefore it is necessary to guarantee not less than 4-5 cells in the smallest pore-throat. In conclusion, the numerical method and boundary conditions implemented were able to give accurate solution results. Although not reported here, a larger number of simulations were run for this case in order to check if the correct behavior was well estimated for different space length and varying the pressure gradient.

Finally, it should be noted that the BGK model with bounce-back boundary condition can lead to an incorrect estimate of the permeability. Pan *et al.* [102]

proposed to solve this problem using the Multi-relaxation time in combination with bounce-back boundary. Prestininzi *et al.* [104] also discussed this problem and they showed that the BGK model and bounce back boundary condition leads to a correct estimate of the permeability for Knudsen number (Kn) smaller than 0.01, which correspond to the limit for the continuous flow regime, under which Navier-Stokes equations and Darcy's law are valid. The drawback of keeping Kn $<$ 0.01 is a considerable increasing in computational effort [104].

Table 4.4: Results of the validation test for different mesh resolutions.

	N_y (l.u.)	Δy (m/l.u.)	Ma (-)	$E(u_{max})$	$E(u_{avg})$
Case 1	4	3.75×10^{-5}	1.3×10^{-3}	4.23%	3.56%
Case 2	6	2.5×10^{-5}	1.544×10^{-4}	0.43%	2.95%
Case 3	12	1.25×10^{-5}	1.527×10^{-4}	0.95%	1.78%
Case 4	30	5×10^{-6}	1.5121×10^{-4}	0.65%	0.78%
Case 5	60	2.5×10^{-6}	1.506×10^{-4}	0.37%	0.4%

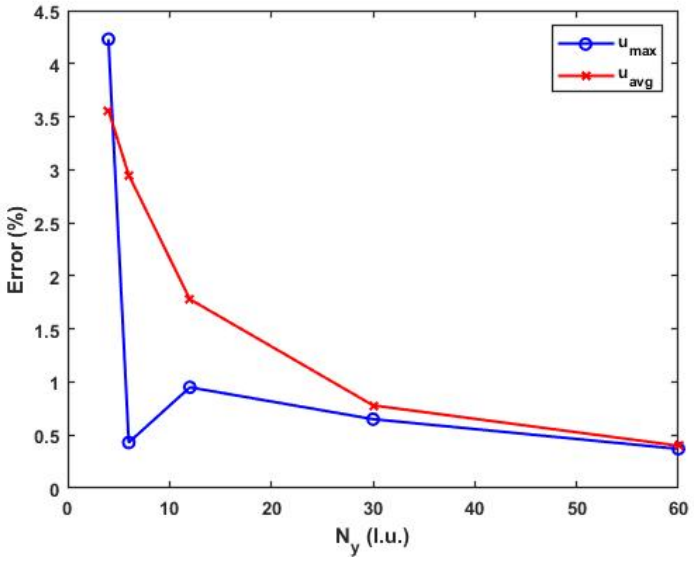

Figure 4.12: Numerical error of the maximum and average velocities computed with the LBM with respect to the analytical values.

4.4 Eulerian grid-based methods

This Section briefly discusses the numerical procedure for solving the incompressible Navier-Stokes equations numerically using Eulerian grid-based methods. The problem is pressure-velocity coupled and requires iterative methods in order

to be solved. In Section 4.4.1 the incompressible NSEs equations are presented in a matrix form and the pressure-velocity coupled problem is introduced. In Paragraph 4.4.2, spatial and temporal terms in the NSEs are discretized using the Finite Volume Method. Finally in Section 4.4.6, the two most popular algorithms for solving the incompressible NSEs (SIMPLE and PISO) are described. In this work, the formulations of FVM and pressure-velocity coupling methods are presented as implemented in OpenFOAM [164]. A more detailed description of these topics can be found in Jasak [164], Versteeg & Malalasekera [165], and Guerrero [166].

4.4.1 Numerical solution of the Navier-Stokes equations

First of all, the incompressible NSEs are rewritten (Eqs. 4.3 and 4.9):

$$\begin{aligned} &\nabla \cdot \mathbf{u} = 0, \\ &\frac{\partial \mathbf{u}}{\partial t} + \nabla \cdot (\mathbf{u}\mathbf{u}) - \nabla \cdot (\nu \nabla \mathbf{u}) - \mathbf{g} = -\nabla p, \end{aligned} \tag{4.98}$$

where ν is the kinematic viscosity, p is the kinematic pressure and $\mathbf{g}$ the gravity acceleration. In Eq. 4.98, we are seeking a solution for the velocity field $\mathbf{u}$ and for the pressure field p. However, the main problem with Eq. 4.98 is that an equation for pressure does not exist and an equation of state (such as $p = \rho RT$) cannot be used in this case because density and temperature are constant. Therefore, in order to resolve the fluid flow, an equation for pressure must be derived from the momentum and continuity equations.

The momentum equation is rewritten in a general matrix form:

$$\mathbf{M}\mathbf{u} = -\nabla p, \tag{4.99}$$

where $\mathbf{u}$ is the unknown velocity field, ∇p the pressure gradient and $\mathbf{M}$ is a matrix of coefficients obtained from the discretization of the differential terms in the NSEs. As shown later, in this work the Finite Volume Method is used for the discretization.

The matrix $\mathbf{M}$ can be decomposed into the matrix $\mathbf{A}$ of diagonal components and the matrix $\mathbf{H}(\mathbf{u})$ of off-diagonal components. The point of this decomposition is that diagonal matrices are easier to invert. The matrix $\mathbf{H}(\mathbf{u})$ is defined as

$$\mathbf{H}(\mathbf{u}) = \mathbf{A}\mathbf{u} - \mathbf{M}\mathbf{u}, \tag{4.100}$$

Then the momentum equation in Eq. 4.99 can be rewritten as

$$\mathbf{A}\mathbf{u} - \mathbf{H}(\mathbf{u}) = -\nabla p, \tag{4.101}$$

from which the velocity can be easily evaluated inverting the diagonal matrix $\mathbf{A}$ as

$$\mathbf{u} = \mathbf{A}^{-1}\mathbf{H}(\mathbf{u}) - \mathbf{A}^{-1}\nabla p. \tag{4.102}$$

The velocity expression in Eq. 4.102 can be used into the continuity equation (i.e. $\nabla \cdot [\mathbf{A}^{-1}\mathbf{H}(\mathbf{u}) - \mathbf{A}^{-1}\nabla p]$) to obtain an equation for pressure

$$\nabla \cdot \left[\mathbf{A}^{-1}\nabla p\right] = \nabla \cdot \left[\mathbf{A}^{-1}\mathbf{H}(\mathbf{u})\right]. \tag{4.103}$$

Eq. 4.103 is called pressure-Poisson equation. Now, a new system of equations, which includes an equation for pressure, equivalent to Eq. 4.98 is derived:

$$\begin{aligned} &\mathbf{A}\mathbf{u} - \mathbf{H}(\mathbf{u}) = -\nabla p, \\ &\nabla \cdot \left[\mathbf{A}^{-1}\nabla p\right] = \nabla \cdot \left[\mathbf{A}^{-1}\mathbf{H}(\mathbf{u})\right]. \end{aligned} \tag{4.104}$$

The two equations reported in 4.104 are pressure-velocity coupled and are solved iteratively ussing pressure-velocity coupled algorithms. SIMPLE and PISO procedures are the most poplar methods for dealing with coupled pressure-velocity systems of equations. The SIMPLE algorithm is used for steady-state problems and the PISO algorithm for transient problems. They are discussed in Section 4.4.6.

In Section 4.4.2, the Finite Volume Method used for the discretization of the terms in Eq. 4.104 is shown.

Before moving to the next Section, a few general considerations about iterative methods for solving systems of linear equations (such as $\mathbf{M}\mathbf{u} = -\nabla p$) are presented. In order to guarantee convergence, iterative solvers require the matrix of coefficients to be diagonally dominant, which means that, for every row of the matrix, the magnitude of the diagonal coefficient is higher or equal to the sum of the off-diagonal elements ($|a_P| > \sum_N |a_N|$) [164]. Then, the diagonal dominance of the of the system should be increased in order to improve the convergence. As shown later, there are terms that tend to increase the diagonal dominance of the matrix and therefore improve the convergence and the stability (the temporal derivative or source terms), and others that reduce it (non-orthogonal corrections). When diagonal dominance is not guaranteed, it is necessary to under-relax matrix the coefficients in order to use iterative solvers.

4.4.2 Finite Volume discretization

The Finite Volume Method (FVM) is a discretization method (such as the Finite Difference Method or the Finite Element Method), that transform a partial differential equation into a set of algebraic equations that can be solved numerically using iterative algorithms. In general, a system of algebraic equations can be written in a matrix form as

$$\mathbf{M}\mathbf{u} = \mathbf{b}, \tag{4.105}$$

where $\mathbf{M}$ is the matrix of coefficients, $\mathbf{u}$ is the vector of unknown variables and $\mathbf{b}$ is the vector of known terms. At this stage, two more considerations are necessary. The variable $\mathbf{u}$ is considered as implicit if it is unknown and therefore it is a

solution of the Eq. 4.105; it will be referred to an implicit contribution using the superscript n (e.g. $\mathbf{u}^n$). The variable $\mathbf{u}$ is considered as explicit if it is known from the previous time step and therefore it is included in $\mathbf{b}$; it will be referred to an explicit contribution using the superscript $n-1$ (e.g. $\mathbf{u}^{n-1}$). This distinction is important in the computation of the discretize terms in the NSEs [164].

In order to introduce the FVM, we consider the general form of the transport equation for an arbitrary variable φ:

$$\frac{\partial(\rho\varphi)}{\partial t} + \nabla \cdot (\rho\mathbf{u}\varphi) = \nabla \cdot (\rho\Gamma\nabla\varphi) + S(\varphi), \tag{4.106}$$

where $\mathbf{u}$ is the fluid velocity and Γ is the constant diffusion coefficient. In Eq. 4.106, on the left hand side, the two terms are the temporal derivative and the convection term of φ respectively, while on the right hand side, the two terms are the diffusion term and the source term respectively.

Note that the Navier-Stokes equations can be obtained from Eq. 4.106. In fact, in Eq. 4.106, if $\varphi = 1$, $\Gamma = 0$ and $S(\varphi) = 0$, the continuity equation is obtained:

$$\frac{\partial\rho}{\partial t} + \nabla \cdot (\rho\mathbf{u}) = 0, \tag{4.107}$$

and if $\varphi = \mathbf{u}$, $\Gamma = \nu$ and $S(\varphi) = S - \nabla p$, the momentum equation is obtained

$$\frac{\partial(\rho\mathbf{u})}{\partial t} + \nabla \cdot (\rho\mathbf{u}\mathbf{u}) = \nabla \cdot (\mu\nabla\mathbf{u}) - \nabla p + S. \tag{4.108}$$

In the FVM, the spatial domain is discretized in control volumes, or cells, to form a mesh where the quantities (e.g. pressure, velocity and temperature) live [165]. The control volumes can have any shape, however they require the cell faces to be planar. An example of a control volume V_P is represented in Fig. 4.13. The point P is called centroid and f is called face center, and they are defined as

$$\int_{V_P} (\mathbf{x} - \mathbf{x}_P)\, dV = 0 \tag{4.109}$$

and

$$\int_{S_f} (\mathbf{x} - \mathbf{x}_f)\, dS = 0. \tag{4.110}$$

In Fig. 4.13, The point N is the centroid of the neighbor control volume V_N and $\mathbf{d}$ is the distance vector from P to N. The cell having centroid P is called owner cell and the cell having centroid N is called neighbor cell. The point f_i denotes the intersection between $\mathbf{d}$ and the cell face. The vector $\mathbf{S}_f = \hat{\mathbf{n}}_f S$ is the normal surface unit vector and points outwards the control volume.

Finally, second-order (linear) approximations of the differential terms are requested (second-order FVM). Therefore, it is assumed that the values of the variables vary linearly across the cell. This is equivalent to approximate the cell value

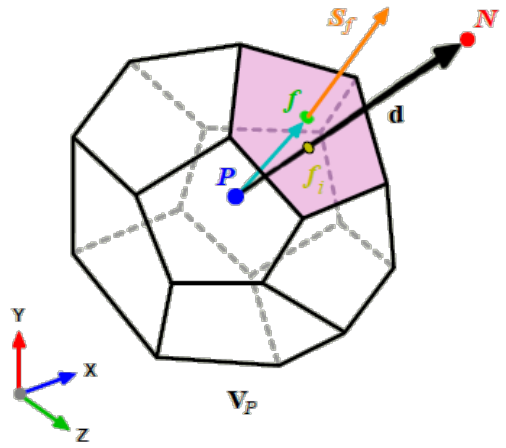

Figure 4.13: Control volume [166]. The control volume has a volume V constructed around the point P, which is the centroid of the control volume. The vector from P to the centroid N of the neighboring control volume is named $\mathbf{d}$. The control volume faces are labeled f. The location where the vector $\mathbf{d}$ intersects a face is f_i. The face area vector $\mathbf{S}_f$ points outwards the control volume and it is located at the face centroid normal to the face.

in the control volume the value at the centroid (average value):

$$\varphi_P = \frac{1}{V_P} \int \varphi(\mathbf{x})\, dV. \tag{4.111}$$

In the same way, the values of the variables on the cell face are stored at the face center and are calculated as the average value of the variable over the cell face:

$$\varphi_f = \frac{1}{A_f} \int \varphi(\mathbf{x})\, dA. \tag{4.112}$$

4.4.3 Discretization of gradient and divergence operators

Here, it is shown how to evaluate the gradient of a generic variable φ at the cell centroid P, i.e. $(\nabla\varphi)_P$. The knowledge of $(\nabla\varphi)_P$ will be needed in the scheme for the discretization of the convection term, for the non-orthogonal corrections in the diffusion term and for the discretization of the pressure gradient term. The gradient is obtained from the generalized form of the Gauss theorem and Eq. 4.112 respectively as [164]:

$$\int_{V_P} \nabla\varphi\, dV = \oint_{\partial V_P} d\mathbf{S}_f\, \varphi = \sum_f \int_f d\mathbf{S}\, \varphi = \sum_f \mathbf{S}_f\, \varphi_f. \tag{4.113}$$

Using Eq. 4.111, it can be written as

$$(\nabla\varphi)_P = \frac{1}{V_P}\sum_f \mathbf{S}_f\,\varphi_f. \tag{4.114}$$

In the same way, the Gauss theorem can be applied also for discretizing the divergence operator at the cell centroid P [164], obtaining

$$(\nabla\cdot\mathbf{a})_P = \frac{1}{V_P}\sum_f \mathbf{S}_f\cdot\mathbf{a}_f, \tag{4.115}$$

where $\mathbf{a}$ is a generic vectorial field. Eq. 4.115 can be applied straightforward to the discretization of the continuity equation ($\nabla\cdot\mathbf{u}=0$). In fact, substituting $\mathbf{a}$ with the velocity field $\mathbf{u}$, the discretized form of the continuity equation on the cell is

$$\sum_f \mathbf{S}_f\cdot\mathbf{u}_f = 0, \tag{4.116}$$

where $\mathbf{S}_f\cdot\mathbf{u}_f$ is the volumetric flux across the cell face. From Eq. 4.116, it is visible that when the continuity equation is satisfied, the fluxes across the cell face are conserved. This is an important property of the FVM.

4.4.4 Discretization of the momentum equation

In this Section, the discretization of the terms in the momentum equation is discussed. The FVM requires that the incompressible NSEs (Eq. 4.98) are satisfied over the control volume V_P in the integral form [164]:

$$\begin{aligned}&\int_t^{t+\Delta t}\left[\frac{\partial}{\partial t}\int_{V_P}\mathbf{u}\,dV + \int_{V_P}\nabla\cdot(\mathbf{uu})\,dV - \int_{V_P}\nabla\cdot(\nu\nabla\mathbf{u})\,dV\right]dt = \\ &\int_t^{t+\Delta t}\left[\int_{V_P}-\nabla p\,dV + \int_{V_P}\mathbf{g}\,dV\right]dt.\end{aligned} \tag{4.117}$$

The discretization of Eq. 4.117 is shown term by term. Second-order accuracy must be guaranteed in the discretization of spatial and temporal terms.

Convection term

Using the divergence theorem, the volumetric integral over V_P is transformed into a surface integral over the control volume boundary faces ∂V_P as:

$$\int_{V_P}\nabla\cdot(\mathbf{uu})\,dV = \oint_{\partial V_P} d\mathbf{S}\cdot(\mathbf{uu}), \tag{4.118}$$

Now, Eq. 4.112 is applied to obtain

$$\sum_f\int_f d\mathbf{S}\cdot(\mathbf{uu})_f = \sum_f \mathbf{S}_f\cdot(\mathbf{uu})_f = \sum_f F\mathbf{u}_f, \tag{4.119}$$

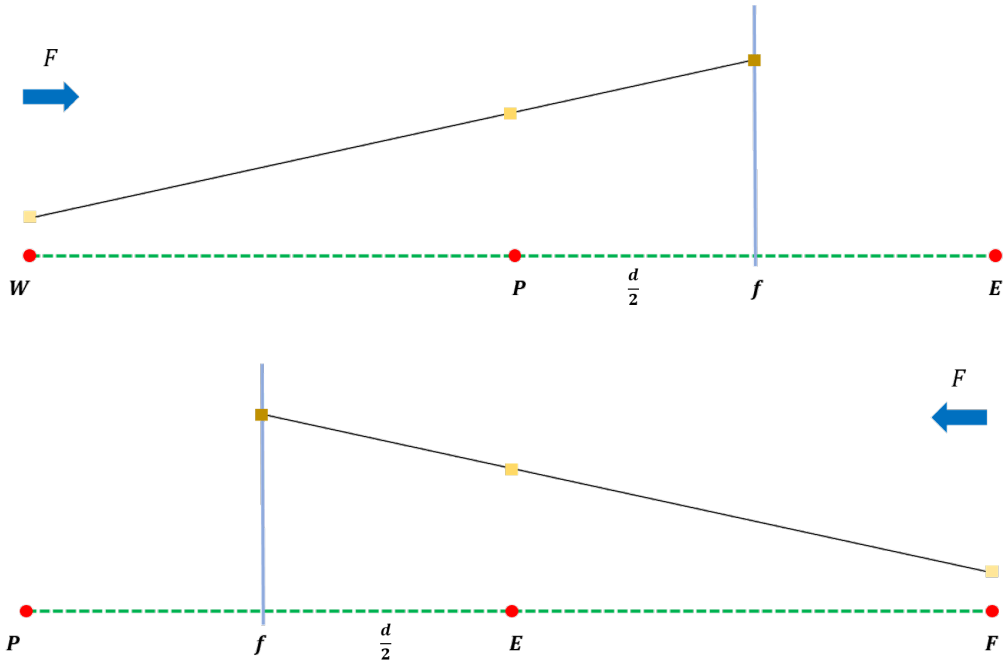

Figure 4.14: Linear upwind scheme for the convection term.

where $\mathbf{S}_f \cdot \mathbf{u}_f = F$ is the volume flux through the cell face. In order to calculate $\mathbf{u}_f$, we focus on the Linear Upwind Differencing (LUD) method, which is a second-order accurate scheme.

In order to introduce the LUD scheme, we consider two cells in a structured 1D mesh with centroids named P and E as represented in Fig. 4.14. Our purpose is to evaluate the velocity on the cell face $\mathbf{u}_f$. The LUD scheme takes into account the gradient between the two centroids upstream f. In this simple case, the LUD scheme can be formulated as

$$\mathbf{u}_f = \begin{cases} \mathbf{u}_P + \frac{1}{2}(\mathbf{u}_P - \mathbf{u}_W) & F > 0 \\ \\ \mathbf{u}_E + \frac{1}{2}(\mathbf{u}_E - \mathbf{u}_F) & F < 0 \end{cases}, \tag{4.120}$$

Referring to Fig. 4.15, the LUD scheme in Eq. 4.120 can be generalized for general 3D meshes using the method proposed by Barth & Jespersen [167]:

$$\mathbf{u}_f = \begin{cases} \mathbf{u}_P + \psi_f (\nabla \mathbf{u})_P \cdot \mathbf{d}_{Pf} & F > 0 \\ \\ \mathbf{u}_N + \psi_f (\nabla \mathbf{u})_N \cdot \mathbf{d}_{Nf} & F < 0 \end{cases}, \tag{4.121}$$

where ψ_f is called gradient limiter and $0 < \psi_f < 1$. In fact, sometimes the computed gradient might be too steep, producing a velocity at the cell face greater than

the velocities of the two neighbor cells (i.e. $\mathbf{u}_P$ and $\mathbf{u}_N$), causing instabilities in the solution. In this case, the role of the gradient limiter is to reduce the values of the gradient and stabilize the simulation. Finally, the LUD scheme requires the discretization of the gradient at the cell centroid ($(\nabla\varphi)_P$ or $(\nabla\varphi)_N$); how to compute this gradient is discussed in Section 4.4.3.

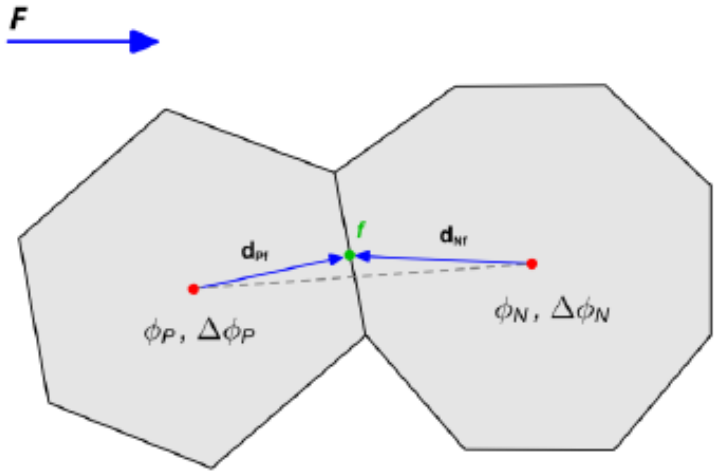

Figure 4.15: Generalization of the linear upwind scheme for the convection term for unstructured meshes [166].

In Eq. 4.121, it is evident that both the owner cell P and all the neighbor cells N contribute to the convection term. Furthermore, the velocities of the convection term are evaluated implicitly and therefore they contribute to fill the $\mathbf{M}$ matrix of coefficients. For the convection term, a triagonal matrix (which reflects the connectivity between owner and neighbor cells) will be created, having the owner cells P on the diagonal and the neighbor cells N off the diagonal. Formally, it can expressed as

$$m_P \mathbf{u}_P^n + \sum_N m_N \mathbf{u}_N^n, \tag{4.122}$$

where m_P and m_N are the diagonal and off-diagonal coefficients of $\mathbf{M}$, respectively.

Diffusion term

As for the convection term, the volumetric integral of the convection term is transformed into a surface integral by the divergence theorem:

$$\int_{V_P} \nabla \cdot (\nu \nabla \mathbf{u})\, dV = \oint_{\partial V_P} d\mathbf{S} \cdot (\nu \nabla \mathbf{u})\,. \tag{4.123}$$

The discretized form of Eq. 4.123 is

$$\sum_f \int_f d\mathbf{S} \cdot (\nu \nabla \mathbf{u})_f = \sum_f \mathbf{S}_f \cdot (\nu \nabla \mathbf{u})_f = \sum_f \nu_f \mathbf{S}_f \cdot (\nabla \mathbf{u})_f, \tag{4.124}$$

where ν_f is obtained by central differencing at the cell face. Central differencing is second-order accurate.

In orthogonal meshes, i.e. vectors $\mathbf{d}$ and $\mathbf{S}$ in Fig. 4.16 are parallel, the gradient term at the cell face $(\nabla \mathbf{u})_f$ is discretized by central differencing:

$$\mathbf{S}_f \cdot (\nabla \mathbf{u})_f = |\mathbf{S}_f| \frac{\mathbf{u}_N - \mathbf{u}_P}{|\mathbf{d}|}. \tag{4.125}$$

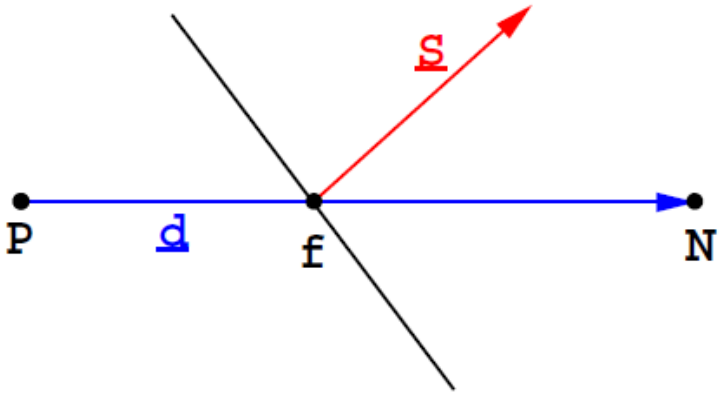

Figure 4.16: Vectors $\mathbf{d}$ and $\mathbf{S}$ on a non-orthogonal mesh [164].

In non-orthogonal meshes, Fig. 4.16, non-orthogonality has to be taken into account. As shown in Fig. 4.17, the $\mathbf{S}_f$ is evaluated as the sum of two parts:

$$\mathbf{S}_f = \mathbf{\Delta}_\perp + \mathbf{k}, \tag{4.126}$$

where $\mathbf{\Delta}_\perp$ is the component parallel to $\mathbf{d}$ and $\mathbf{k}$ is the non-orthogonal component. In this way, the dot product $\mathbf{S}_f \cdot (\nabla \mathbf{u})_f$ in Eq. 4.125 is split into two parts:

$$\mathbf{S}_f \cdot (\nabla \mathbf{u})_f = |\mathbf{\Delta}_\perp| \frac{\mathbf{u}_N - \mathbf{u}_P}{|\mathbf{d}|} + \mathbf{k} \cdot (\nabla \mathbf{u})_f \,, \tag{4.127}$$

where, on the right hand side, the first part is the orthogonal contribution and the second part the non-orthogonal contribution. The gradient in the non-orthogonal contribution is calculated as shown in Eq. 4.114.

In Eq. 4.127, the orthogonal contribution is treated implicitly because both $\mathbf{u}_P$ and $\mathbf{u}_N$ are unknown. As discussed for the convection term, $\mathbf{u}_P$ represents the diagonal components and $\mathbf{u}_N$ the off-diagonal components. Therefore, the orthogonal contribution of the diffusion term tends to improve the overall stability of the

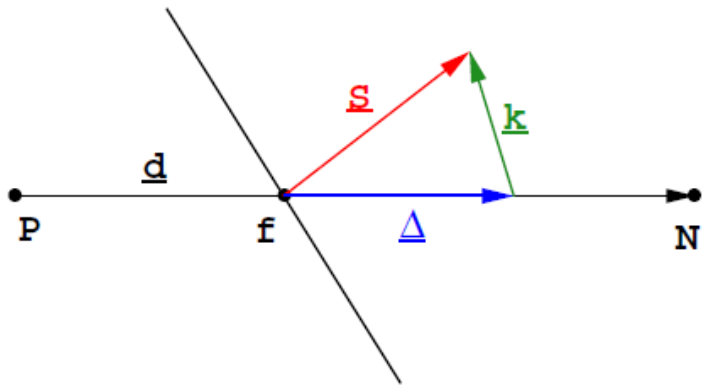

Figure 4.17: Non-orthogonality treatment in the orthogonal correction approach [164].

solution procedure. On the contrary, the non-orthogonal contribution is evaluated explicitly and it is added to the source term. Since explicit terms increase instability, the non-orthogonal term should be as small as possible. Note that higher the non-orthogonal term, higher the explicit term and, as a consequence, smaller the implicit term (orthogonal contribution). This is the reason why it is important to have a mesh as good as possible.

Source term

The source term in Eq. 4.117 is the gravitational acceleration and it is a constant vector $\mathbf{g}$. Integrating $\mathbf{g}$ over the control volume, it becomes

$$\int_{V_P} \mathbf{g}\, dV = \mathbf{g}\, V_P. \tag{4.128}$$

Clearly, in this expression there is no dependency to the velocity field, then this source term will be added to the vector $\mathbf{s}$ of the known terms in Eq. 4.105.

Even if this is the most common form of the source term in incompressible NSEs, it is worth mentioning a more general form of the source term. In general, the source term the source term $S(\mathbf{u})$ can be linearized, i.e. $S(\mathbf{u}) = S_p + S_u\mathbf{u}$. In this case, Eq. 4.111 is applied, obtaining

$$\int_{V_P} S(\mathbf{u})\, dV = \int_{V_P} [S_p + S_u\mathbf{u}]\, dV = S_p V_P + S_u V_P \mathbf{u}_P. \tag{4.129}$$

The term proportional to the velocity can be treated in two different ways, depending on the sign of the source term. If the source terms has a negative sign, it is treated implicitly because it contributes to increase the diagonal dominance of the matrix $\mathbf{M}$. However, if it has a positive sign it is treated explicitly and it is added to the known term vector $\mathbf{s}$ because it would reduce the diagonal dominance of $\mathbf{M}$.

Temporal discretization

In order ensure second-order approximation in time, linear variation of the generic property φ over the time interval between t and $t + \Delta t$ is assumed [164]:

$$\varphi(t + \Delta t) = \varphi(t) + \frac{\partial \varphi(t)}{\partial t} \Delta t. \tag{4.130}$$

Furthermore, $\varphi(t + \Delta t)$ is denominated as φ^n and $\varphi(t)$ as φ^{n-1}.

Assuming that the control volume does not change in time, the temporal derivative term in Eq. 4.117 becomes

$$\int_t^{t+\Delta t} \frac{\partial}{\partial t} \left(\int_{V_P} \mathbf{u} \, dV \right) dt = \int_t^{t+\Delta t} \left(\frac{\partial \mathbf{u}}{\partial t} \right)_P V_P \, dt = \left(\mathbf{u}_P^n - \mathbf{u}_P^{n-1} \right) V_P. \tag{4.131}$$

The temporal variation of centroid values, face values and gradients are neglected [135]. They are assumed to be constant during a time step [136]. Considering that all terms are treated implicitly, the discretized from of Eq. 4.117 in the P cell centroid can be written as:

$$\begin{aligned} &\left(\mathbf{u}_P^n - \mathbf{u}_P^{n-1} \right) V_P + \sum_f F \mathbf{u}_f^n \, \Delta t - |\boldsymbol{\Delta}_\perp| \frac{\mathbf{u}_N^n - \mathbf{u}_P^n}{|\mathbf{d}|} \Delta t + \mathbf{k} \cdot \left(\nabla \mathbf{u}^{n-1} \right)_f \Delta t - \\ &- \mathbf{g} \, V_P \, \Delta t = - \frac{1}{V_P} \sum_f \mathbf{S}_f \, p_f^n \, \Delta t. \end{aligned} \tag{4.132}$$

Discretized momentum equation

Eq. 4.132 can be rearranged dividing by Δt and writing all the implicit terms on the right hand side of the equation and the explicit terms plus the source term on the right hand side:

$$\begin{aligned} &\frac{\mathbf{u}_P^n V_P}{\Delta t} + \sum_f F \mathbf{u}_f^n - |\boldsymbol{\Delta}_\perp| \frac{\mathbf{u}_N^n - \mathbf{u}_P^n}{|\mathbf{d}|} + \frac{1}{V_P} \sum_f \mathbf{S}_f \, p_f^n = \\ &= \frac{\mathbf{u}_P^{n-1} V_P}{\Delta t} - \mathbf{k} \cdot (\nabla \mathbf{u})_f^{n-1} + \mathbf{g} \, V_P. \end{aligned} \tag{4.133}$$

Grouping all the explicit terms on the right hand side of the equation into $\mathbf{b}_P$, Eq. 4.133 can be written in matrix form as

$$a_P \mathbf{u}_P^n + \sum_N a_N \mathbf{u}_N^n + \sum_f \mathbf{S}_f \, p_f^n = \mathbf{b}_P. \tag{4.134}$$

The $\mathbf{H}(\mathbf{u})$ matrix contains the off-diagonal coefficients $\sum_N a_N \mathbf{u}_N^n$ and the source terms $\mathbf{b}_P$:

$$\mathbf{H}(\mathbf{u}) = - \sum_N a_N \mathbf{u}_N^n + \mathbf{b}_P. \tag{4.135}$$

Eq. 4.134 can be rearranged using Eq. 4.135 as

$$a_P \mathbf{u}_P^n + \mathbf{H}(\mathbf{u}) = -\sum_f \mathbf{S}_f \, p_f^n. \tag{4.136}$$

This is the discretized form of Eq. 4.101. From Eq. 4.136, the discretized from of Eq. 4.102 can be expressed as

$$\mathbf{u}_P^n = \frac{\mathbf{H}(\mathbf{u})}{a_P} - \frac{1}{a_P} \sum_f \mathbf{S}_f \, p_f^n. \tag{4.137}$$

4.4.5 Discretization of the pressure equation

The pressure-Poisson equation (Eq. 4.103) can be discretized using Eq. 4.134 and applying the schemes reported in Section 4.4.3 as [164]:

$$\sum_f \mathbf{S}_f \cdot \left[\frac{1}{a_P} \sum_f \mathbf{S}_f \, p_f^n \right]_f = \sum_f \mathbf{S}_f \cdot \left[-\frac{1}{a_P} \left(\sum_N a_N \mathbf{u}_N^n + \mathbf{b}_P \right) \right]_f, \tag{4.138}$$

or

$$\sum_f \mathbf{S}_f \cdot \left[\frac{1}{a_P} \sum_f \mathbf{S}_f \, p_f^n \right]_f = \sum_f \mathbf{S}_f \cdot \left[-\frac{\mathbf{H}(\mathbf{u})}{a_P} \right]_f. \tag{4.139}$$

4.4.6 Pressure-velocity coupling algorithms

In order to calculate pressure and velocity fields, Eq. 4.136 and Eq. 4.139 must be solved. For this purpose, PISO and SIMPLE algorithms are used for transient and steady-state problems respectively [164]. Since this is a coupled problem, the two equations are solved in sequence and iteratively. Before going into detail, two major assumptions valid for both algorithms are pointed out: in Eq. 4.136, the $\mathbf{H}(\mathbf{u})$ matrix and the pressure gradient are evaluated explicitly:

$$a_P \mathbf{u}_P^n + \mathbf{H}(\mathbf{u}) = -\sum_f \mathbf{S}_f \, p_f^{n-1}. \tag{4.140}$$

where

$$\mathbf{H}(\mathbf{u}) = -\sum_N a_N \mathbf{u}_N^{n-1} + \mathbf{b}_P. \tag{4.141}$$

4.4.7 PISO

The PISO algorithm (Fig. 4.18) was proposed by Issa [134] and it is used for transient calculations.

1) **Momentum predictor**. The momentum equation (Eq. 4.140) is solved. At this stage, the pressure from the previous time step (or from initial conditions) is used. The velocity at this stage does not satisfy the continuity.

2) **Pressure solution**. Using the predicted velocities, the pressure equation (Eq. 4.139) is solved. The obtained pressure gives an estimate of the new pressure field.

3) **Momentum corrector**. The pressure obtained in the step 2 is used to correct the velocity field using Eq. 4.137. Now the velocity satisfy the continuity.

At the end of step 3, the pressure has to be recalculated because the velocity has changed and therefore $\mathbf{H}(\mathbf{u})$ has changed. Therefore, $\mathbf{H}(\mathbf{u})$ is corrected and the new pressure equation (step 2) is formulated.

In other words, at each time step, the PISO algorithm consists of one momentum predictor followed by a series of pressure solutions and momentum correctors. If there is high non-orthogonality, non-orthogonality loops has to be performed over the pressure equation [166]. Finally, it is important to mention that the PISO loop requires a small number of iterations (usually less than 10) to converge, especially when the time step size is small and the diagonal dominance of the matrix is increased; this is an important characteristic of this algorithms because it allows solve the equations over a large number of time steps in an acceptable amount of time.

4.4.8 SIMPLE

The SIMPLE (Fig. 4.18) algorithm was proposed by Patankar [135] and it is used for solving steady state problems.

1) **Momentum predictor**. As in PISO, the first step is the momentum predictor. However, since in steady-state simulations the temporal derivative is not present, Eq. 4.140 is under-relaxed in order to increase the diagonal dominance of the matrix [164]:

$$\frac{1}{\alpha} a_P \mathbf{u}_P^n = \mathbf{H}(\mathbf{u}) - \sum_f \mathbf{S}_f \, p_f^{n-1} + \frac{1-\alpha}{\alpha} a_P \mathbf{u}_P^{n-1}, \tag{4.142}$$

where α is the under-relaxation coefficient between 0 and 1. The pressure gradient is computed using the pressure distribution from the previous iteration or from an initial guess.

2) **Pressure solution**. The pressure equation (Eq. 4.139) is formulated and solved in order to obtain the new pressure field.

3) **Momentum corrector**. The velocity is corrected using Eq. 4.137.

At the end of step 3, the matrix $\mathbf{H}(\mathbf{u})$ has to be recalculated with the new velocity field and therefore the pressure needs to be recomputed as well. Differently from PISO, here the process restarts from the momentum predictor step (step 1) and iterations continue until the tolerance is reached.

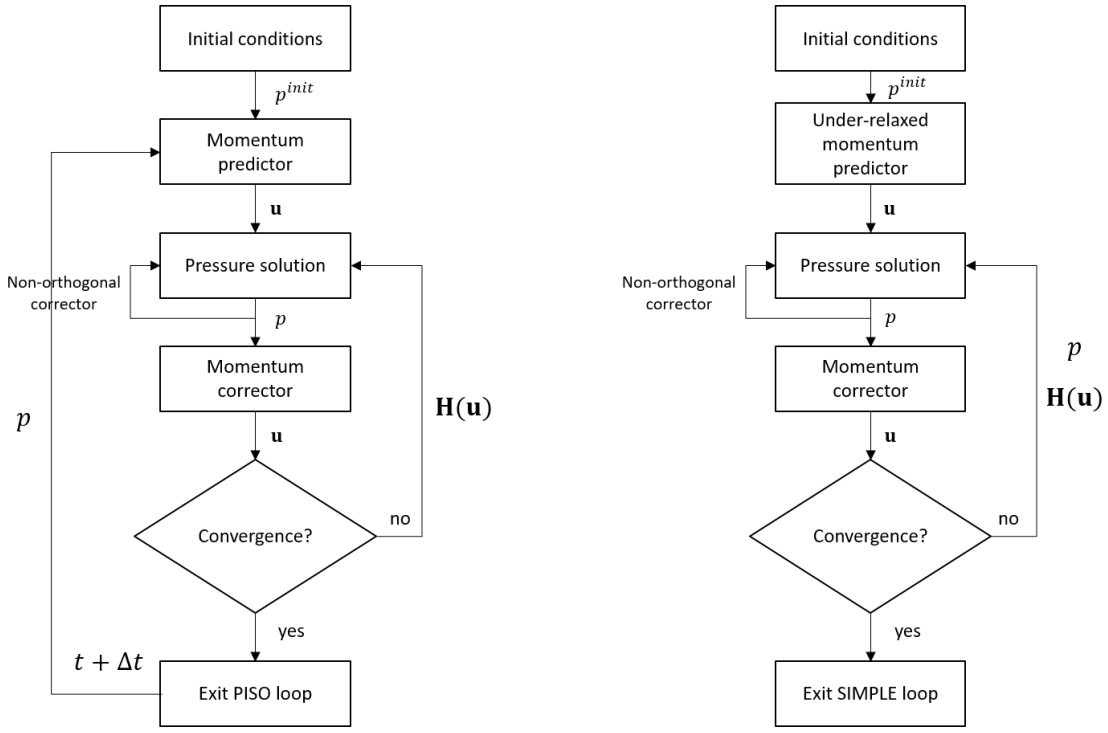

Figure 4.18: PISO (left) and SIMPLE (right) algorithms.

4.4.9 Boundary conditions

Three types of boundary conditions exist [166]: 1) Dirichlet (or fixed value) boundary conditions, which fix the value of the variable on the physical boundary (i.e. $\varphi = \varphi_b$ at the boundary b), 2) Neumann (or fixed gradient) boundary condition, which prescribes the value of the gradient of the variable normal to the physical boundary (i.e. $(\nabla\varphi)_b = g_b$ at the boundary b), and 3) Robin (or mixed) boundary condition, which mixes Dirichlet and Neumann boundary conditions. In the model, physical boundaries (e.g. walls, inlet, outlet, symmetry plane) are associated with a set of boundary conditions for each variable calculated [164].

Here, we report the most common boundary conditions used at inlet, outlet and wall boundaries in CFD applications:

1) **Inlet boundary**: three configurations are mainly used.

- fixed value boundary condition for the velocity and zero gradient boundary condition for the pressure. This boundary conditions is the most stable when used in combination with the outlet boundary condition reported below, but the less representative from the physical point of view.
- fixed flow rate, which is translated into a velocity profile, and zero gradient boundary condition for the pressure. This configuration is useful if a comparison with laboratory experiments is needed.
- zero gradient boundary condition for the velocity and fixed value boundary condition for the pressure. Also this configuration is realistic in laboratory flow experiments, where a pressure gradient between inlet and outlet is applied to move the fluid.

2) **Outlet boundary**: fixed value boundary condition for pressure and zero gradient zero gradient boundary condition for velocity.

3) **No-slip wall**: fixed value boundary condition for the velocity set to zero (the wall is not moving) and zero gradient boundary condition for pressure.

4) **Symmetry**: when the geometry (and the flow) has a symmetry, it is possible to insert a symmetry plane and simulate only half of the domain. The component of the gradient normal to the symmetry plane is fixed to zero, and the component parallel to the symmetry plane are projected from inside the domain to the boundary face.

4.5 Estimate of hydrodynamic parameters

This paragraph discusses the methodology based on hydrodynamic modeling proposed in this work to estimate the rock parameters showed in Section 2.3, i.e. tortuosity, effective porosity and permeability. To this end, both the LBM and the FVM can be used.

The hydraulic tortuosity was defined by Carman [55] as the ratio of the average length of the fluid paths divided by the length of the sample:

$$\tau_{h,i} = \frac{\langle L_{h,i} \rangle}{L_i} \quad \text{where} \quad i = x, y, z. \tag{4.143}$$

Clennell [56] suggested a kinematical average in which the path lines were weighted with fluid flow velocities. Later, Koponen *et al.* [57] suggested to calculate the hydraulic tortuosity in a fixed direction i using the velocity field calculated by direct numerical simulation in the pore space:

$$\tau_{h,i} = \frac{\langle |u| \rangle}{\langle u_i \rangle} \quad \text{where} \quad i = x, y, z \tag{4.144}$$

where $|v|$ is the absolute value of the local flow velocity, v_i is the i-th component of that velocity and $\langle\rangle$ denotes the spatial average over the pore space. Here, the LBM and the FVM were used to simulate the fluid flow in porous media at the pore-scale and obtain the velocity field and calculate the hydraulic tortuosity ($\tau_{h,i}$) with Eq. 4.144. It was verified that the tortuosity value does not change varying the pressure gradient until laminar flow conditions are guaranteed, i.e. Re ≤ 2 [168], where the Reynolds number Re was calculated as [7]:

$$\mathrm{Re} = \frac{\rho\, U\, d_c}{\mu}, \tag{4.145}$$

where d_c is the characteristic length, ρ and μ are the density and the dynamic viscosity of the fluid respectively and U is the averaged velocity over the porous medium. There are several ways to define the characteristic length in a porous medium: sometimes it is equal to the grain diameter [7], others it involves the hydraulic radius (or hydraulic diameter)[169–171]. Here, the image-based definition introduced by Mostaghimi *et al.* [172] and later proposed by Blunt [8] was adopted:

$$d_c = \pi \frac{V_b}{S_w} = \pi \frac{r_H}{\phi}, \tag{4.146}$$

where V_b is the total volume of the bulk system (pore and grain) and S_w is the wetted surface (surface area between grain and void). Eq. 4.146 represents a sort of average grain size diameter. In 2D, r_H is replaced by $r_{H,2D}$ and ϕ by ϕ_{2D}.

For comparison with the geometrical approach, the effective porosity can be calculated using the hydrodynamic paths by [57]:

$$\phi_{eh,i} = \frac{N_{s,i}}{N_{l,i}} \quad \text{where} \quad i = x, y, z \tag{4.147}$$

where, according to Koponen *et al.* [57], N_s is the number of grid cells crossed by streamlines and N_l is the total number of grid cells. To reduce the computational effort, we calculated the effective porosity by applying a cutoff on the local velocity $|u|$ obtained by numerical simulations. A preliminary analysis on the velocity field distribution showed that the velocities of one order of magnitude lower than average velocity value were not significantly contributing to the flow. The total effective porosity ϕ_{eh} was then calculated merging the identified cells contributing to the flow in i direction.

The connected porosity (ϕ_c), i.e. the fraction of pore space actually connected, is also obtainable from the hydrodynamic simulation. In fact, the isolated pore space is not affected by the imposed pressure difference and remains at the initial pressure condition ($p = p_i$), giving:

$$\phi_c = \phi - \frac{N_{pi}}{N_l} \quad \text{where} \quad i = x, y, z \tag{4.148}$$

where N_{pi} is the number of porous grid cells with $p = p_i$ and N_l is the total number of grid cells. The connected porosity ϕ_c represents a first estimate of the pore fraction that can be potentially involved in the fluid flow. By definition, $\phi_e \leq \phi_c$.

The permeability $k_{h,i}$ is directly calculated by inverting the Darcy's equation [173]:

$$k_{h,i} = \frac{u_i \, \mu}{\nabla_i p} \quad \text{where} \quad i = x, y, z \tag{4.149}$$

where $\nabla_i p$ is the macroscopic pressure gradient across the sample in the i direction and u_i is the component of the Darcy's velocity in the i direction. The pressure gradient is calculated as

$$\nabla_i p = \frac{p_{in} - p_{out}}{L_i}, \tag{4.150}$$

where p_{in} and p_{out} are constant pressures at the inlet and outlet and L_i is the sample length in the i-direction. The Darcy's velocity is calculated as

$$U_{D,i} = \frac{1}{V} \int_V u_i(x, y, z) \, dV, \tag{4.151}$$

with V the volume of the sample and $v_i(x, y, z)$ the local velocity field of the fluid in the i-direction.

Chapter 5

Characterization of 2D images of rocks

The purpose of this Chapter is to show the application of the methodology based on the geometrical and hydrodynamic characterization described in Chapters 3 and 4 to 2D binary images of rocks. The results obtained with these two different procedures are discussed and compared. The case studies and the results reported in this Chapter were published in Viberti *et al.* [73].

In 2D geometries, the inlet and outlet points are placed in the pore space on the inlet and outlet boundaries of the image. These are the points where the fluid enters and leaves the porous medium. Therefore, the application of A* algorithm to the images gives a set of $n_{in} \times n_{out}$ geometrical paths in the considered direction.

In the hydrodynamic approach, numerical simulation of single-phase fluid flow in the pore space using the LBM was used to obtain the fluid paths. The implementation adopted for single-phase flow simulation in porous media is based on the BGK model. The relaxation time was set equal to 1 and the time step was calculated in accordingly to guarantee stability conditions [98]. The nine-velocity square lattice model D2Q9 [150] was adopted to discretize the domain. At the fluid-solid interface, no-slip condition was imposed by the halfway bounce-back method. Constant pressure boundary conditions, which were implemented by the non-equilibrium bounce-back method [162], were applied at the inlet and outlet boundaries. No-flow boundaries parallel to the main flow direction were assumed to reproduce laboratory conditions and they were implemented using the halfway bounce-back method. Furthermore, in order to facilitate the application of boundary conditions, additional cells were added to the inlet and outlet lines.

5.1 Validation cases

In order to validate the two approaches, three simple cases were analyzed: a thin curved channel (Case 1), a thick curved channel (Case 2) and a slanted straight channel, inclined of 23° (Case 3); details are given in Table 5.1.

Table 5.1: Validation cases. Note that in this table τ refers to tortuosity and not to relaxation time [73].

	Image dimensions (px × px)	Resolution (ppcm)	ϕ_{2D} (-)	τ_{an} (-)	r (mm)
Case 1	793 × 623	4170	0.061	1.571	0.030
Case 2	745 × 736	3920	0.360	1.512	0.223
Case 3	491 × 298	2650	0.206	1.086	0.108

In these cases, the hydraulic radius is equal to the capillary tube radius, the effective porosity is equal to the porosity and the tortuosity is the length of the tube median line divided by the extension in the x direction. The input parameters of the three cases are reported in Table 5.2. The fluid used for hydrodynamic simulations has the following properties: viscosity 0.5 cP, density 1050 kg/m^3. A pressure gradient of 100 Pa/m was applied between inlet and outlet. Laminar flow occurs in all the three cases (Re $\leq$ 2). The identified geometrical and hydrodynamic paths are compared in Fig. 5.1. Results are summarized in Table 5.3.

Table 5.2: Parameters for the numerical simulation of validation cases [73].

	n_x (l.u.)	n_y (l.u.)	Δx (μm/l.u)	Re (-)
Case 1	793	623	2.4	0.0046
Case 2	745	736	2.55	1.97
Case 3	491	298	3.77	0.3443

The pore radius estimated with the geometrical approach $\tilde{r}_p$ is in good agreement with the hydraulic radius $r_{H,2D}$, which matches the channel radius. τ_g and τ_h are similar to the theoretical values τ and they give an excellent estimate of tortuosity in Case 3. In the presence of curves (i.e. Case 1 and Case 2), τ_g is smaller than τ_h because the shortest path is a slanted line crossing out the curve, while the hydrodynamic path follows the tube curvature. The discrepancy is more significant when the pore radius is larger (Case 2). In Case 1 the hydrodynamic path follows the channel median line, while in Case 2 the hydraulic path does not perfectly follow the channel median line and, as a consequence, in Case 2 the computed hydraulic tortuosity differs a little from the analytic value. As expected, ϕ_{eg} matches the total porosity. ϕ_{eh} is slightly lower, due to the combination of no-slip effect at the solid-fluid interface, numerical discretization and velocity field processing.

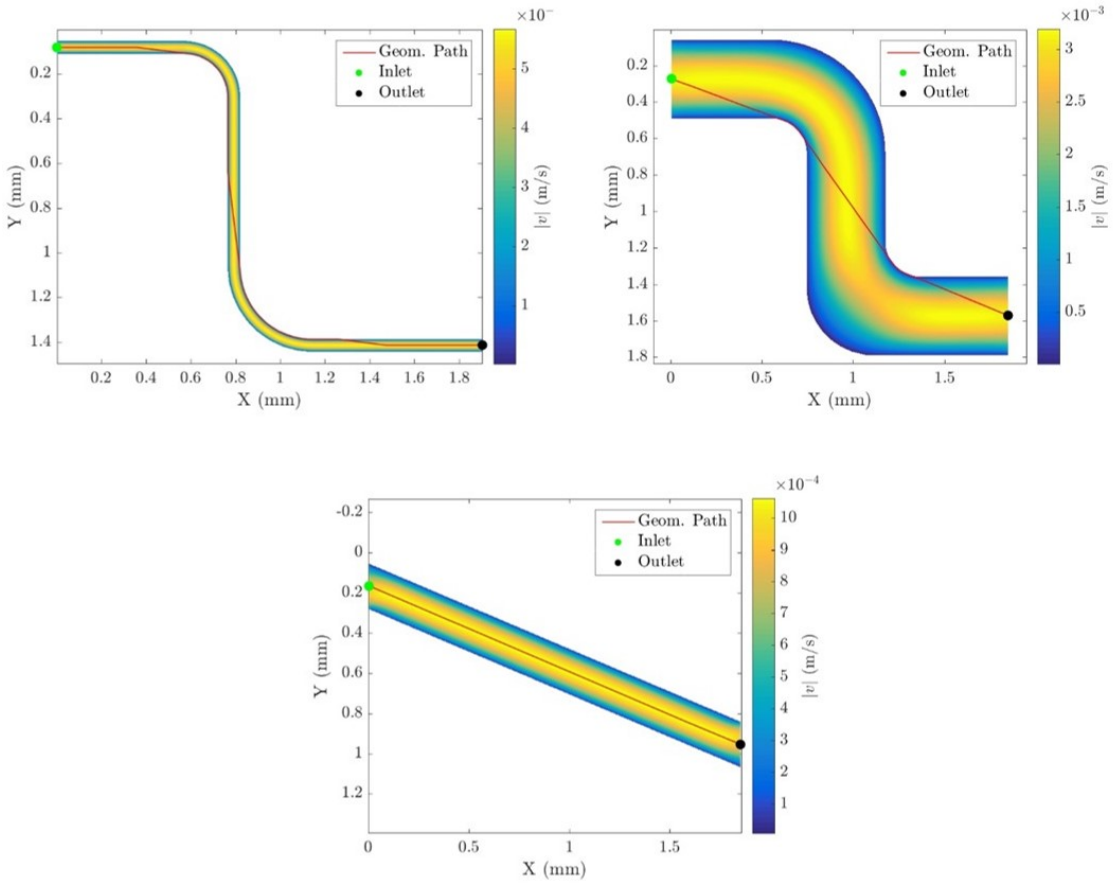

Figure 5.1: Simulated velocity map and detected geometrical paths for the validation cases: (a) Case 1, (b) Case 2, (c) Case 3 [73].

Table 5.3: Comparison of parameter estimates obtained by the geometrical and hydrodynamic approaches for the validation cases [73].

	$r_{H,2D}$ (mm)	$\tilde{r}_p$ (mm)	τ_g (-)	τ_h(-)	ϕ_{eg} (-)	ϕ_{eh} (-)
Case 1	0.030	0.029	1.530	1.571	0.061	0.057
Case 2	0.231	0.221	1.268	1.486	0.359	0.353
Case 3	0.110	0.115	1.087	1.083	0.206	0.198

5.2 Case studies

The geometrical and hydrodynamic characterization was carried out on images obtained from thin sections of 3D samples of sedimentary rocks. In this study, two medium-to-fine-grained sandstone and a oolite were analyzed: Berea sand (D_{50} = 23 μm [174]), Hostun sand (D_{50} = 300 μm [175]) and Caicos ooid (D_{50} = 420 μm [176]). All these images were taken from the literature. When available, multiple

images of the same rock were studied. The images are represented in Fig. 5.2 and the details are reported in Table 5.4.

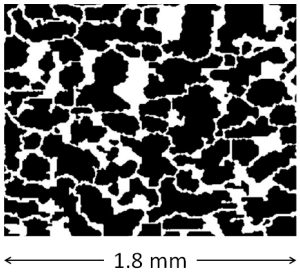

(a) BE30

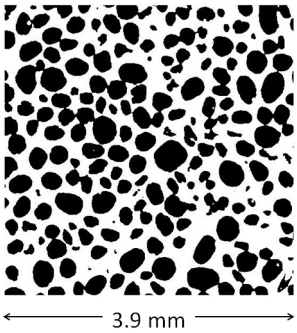

(b) CA52

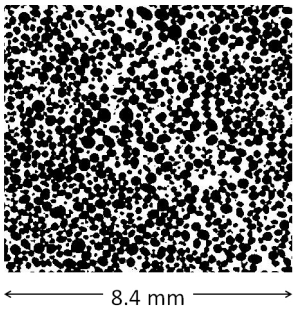

(c) CA42

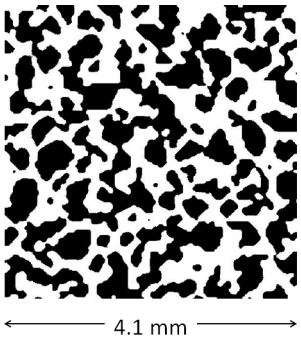

(d) HO49

(e) HO56

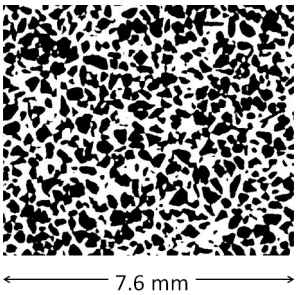

(f) HO47

Figure 5.2: Case studies: 2D images of sedimentary rocks [73].

These three rocks have very different pore geometries. Berea sand is characterized by a high difference in pore dimensions. Hostun sand is more homogeneous and it is characterized by well-sorted predominantly quartz angular grains [177]. Caicos ooid is relatively homogeneous and characterized by round calcite grains [176]. The high porosity and permeability values of these rocks make them a potential source of hydrocarbons. Also, they are used as standard rocks for various applications such

Table 5.4: Case studies: images details [73].

	Image dimensions (px × px)	Resolution (ppcm)	ϕ_{2D} (-)
BE30	769 × 624	4120	0.3
HO49	640 × 640	1450	0.49
HO56	449 × 549	1915	0.56
HO47	657 × 654	858	0.47
CA52	546 × 549	1414	0.52
CA42	448 × 417	531	0.42

as laboratory core analysis, flooding experiment, testing the efficiency of chemical surfactants and studying the drainage capacity in granular soil [178–180].

For Berea sand, a black and white image of a horizontal sample [129] widely used in literature (for example in Gu *et al.* [181] and Xu & Liu [121]) was adopted; the image is shown in Fig. 5.2a and named in the following as case BE30. For Hostun sand, X-ray micro-tomography images of horizontal sections of three different samples were considered: a section with $\phi_{2D} = 49\%$ [182], named case HO49; a small horizontal section with $\phi_{2D} = 56\%$ [183], named case HO56; a more extended section with $\phi_{2D} = 47\%$ [183], named case HO47. For Caicos ooid, X-ray micro-tomography of two samples were available: a small horizontal section [183], named CA52, and a more extended vertical section, already segmented [176], named CA42. The gray-scale X-ray micro-tomography images were segmented in order to distinguish the solid part from the voids for the following geometrical analysis and hydrodynamic simulation: 1 was assigned to the solid grain while 0 to the porous domain. To this end, a threshold was applied to the gray-scale images based on the histogram of pixels values [183]. The obtained binary images are shown in Fig. 5.2b-5.2f and the corresponding image parameters are reported in Table 5.4, where the 2D porosity values were calculated from images.

In order to observe hydrodynamic behavior, the smallest pore size should be 4-5 lattice units [105]. When the pixel resolution of the rock images did not satisfy the condition above, the figures were resized by bi-cubic interpolation [86], imposing a number of lattices that guarantees a minimum of 5 lattice cells in the smallest pore throats. The numerical parameters of the case studies are reported in Table 5.5. The fluid used for numerical simulations has the following properties: viscosity 0.5 cP, density 1050 kg/m^3. The pressure gradient between inlet and outlet is 100 Pa/m. Laminar flow occurs in all the three cases. The case studies were analyzed separately in the x and y directions to assess eventual discrepancy in tortuosity which could be an indicator of permeability anisotropy.

Table 5.5: Numerical simulation parameters [73].

	n_x (l.u.)	n_y (l.u.)	Δx (μm/l.u.)	Re (-)
BE30	1706	1367	1.04	3.18E-04
HO49	1200	1200	3.45	0.054
HO56	1000	1209	2.5	0.0192
HO47	1200	1038	6.66	0.0281
CA52	800	804	5	0.0526
CA42	1200	1121	7.5	0.006

5.3 Results and discussion

Results of the geometrical analysis and hydrodynamic simulation are summarized in Table 5.6. Moreover, the mode of the pore radius r_p estimated through the path finding approach is compared with the calculated hydraulic radius ($r_{H,2D}$). In CA42 there is no connectivity along the x direction, thus it was not possible to estimate τ_x.

Table 5.6: Comparison of parameter estimates obtained by the geometrical and hydrodynamic approaches [73].

	$r_{H,2D}$ (μm)	$\tilde{r}_p$ (μm)	τ_{xg} (-)	τ_{xh} (-)	τ_{yg} (-)	τ_{yh} (-)	ϕ_{eg} (-)	ϕ_{eh} (-)	ϕ_{ch} (-)
BE30	14.6	7.29	1.250	1.416	1.437	1.542	0.277	0.256	0.3
HO49	71.7	58.6	1.269	1.459	1.243	1.357	0.374	0.362	0.481
HO56	52.6	57.5	1.153	1.322	1.14	1.362	0.533	0.506	0.559
HO47	69.5	47.2	1.257	1.641	1.22	1.6	0.342	0.355	0.459
CA52	61.4	38.9	1.128	1.301	1.118	1.278	0.508	0.489	0.519
CA42	78.8	95.4	-	-	1.317	1.65	0.065	0.056	0.31

In Figs. 5.3 and 5.4, the results for BE30 and HO49 are represented. In Fig. 5.5, it is shown the comparison of the effective porosity map obtained with the two approaches. In Fig. 5.6, the pore radius analysis conducted with the geometrical approach (i.e. overall pore radius distribution and pore radius evolution along a single path) is shown.

In all cases, tortuosity values calculated with the two methods are comparable (the discrepancy is less than 10%) and the geometrical tortuosity is slightly smaller than the hydraulic tortuosity, as expected [54, 56]. The only exception is HO47, which shows a discrepancy of around 16%; this is due to local significant narrowing of the pore radius along the shortest paths which induces the fluid flow to choose alternative ways even if longer. Comparing these results with the literature, tortuosity results of Berea are coherent with the gamma-shaped distribution with minimum value 1.07 and most probable value near to 2, reported in Lindquist *et al.* [37] and just below the range 1.6-2.8 reported in Takahashi *et al.* [184].

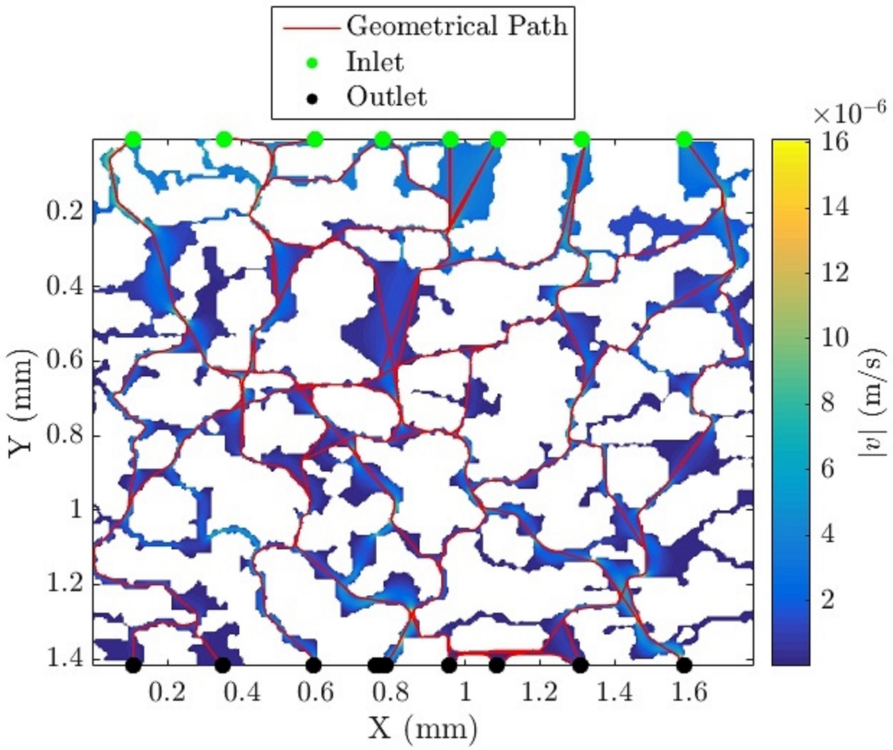

Figure 5.3: Simulated velocity map and detected geometrical paths on Berea sandstone considering flow in the y direction [73].

The pore radius distribution obtained by the path-finding algorithm appears to be reliable. For instance, in Berea the distribution is in good agreement with the literature (Fig. 5.6a): 31% of pore throats diameter about 10 μm [83]; 5 μm as the most frequent pore throat radius [84]; 37% of relative pore volume characterized by 7-10 μm of pore radius [185]. In Hostun, results are comparable with the pore diameter distribution calculated with Mercury Intrusion Porosity and analysis of SEM images [175], which show a mode around 60-90 μm. Reasonable agreement is observed between the hydraulic radius and the mode of pore radius distribution obtained by the geometrical approach in all cases (Tab. 5.6), thus suggesting that the hydraulic radius is reasonably representative of the effective pore radius of the sample, at least if the pore radius variations are limited. The representativeness of $r_{H,2D}$ is poorer when the pore radii is highly variable (e.g. BE30, HO47, CA42).

In all cases except CA42, the connected porosity is similar to the total porosity ($\phi_{c,h} \approx \phi_{2D}$). In fact, CA42 shows a very poor connection as shown in Fig. 5.5. Good agreement is observed in terms of estimated effective porosity in all scenarios (Tab. 5.6). Pore space in small sections (CA57 and HO56), characterized by higher porosities, is more interested by fluid flow (i.e. $\phi - \phi_e < 10\%$). Conversely, in HO49, HO47 and CA42 significant dead zones ($\phi - \phi_e \approx 30\%$ or greater) are

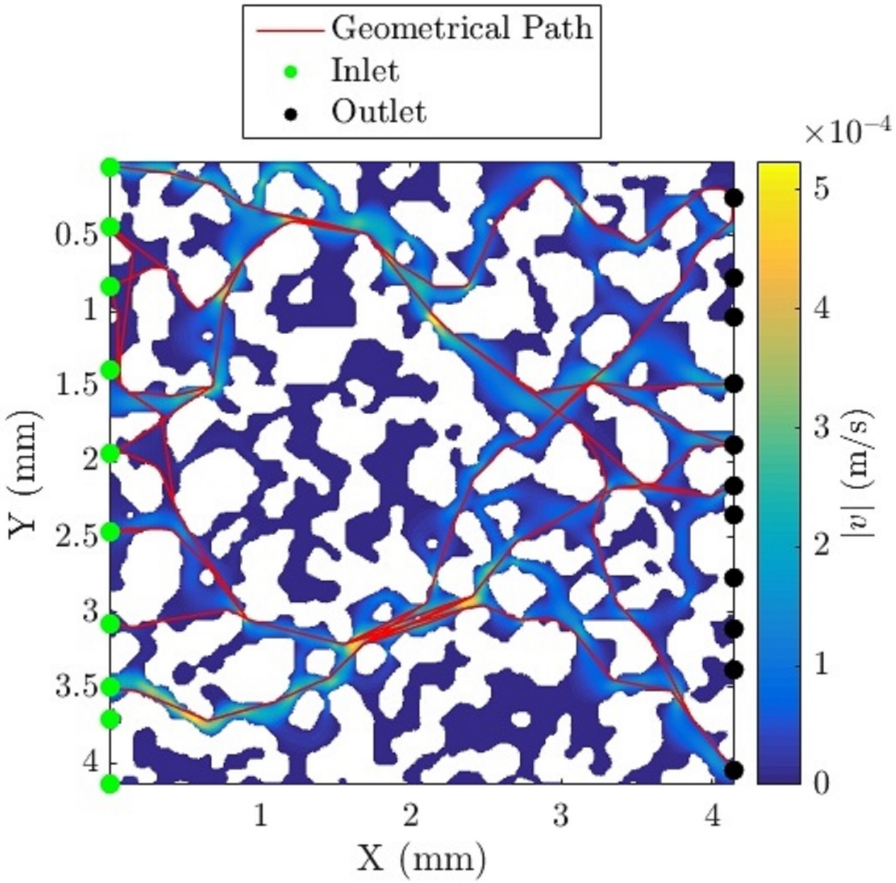

Figure 5.4: Simulated velocity map and detected geometrical paths on Hostun sandstone considering flow in the x direction [73].

clearly identified by both approaches. Discrepancies between effective porosity estimated with the two approaches is below 5% in most cases. These differences are due to different treatments of meandering pore space zones by the two methods. Trajectories identified by the A* algorithm agree with the paths shown by the velocity map in HO49, H56, CA52 and CA42, and, as consequence, the identified dead zones are well comparable. On the contrary, in BE30 and HO47, the more complex pore structure, characterized by multiple possible paths between the entry and outlet points, and the higher variability in the pore radius induce local discrepancies between the geometrical and hydrodynamic path. The fluid flow, in presence of a conspicuous narrowing of the pore radius, choose to follow a wider pathway.

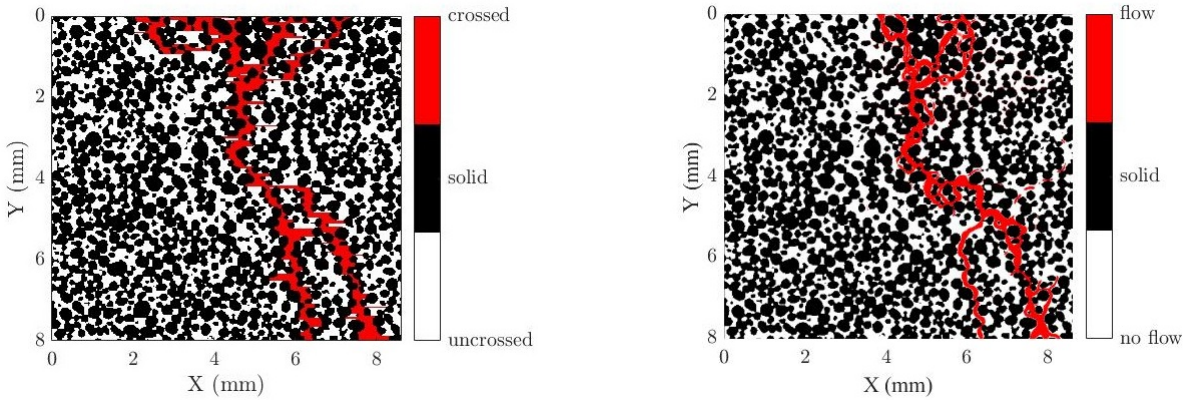

(a) geometric (b) hydraulic

Figure 5.5: Pore volume interested by fluid flow (red) and dead zones (white) on Caicos ooid CA42, identified by applying (a) the path-finding algorithm and (b) a threshold on the velocity simulated by the LBM [73].

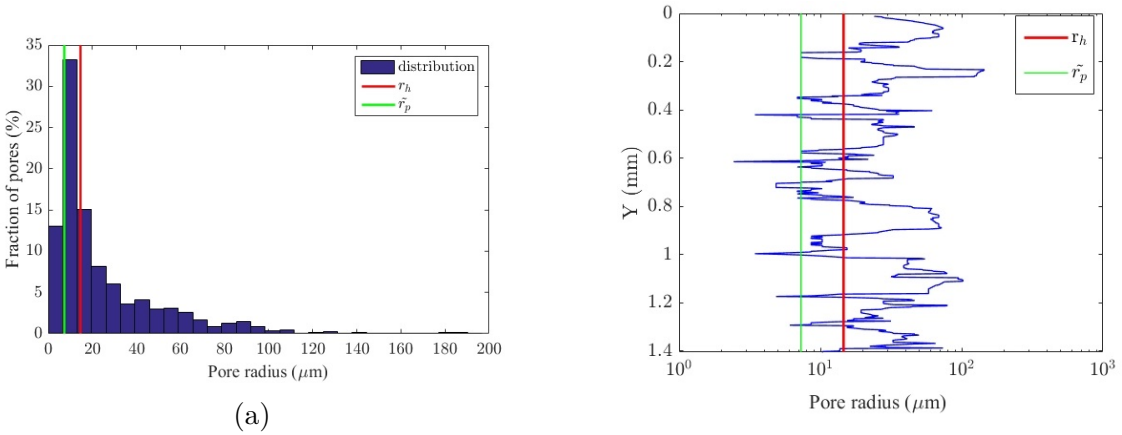

(a) (b)

Figure 5.6: Estimate of the pore size of Berea sandstone: (a) pore radius distribution compared with the hydraulic radius (red line) ; (b) pore radius variation along a single geometrical path, compared with the mode of the pore radius along the selected path (green line) and the hydraulic radius (red line) [73].

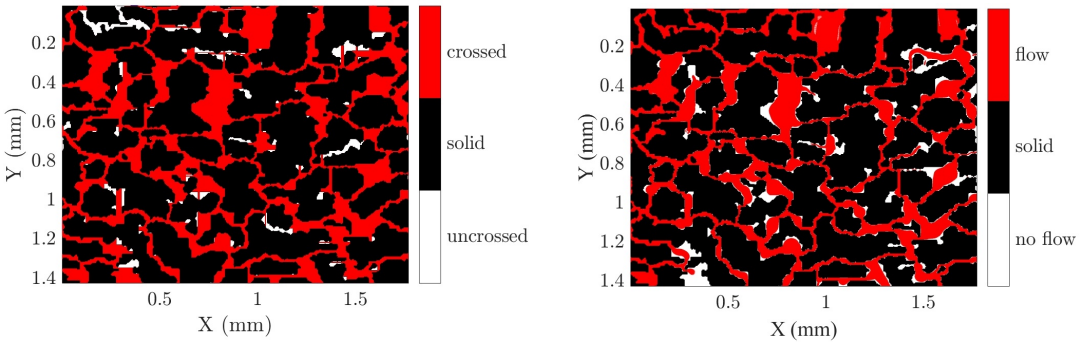

(a) geometric (b) hydraulic

Figure 5.7: Pore volume interested by fluid flow (red) and dead zones (white) on Berea sandstone, identified by applying (a) the path-finding algorithm and (b) a threshold on the velocity simulated by the LBM [73].

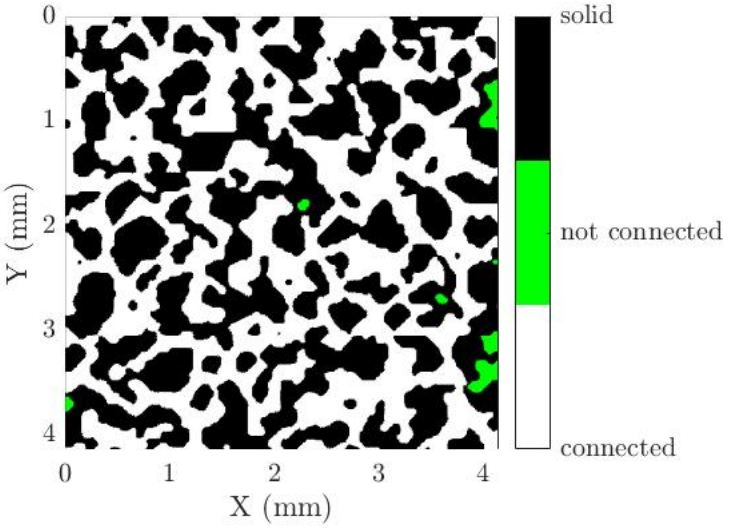

Figure 5.8: Representation of the connected porosity in HO49 [73].

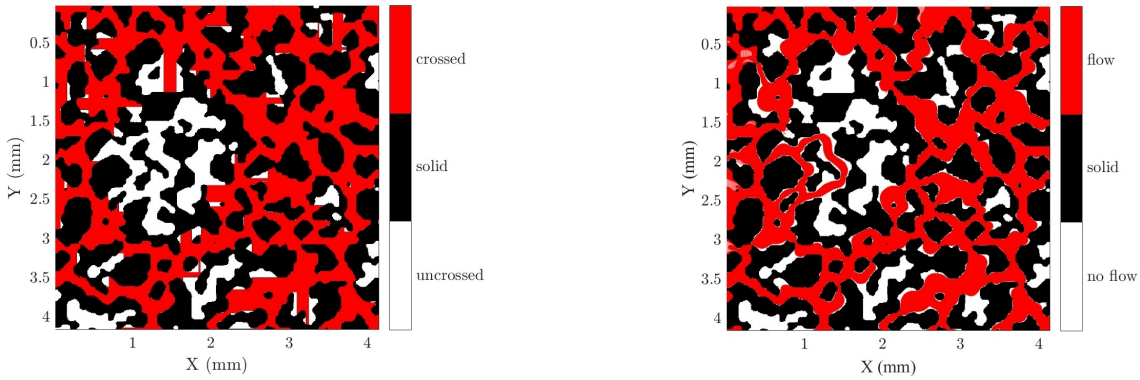

(a) geometric (b) hydraulic

Figure 5.9: Pore volume interested by fluid flow (red) and dead zones (white) on Hostun HO47 sandstone, identified by applying (a) the path-finding algorithm and (b) a threshold on the velocity simulated by the LBM [73].

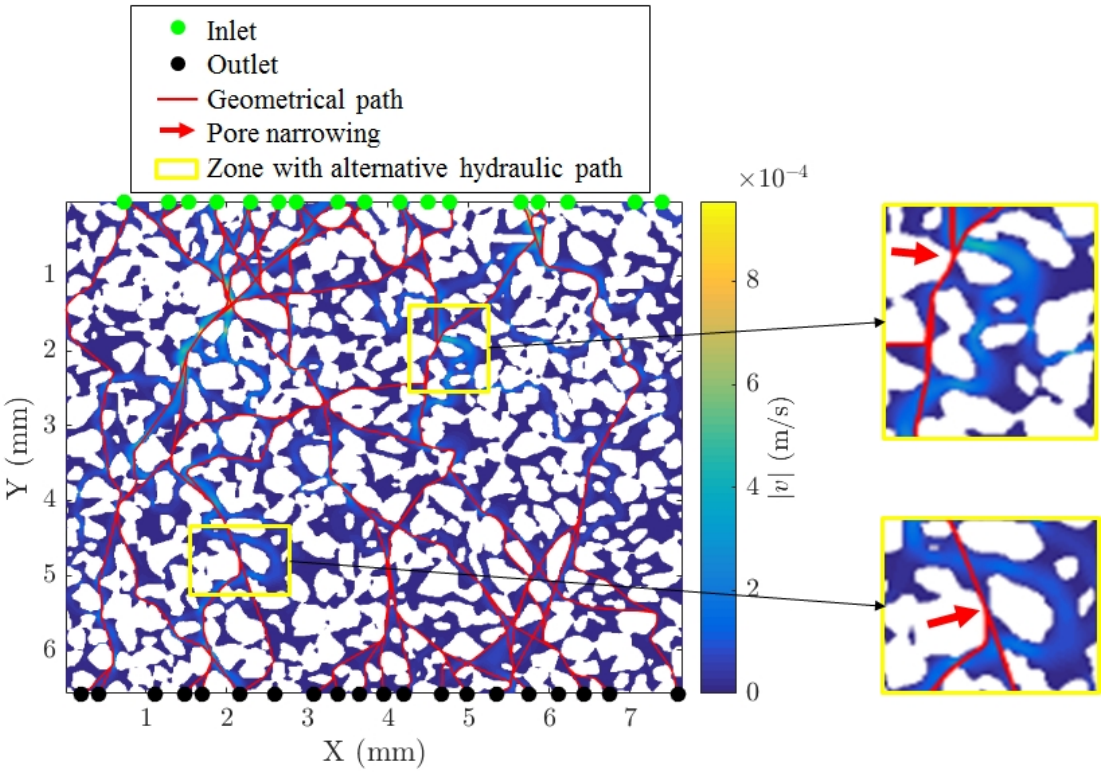

Figure 5.10: Velocity map obtained by LBM simulation and geometrical paths in HO47 in y direction. Pore narrowing forces a change of the fluid path. on the other hand, the shortest path is highlighted by red arrows and yellow circles [73].

Chapter 6

Characterization of 3D images of rocks

In this Chapter, the methodology presented in Chapters 3 and 4 and applied to 2D binary images or rocks Chapter 5 is extended to 3D binary images of porous media. Since 3D images data of real rocks were not available, synthetic 3D binary samples were generated through the random porous media generation algorithm Quartet Structure Generation Set (QSGS) [186]. For 3D images, the analysis was also extended to the estimate of permeability k and anisotropy R. Anisotropy can be quantified by [187]:

$$\mathrm{R} = \frac{k_{min}}{\sqrt{k_{int}\, k_{max}}}, \tag{6.1}$$

where k_{min} is the minimum permeability, k_{int} is the intermediate permeability and k_{max} is the maximum permeability value.

For the geometrical characterization, the A* algorithm is used to obtain the shortest paths between pairs of inlet and outlet points.

For the hydrodynamic characterization, single-phase fluid flow was simulated by CFD modeling at low Reynolds numbers (i.e. Re ≤ 2) to obtain the hydrodynamic paths in the pore space. The CFD code OpenFOAM, based on the Finite Volume Method (FVM), was used to perform simulations. The Navier-Stokes equations (NSEs) govern the incompressible single-phase flow at small Reynolds numbers. The NSEs are solved for steady-state conditions by the Semi-Implicit Method for Pressure Linked Equations (SIMPLE) algorithm [135].

The case studies and the results reported in this Chapter were published in Salina Borello *et al.* [75].

6.1 Generation of 3D synthetic rock images

The QSGS is an algorithm to generate 3D porous media based on the stochastic cluster growth theory [186]. The QSGS generates realistic microstructures of porous media such as rocks [188–190] and soils [191] with a few control parameters. Three control parameters must be set for generating a porous medium saturated by a single fluid: porosity (ϕ), core distribution probability (P) and a set of growth probabilities (D_i). The core distribution probability is the probability of a grid cell center to become the core of a grain and it determines the degree of detail of a structure. In fact, bigger P leads to more smaller grains. The growth probability D_i is the probability of the grain to grow in the i-direction. The set of growth probabilities regulates the anisotropy. In 3D, 26 directions (6 main, 12 side, and 8 diagonal) are considered. The scheme of growth directions adopted in this work is shown in Fig. 6.1, where main directions (from D_1 to D_6) are represented in green, side directions (from D_7 to D_{18}) in red and diagonal directions (from D_{19} to D_{26}) in blue.

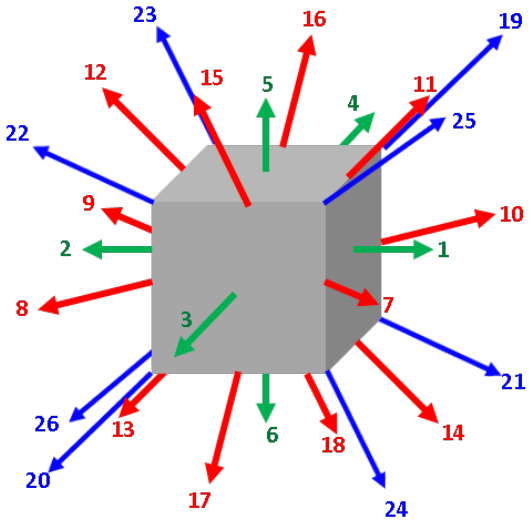

Figure 6.1: Scheme of growth directions for the QSGS algorithm [75].

Isotropic systems are obtained by setting uniform values within each class of direction [186]. The values used in this work are:

$$\begin{aligned} D_1, \ldots, D_6 &= D_1, \\ D_7, \ldots, D_{18} &= \frac{1}{12} D_1, \\ D_{19}, \ldots, D_{26} &= \frac{1}{8} D_7. \end{aligned} \tag{6.2}$$

In order to introduce anisotropy in the vertical (z) direction, horizontal and vertical growth probabilities are connected to an aspect ratio $AR = D_z/D_{xy}$

$$\begin{aligned} &D_1, \ldots, D_4 = D_1, \\ &D_5, \ldots, D_6 = AR\, D_1, \quad AR < 1, \\ &D_7, \ldots, D_{10} = \frac{1}{12} D_1, \\ &D_{11}, \ldots, D_{18} = \frac{\sqrt{AR}}{12} D_1, \\ &D_{19}, \ldots, D_{26} = \frac{\sqrt[3]{AR}}{96} D_1. \end{aligned} \tag{6.3}$$

In terms of permeability, the resulting relationship between anisotropy, and growth probability aspect ratio AR is nonlinear. A similar behavior can be recognized from the data provided by Wang *et al.* [192].

In the QSGS algorithm there are two main steps [190]:

1) Grain cores are randomly distributed on the grid in according to$P$:
   (a) a random number n_g is assigned to each grid cell;
   (b) cells having $n_g < P$ become grain cores.
2) Iterative enlargement of existing solid grains in according to D_i, until the desired value of porosity ϕ reaches the desired value ϕ:
   (a) new random numbers n_{gi} are assigned to all neighbor cells of the grain.
   (b) the neighbor cells in the i-direction will belong to the grain if $n_{gi} < D_i$.

Since the generation procedure is random, the same set of control parameters will produce different geometries having same morphological features. Recently, some authors proposed a modified versions of the QSGS algorithm to take into account multiscale pore size distributions [192, 193]. Wang *et al.* [192] used a combination of a coarse and a refined structure obtained by two independent simultaneous construction processes, characterized by two different core distribution probabilities (P_{coarse} and $P_{refined}$). In this work, a modification of the two-scale generation method suggested by Wang *et al.* [192] was adopted to generate anisotropic porous media. In this implementation, coarse and refined structures are constructed in sequence. Once the coarse grain structure G_1 is fully grown to a target porosity (ϕ_{coarse}), the refined grain structure G_2 grows independently until the combination of the two structures (G_3) reaches the target porosity ϕ. G_3 is obtained by the union of the coarse and refined structures, with possible local permeation. Details about the QSGS algorithm modified in order to consider multiple grain size distributions is shown in Fig. 6.2. In the obtained geometry there may be some dead-end

or isolated pores not connected to the main pore space. In order to generate 3D porous media with the QSGS algorithm, the open-source code GenPorMed [194] was used and then modified and integrated to include multiple grain distributions and anisotropy.

It should be noted that the QSGS algorithm gives a simplified representation of rock complexity. In fact, it assumes stationarity over the domain of interest, therefore it is not able to reproduce heterogeneity. Also, unlike fractal approaches, it ignores the scale-invariance properties widely existing in porous media [195]. However, it is a comprehensive algorithm to characterize the original complexity in natural porous media, such as the random internal morphology and anisotropic properties [195].

6.2 Case studies

Two different cases were considered: an isotropic porous medium with porosity equal to 30% (Case 1) and an anisotropic porous medium having a porosity of 20% and smaller grain sizes (Case 2). Case 1 was generated with the QSGS algorithm, while case 2 was generated with the modified version of the QSGS algorithm considering two-scale grain size. The QSGS parameters are listed in Tab. 6.1 and the generated samples are binary matrices having $100 \times 100 \times 100$ voxels. The samples have an edge length equal to 0.7 mm. The 3D images and 2D sections for Case 1 and Case 2 are shown in Fig. 6.3.

Table 6.1: Cases generated with the QSGS algorithm [75].

	Case 1	**Case 2**
P (-)	0.001	P_{coarse}=0.001; $P_{refined}$=0.0001
$D_{x,y}$ (-)	0.001	0.001
D_z (-)	0.001	1×10^{-9}
ϕ (%)	30	ϕ_{coarse}=50; ϕ=20
r_H (μm)	4.25	5.03
Resolution (ppcm)	142.9	142.9

For the geometrical characterization, a set of inlet and outlet points were positioned on the boundary faces of the domain orthogonal to the flow directions x, y and z. In this case, inlet and outlet points were set by the user. However, since in some cases the manual selection of inlet and outlet points might be time consuming, a procedure for the automatic selection these points was implemented and described in Appendix A.

The mesh for the CFD simulations was created by using the native OpenFOAM mesh generator *snappyHexMesh*. In order to use *snappyHexMesh*, the 3D binary

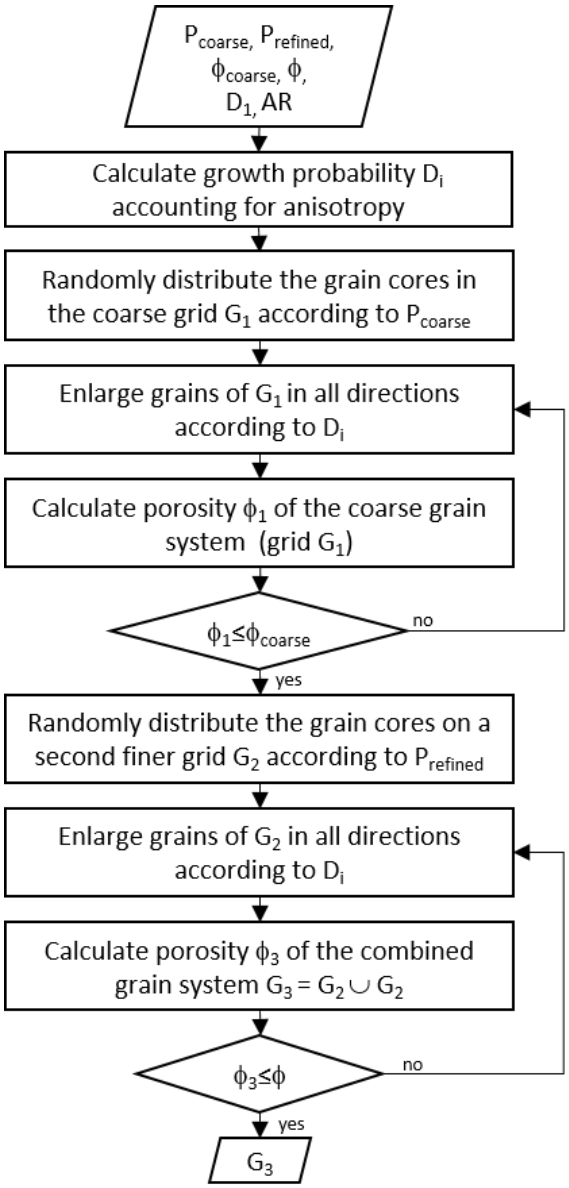

Figure 6.2: QSGS algorithm with two grain-size distributions [75].

image obtained with the QSGS was converted into a stl file using the Matlab library written by Aitkenhead [196].

For each case study, three simulations were run to assess the textural parameters in each direction $i = x, y, z$. For each investigated direction i, the flow is forced toward i direction by imposing a macroscopic pressure gradient $\nabla_i p$ along the i direction. To this end, constant pressure at the inlet (p_{in}) and at the outlet (p_{out}) boundaries were imposed. No flow and no-slip boundary conditions were imposed on the remaining external surfaces and at the fluid-solid interface. In the CFD

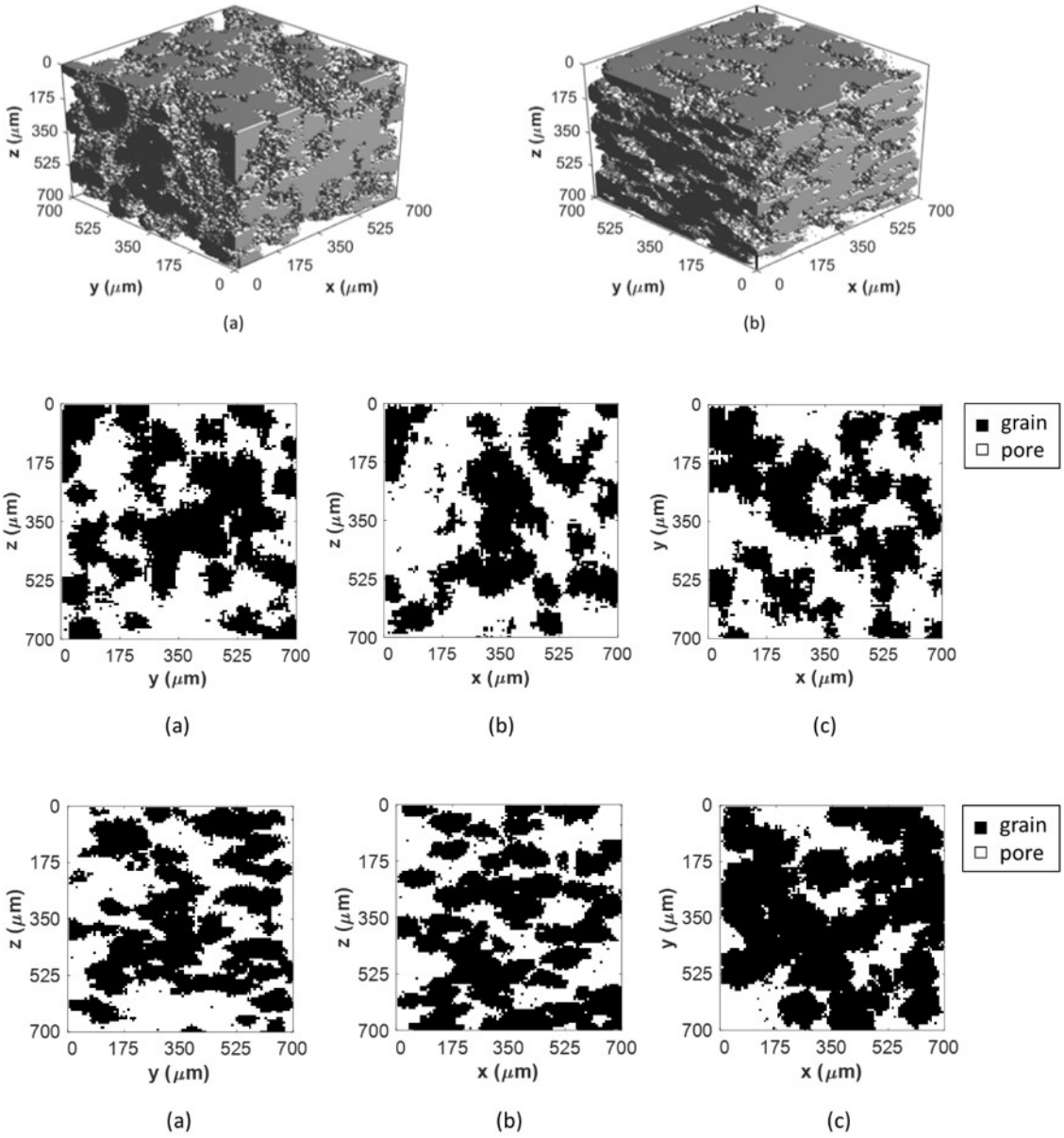

Figure 6.3: 3D images of the cases generated with the QSGS algorithm: (a) isotropic (Case 1) and anisotropic (Case 2). 2D top sections of Case 2 in x, y and z directions [75].

simulations, the mesh was refined to guarantee at least 3-4 cells in the smallest pores. In order to choose the correct mesh resolution, a mesh sensitivity was conducted on Case 1 and in the x flow direction. In all the simulations, the grid is structured and the cell is square, i.e. $\Delta x = \Delta y = \Delta z$. Four different increasing mesh resolution are considered and named refinement level: level 1 corresponds to

the lowest resolution and level 4 to highest resolution. The accuracy is evaluated by calculating the following relative error on permeability [173]:

$$E(k) = \frac{|k_x^4 - k_x^j|}{k_x^4}, \tag{6.4}$$

where j = 1,2,3 is the refinement level up to 3 and k_x^4 is the permeability calculated with the refinement level 4, that has $\Delta x = 2$ μm. Also, the same relative error was calculated for tortuosity ($E(\tau_h)$) and effective porosity ($E(\phi_e)$). Using the refinement level 4, the results are: $k = 900$ mD, $\tau_h = 1.653$ and $\phi_e = 16.84$. In Table 6.2, the relative errors related to the refinement levels are showed.

Table 6.2: Relative errors for three different refinement levels.

Refinement	Δx (μm)	$E(k)$	$E(\tau_h)$	$E(\phi_e)$
Level 1	3.5	15%	0.96%	2.55%
Level 2	2.8	8%	0.78%	2.43%
Level 3	2.3	2.3%	0.27%	0.35%

Increasing the refinement level, the relative error in permeability decreases from 15% to 2.3%, suggesting that the numerical error in permeability calculation is related to the number of cell discretizing the smallest pores [173]. Hydrodynamic tortuosity and effective porosity are much less sensible to grid refinement than permeability. Therefore, when the main task is to calculate τ_h or ϕ_e, a high level of refinement is not required to obtain an accurate result. However, in this study we are interested in calculating permeability with good accuracy and therefore the refinement level 4 was chosen.

Finally, in order to verify that the numerical method can be used to characterize the porous medium, it is necessary that the permeability and the other pore structure parameters do not change with the type of fluid injected. Therefore, it was also verified that permeability, tortuosity and effective porosity were invariant with respect the fluid properties in single-phase fluid flow conditions. Three different fluids were considered at reservoir conditions (150 bar, 45 °C): water, methane, and heavy oil. In all the cases, the same pressure gradient between the inlet and the outlet was applied, assuring Reynolds number Re$<<$ 1. Details are given in Table. 6.3. The simulations were run for all the three types of fluids in the three directions and the values of permeability, tortuosity and effective porosity values were found to be almost the same, ensuring the ability of the hydrodynamic approach to characterize correctly the rock properties.

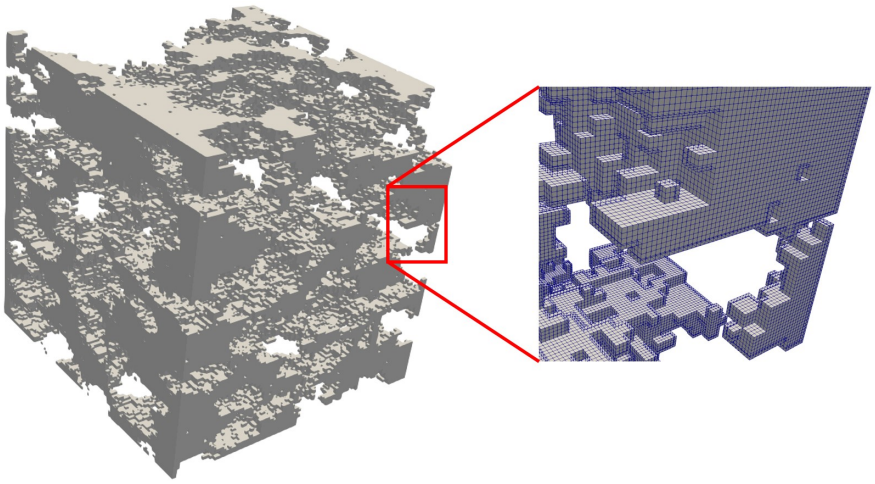

Figure 6.4: Computational mesh for CFD simulation. The pore space of binary images is directly discretized.

Table 6.3: Fluid properties, pressure difference, pressure gradient and Reynolds number adopted for the hydraulic characterization [75].

	water	methane	heavy oil
μ (Pa s)	0.0005	1.60×10^{-5}	0.5
ρ (kg/m^3)	1050	107.5514	1050
Δp (Pa)	0.0708	0.0708	0.0708
Δp/L (Pa/m)	101.1429	101.1429	101.1429
Re	10^{-4}	10^{-2}	10^{-10}

6.3 Results and discussion

In this Section, the main results obtained with the geometrical and hydrodynamic approach are reported, and a comparison between the two methods is proposed. In Fig. 6.5, the pressure field computed with CFD for Case 1 and Case 2 in the z direction are represented. This picture shows a clear and uniform pressure gradient over the all domain in Case 1, and a disconnected and sharp pressure gradient in Case 2, where in only a few small regions of the domain a transition is visible. This is a first qualitative indication of low connectivity in z flow direction in Case 2, because the fluid is forced to flow into a few connected channels and a large part of the domain is not connected.

In Figures 6.6 and 6.7, the main flow paths identified by the geometrical and the hydrodynamic approaches are shown. On the top, the blue points on the inlet and outlet sections represent the n_{in} and n_{out} sets of points selected as starting and final points for the search and the geometrical paths are represented in red. On the bottom, the hydrodynamic paths individuated through the velocity field map

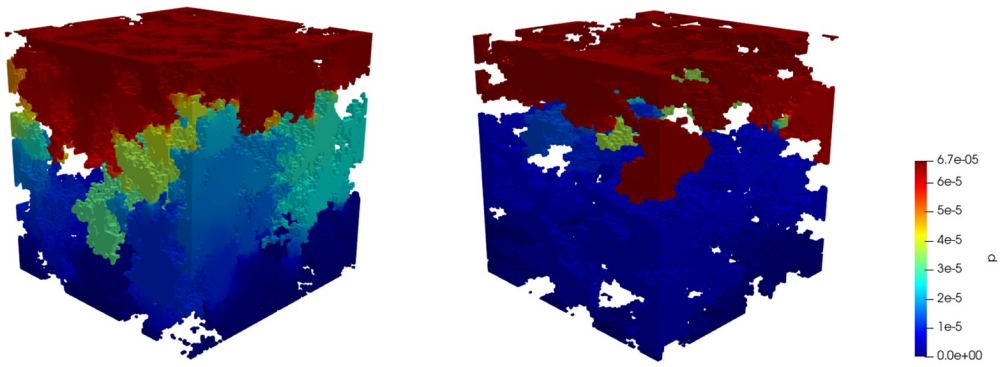

Figure 6.5: Pressure fields for Case 1 (left) and Case 2 (right) in z flow direction. Note that the kinematic pressure ($p_{kin} = p/\rho$) is represented, therefore the physical pressure is obtained mutiplying p_{kin} by the fluid density.

in the three main flow direction are reported. In Case 1, the isotropy of the system is visible both from the geometrical and hydrodynamic paths because there are no favorite flow direction over the others. In Case 2, fewer geometrical and hydraulic paths are found in z direction over x and y directions, suggesting anisotropy in the system. The geometrical and hydrodynamic approach are consistent in the results.

All the numerical results obtained with the geometrical and hydrodynamic approaches are listed in In Table 6.4. The distributions obtained with the geometrical analysis of the pore space for tortuosity, pore radius and constriction factor are compared for Case 1 and Case 2 and are showed in Figs. 6.9, 6.10 and 6.9 respectively. Note that the representative pore radius and the constriction factor cannot be calculated by the hydrodynamic approach.

The values of tortuosity, effective porosity, permeability and anisotropy calculated with the geometrical and hydrodynamic approach are in good agreement both in Case 1 and Case 2. The histograms of constriction values for Case 1 and Case 2 are showed in Fig. 6.10. In Case 1, the histograms confirm the isotropy of the system because have similar shapes and the mode is around the same value; this is confirmed by the numerical values of the mode reported in Table 6.4. In Case 2, the histogram of constriction in z direction is moved to higher values and its mode C_z=222 is significantly larger than C_x=86 and C_y=94. An increase of the constriction factor produces a decrease in permeability and the strong difference in constriction factor is another sign of anisotropy in the sample. Similar considerations can be done regarding the tortuosity distribution.

In the hydrodynamic approach, the fluid flow is intrinsically influenced by all the features of the pore space (i.e. tortuosity, effective porosity, constriction and pore radius) and the porous medium is usually characterized by a single parameter that takes into account all these properties, which is the permeability calculated directly inverting the Darcy's law. Instead, in the geometrical approach all pore

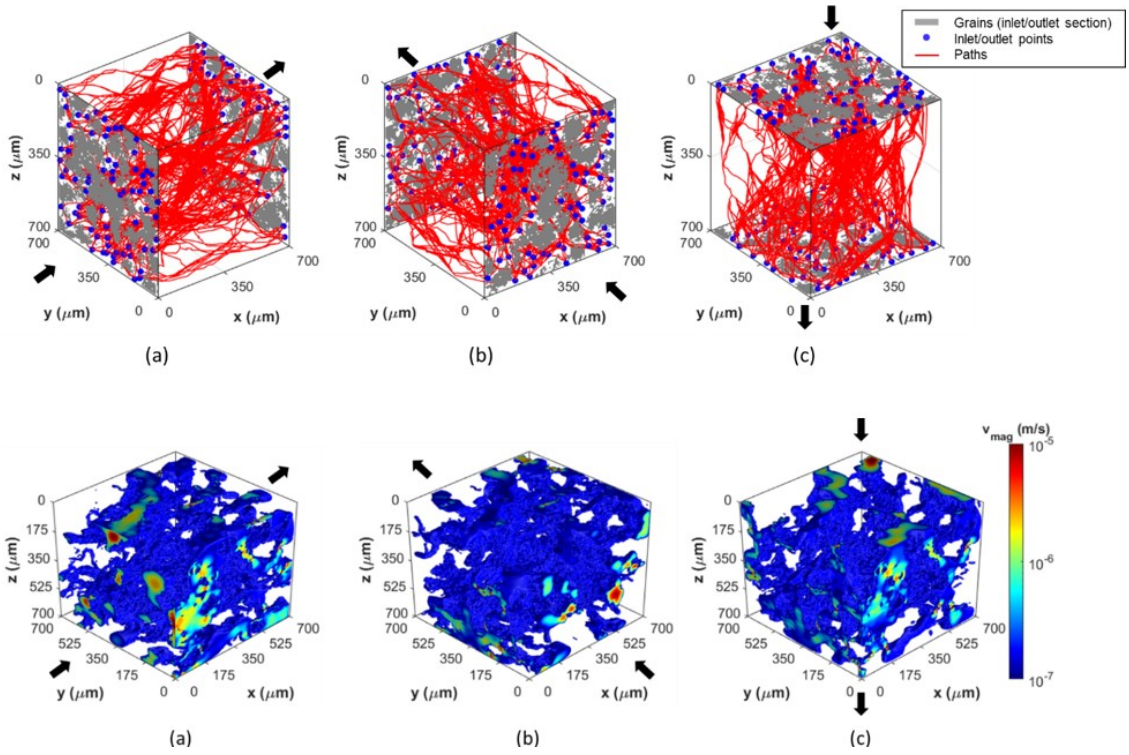

Figure 6.6: Geometrical paths for Case 1, considering flow in the x, y, and z directions. Simulated velocity map for Case 1 in the x, y, and z directions [75].

space characteristics are evaluated individually and combined through the Kozeny-Carman equation. In Case 1, the estimate of permeability values calculated with the geometrical approach and using $c_k = 5.8$ is in good agreement with permeability values obtained with the hydrodynamic approach. In case 2, the Kozeny-Carman coefficient (Section 2.3) $c_k = 20$, obtained by fitting the permeability of the x and y directions with the values of the hydrodynamic simulation, is within the range of 4-40 reported in literature. The values of permeability calculated with the geometrical approach are strongly affected by the selected value of the Kozeny-Carman coefficient c_k, which is difficult to be established a priori for irregular geometries such as anisotropic porous media. The possibility to include information about the constriction factor in c_k should be investigated.

Since the A* algorithm has been implemented in a prototype Matlab code, which is not been optimized and/or parallelized yet, a quantitative comparison in terms of computational time against the CFD code OpenFOAM is not provided. Nevertheless, the computational time of the geometrical approach is lower than CFD single-phase flow simulation: run time reduction of about 5% considering 50×50 inlet and outlet points per direction; run time reduction of about 80% considering 30×30 inlet and outlet points per direction.

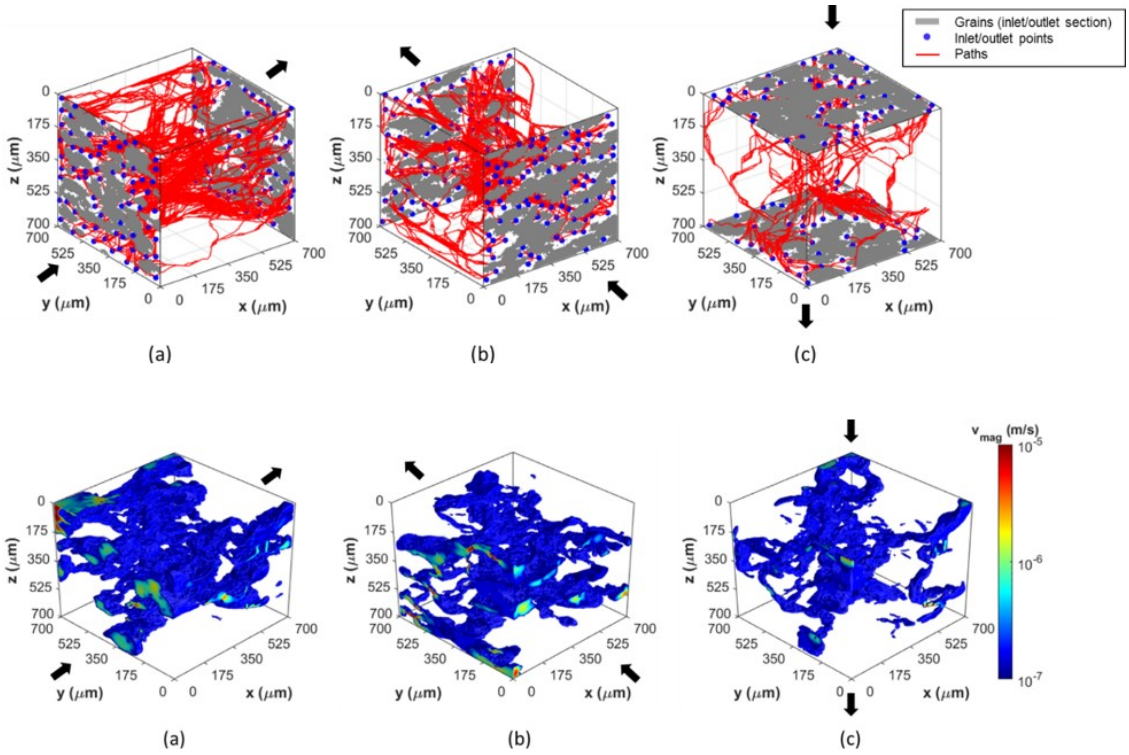

Figure 6.7: Geometrical paths for Case 2, considering flow in the x, y, and z directions. Simulated velocity map for Case 1 in the x, y, and z directions [75].

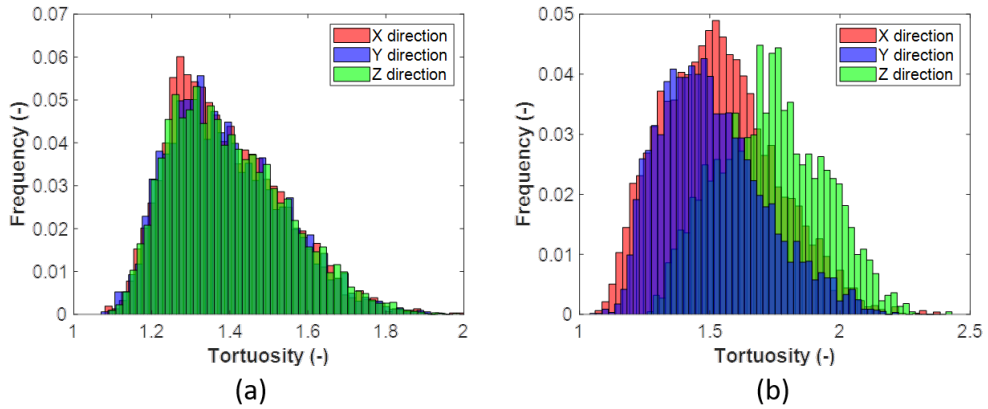

Figure 6.8: Tortuosity distribution: a) Case 1; b) Case 2 [75].

A final consideration is related to the invariance of the hydrodynamic characterization to the chosen fluid. Fluids with very different properties such as water, gas (CH_4), and heavy oil were used for the hydraulic characterization of the anisotropic

Table 6.4: Results obtained with the geometrical and hydrodynamic approaches [75].

		Geometrical	**Hydrodynamic**
Case 1	τ_x (-)	1.35	1.653
	τ_y (-)	1.38	1.660
	τ_z (-)	1.4	1.443
	$\phi_{e,x}$ (-)	16.7	16.84
	$\phi_{e,y}$ (-)	16.9	16.83
	$\phi_{e,z}$ (-)	19.0	17.26
	ϕ_e (-)	24.9	26.32
	r_x (μm)	6.9	-
	r_y (μm)	7.2	-
	r_z (μm)	7.3	-
	C_x (-)	187	-
	C_y (-)	120	-
	C_z (-)	125	-
	k_x (mD)	759	900
	k_y (mD)	807	764
	k_z (mD)	906	839
	R (-)	0.89	0.88
Case 2	τ_x (-)	1.52	1.320
	τ_y (-)	1.48	1.519
	τ_z (-)	1.73	2.068
	$\phi_{e,x}$ (-)	12.4	11.02
	$\phi_{e,y}$ (-)	11.25	10.57
	$\phi_{e,z}$ (-)	9.65	11.05
	ϕ_e (-)	16.35	16.97
	r_x (μm)	15.5	-
	r_y (μm)	10.5	-
	r_z (μm)	8.5	-
	C_x (-)	86	-
	C_y (-)	94	-
	C_z (-)	222	-
	k_x (mD)	653	663
	k_y (mD)	287	287
	k_z (mD)	118	72
	R (-)	0.27	0.16

case. Consistent results were obtained for water, gas and heavy oil. Thus, the proposed geometrical approach can be effectively applied to a variety of scenarios characterized by single-phase flow, such as geothermal applications and aquifers, and to

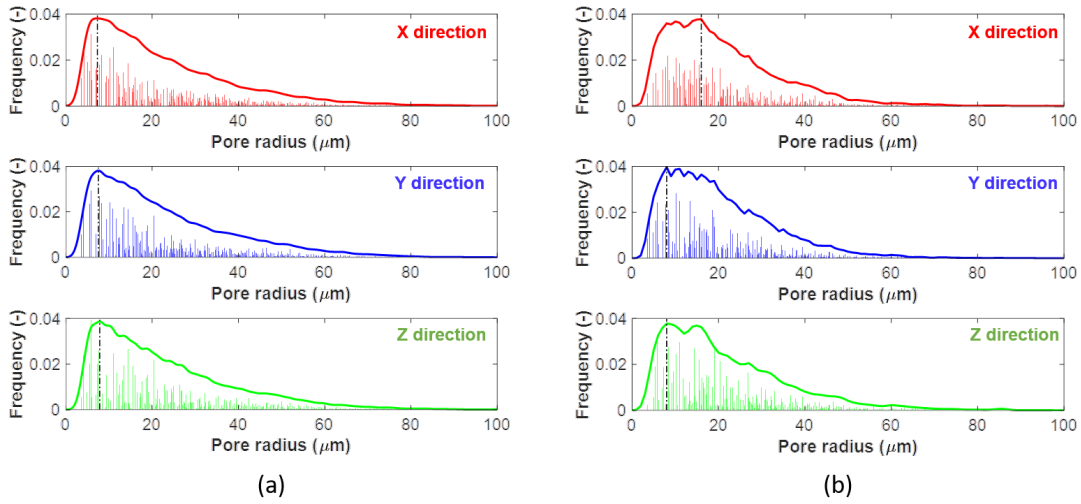

Figure 6.9: Pore radius distribution: a) Case 1; b) Case 2 [75].

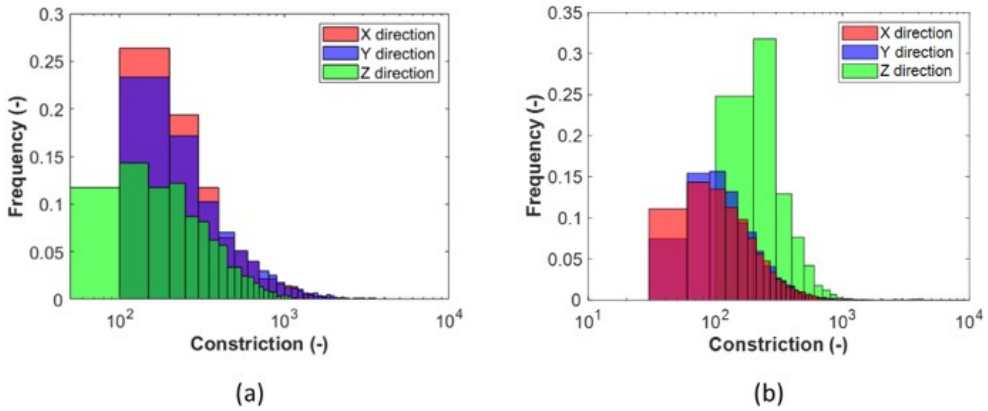

Figure 6.10: Constriction factor distribution: a) Case 1; b) Case 2 [75].

characterize petrophysical properties for gas storage scenarios, including CO_2 and H_2 storage, and reservoir production. However, the proposed geometrical approach cannot account for multiphase flow properties such as contact angle and interfacial tension, which result in relative permeability and capillary pressure effects at the macro scale. These properties affect the fluid flow and the fluid phases preferential paths.

Chapter 7

Conclusions

The aim of this thesis was to propose a methodology based on geometrical analysis and hydrodynamic simulation at the pore-scale for the estimation of microscopic and textural parameters that influence the fluid flow behavior in porous media. To this end, a geometrical analysis based on the A* path-finding algorithm was implemented to characterize the pore network geometry of 2D and 3D binary images of rock samples and the results were compared to hydrodynamic simulations directly in the pore space.

Chapter 2 introduced and discussed the parameters of interest for rock characterization, i.e. tortuosity, effective porosity, permeability, hydraulic radius and constriction factor.

Chapter 3 presented the A* algorithm and its implementation in this work in order to find the shortest paths between inlet and outlet points in 2D and 3D binary images of rocks. A sensitivity analysis showed that the algorithm was robust with respect to the selected number of inlet and outlet points. Furthermore, a methodology based on the A* algorithm to calculate the parameters introduced in Chapter 3 was proposed.

Chapter 4 showed two numerical methods to simulate fluid flow in porous media at the pore-space: the Lattice Boltzmann Method and the Finite Volume Method with pressure-velocity coupling. In this work, the LBM with BGK collision operator was implemented to solve single-phase flow in 2D porous media. Bounce-back boundary condition was applied at the fluid-solid interface and Zou-He boundary condition at open boundaries. A validation test showed that the method and boundary conditions implemented were able to reproduce accurate results for Poiseuille's flow in a 2D microchannel. For the simulation of fluid flow in 3D geometries, the open source code OpenFOAM was used. The pressure-velocity algorithms SIMPLE was used to solve numerically the Navier-Stokes equations and steady-state conditions. Finally, a methodology based on hydrodynamic simulation was adopted to estimate tortuosity, effective porosity and permeability of rock images.

Chapter 5 showed the use of the geometrical analysis based on the A* algorithm

for the characterization of the pore network geometry and connectivity of 2D binary images of rock samples representative of real geological formations. In order to validate the results provided by the geometrical analysis, the LBM code discussed in Chapter 4 was used. Results showed that the geometrical approach produced reasonable estimates of tortuosity and effective porosity and was successfully applied to analyze the distribution of the pore size. Some discrepancies in the results provided by the geometrical and hydrodynamic approaches were present in cases characterized by large pores (i.e. Case 2), or high variability of pore radius along the paths (i.e. Berea B30 and Hostun HO47). In fact, the geometrical approach always selected the shortest paths, without considering the pore size. Thus, the geometrical paths did not always reflect some local flow paths.

In Chapter 6, the geometrical analysis based on the A* algorithm was adopted to characterize the pore network geometry of 3D binary images representative of rock samples. Two cases, isotropic and anisotropic, were generated using the QSGS algorithm, which was modified to generate different types of rocks having different grain size distribution and anisotropy ratio. An algorithm for automatic selection of inlet and outlet points was also proposed (Appendix A). The geometrical analysis was performed to produce a detailed description of the pore space and a tensorial representation of tortuosity, effective porosity, representative pore radius for calculation of permeability and anisotropy. The results provided by the geometrical approach were validated by using the CFD simulator OpenFOAM. Results showed that the geometrical approach was able to characterize tortuosity, effective porosity, permeability, and anisotropy. The results obtained with the two approaches are in good agreement in both cases.

The developed geometrical approach can be applied to a thorough description and characterization of the internal geometry of porous media in terms of pore radius distribution and texture parameters. As a consequence, it can be useful for a variety of scenarios such as geothermal applications, gas storage, including CO_2 and H_2, and reservoir production. Since physical parameters such as interfacial tension and contact angle are not taken into account, multiphase properties cannot be characterized. The proposed geometrical methodology should not be considered as an alternative to CFD simulation but as a possible additional tool for a thorough geometrical description and characterization of the pore network geometry. Another interesting and promising area to apply the methodology described in this work is microfluidics. In fact, microfluidics contributes to the investigation of fluid flow, providing synthetic tools that mimic porous media and enable the direct visualization of the fluid dynamics and the tuning of geometrical features. These devices can also be called micromodels. A microfluidic device is typically constituted by a patterned layer bonded to a transparent covering layer. The integrated usage of experimental and computational microfluidics is a powerful approach to understand the complex mechanisms that occur in geological porous systems. The

methodology reported in this thesis can be a useful tool for the design of microfluidic devices. The geometrical characterization can be used to extract properties such as pore-size distribution and constriction factor and, on the other hand, the hydrodynamic characterization can be used to calculate tortuosity and permeability of the micromodel. These parameters can be used as input for the design of synthetic rocks that have geometrical and transport properties similar to real rocks.

7.1 Future work

Based on the results reported in this thesis, the following suggestions can be studied and developed in future works:

1. Parallelization of the A* algorithm. As discussed in Section 6.3, the A* algorithm is implemented in a prototype Matlab code which is not optimized nor parallelized. The A* algorithm is particularly suitable for parallelization because a path search is independent from the others. For this reason, the current code should be translated to a more efficient programming language and parallelized in order to drop significantly the computational time.

2. Improvement and optimization of the LBM code. First of all, it is necessary to implement the multi-relaxation time to obtain reliable estimates of permeability without increasing significantly the computational time. In fact, a very fine mesh is required in order to keep the Knudsen number smaller than 0.01 as required in simulations with single-relaxation time. However, this is not always possible, especially in simulations on large domains. Secondly, although the code is already compatible to 3D simulations, it has never been tested on 3D cases of porous media. In order to perform 3D simulations on 3D geometries, further optimization of the code is necessary to reduce the computational cost.

3. 3D images of real rocks. In this work, the methodology was applied to 3D synthetic images generated with the QSGS algorithm. It would be interesting to apply the methodology to real 3D images of rocks obtained with micro-CT.

4. Multiphase flow simulation. A further step necessary to study pore-scale phenomena associated to CO_2 and H_2 underground storage is the simulation of multiphase flow in porous media. Multiphase simulations can be used to calculate saturation, capillary pressure and relative permeability curves and to visualize displacement patterns and trapping phenomena such as snap-off and water by-pass.

Appendix A

Automatic selection of inlet and outlet points

In 3D binary images of porous media, boundary faces can be characterized by a significant number of pores and therefore a manual selection of inlet and outlet points could be not efficient and time-consuming. Therefore, an algorithm based on the medial axis algorithm was developed in order to place inlet and outlet points automatically. In order to extract the skeleton of the pore network, the Matlab Image Processing Toolbox was used on 2D images of the boundary faces. Then, the points of the skeleton are grouped in clusters with the K-means algorithm. The number of clusters is fixed to the desired number of inlet and outlet points. The cell centroid nearest to the cluster centroid is selected as an inlet/outlet point. In this way, the selected inlet/outlet points lay on the medial axis and are spread almost uniformly on the pore domain. In Fig. A.1, a 2D inlet surface of a porous medium is showed. The medial axis of the pore space network is represented in cyan. The algorithm individuated automatically 150 inlet points depicted in blue.

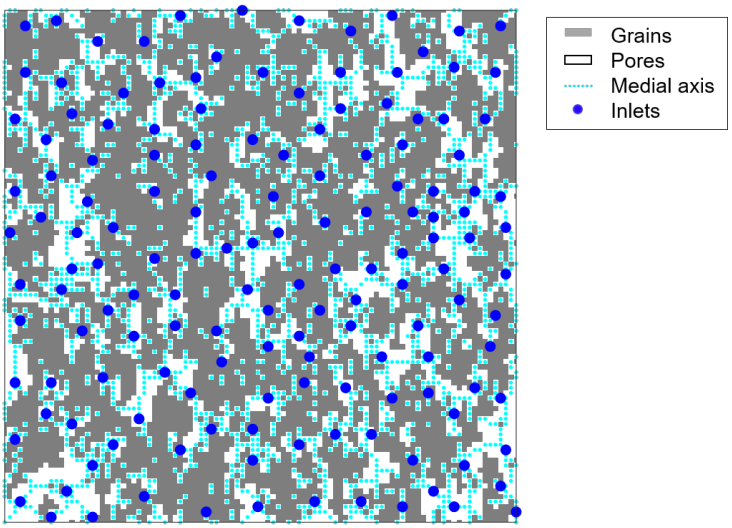

Figure A.1: Example of a boundary surface with automatic identification of inlets [75].

Nomenclature

Δt: Time step size

Δx: Cell size

$\mathbf{A}$: Matrix of diagonal coefficients

$\mathbf{c}$: Microscopic velocity, m/s

$\mathbf{c}_i$: Lattice velocity

$\mathbf{d}$: Distance vector between two centroids

$\mathbf{H}$: Matrix of off-diagonal coefficients

$\mathbf{M}$: Matrix of coefficients

$\mathbf{S}_f$: Surface vector normal to the cell face

$\mathbf{u}$: Local (i.e. pore-scale) velocity, m/s

$\mathbf{U}_D$: Darcy's velocity, m/s

Ma: Mach number

Re: Reynolds number

μ: Dynamic viscosity, Pa s

ν: Kinematic viscosity, m^2/s^2

Ω: Collision operator

ϕ: Porosity

ϕ_c: Connected porosity

ϕ_e: Effective porosity

ρ: Density, kg/m^3

τ: Relaxation time

τ_g: Geometrical tortuosity

τ_h: Hydraulic tortuosity

R: Anisotropy

φ: Arbitrary variable

A_w: Wetted area, m^2

C: Constriction factor

$c(n_i)$: A* cost function

c_d: Connecting distance

c_k: Kozeny's constant

c_s: Sound speed

D_i Growth probability

E: Error

F: Cell volume flux

f: Particle distribution function

f^{eq}: Equilibrium particle distribution function

f_i: Discrete particle distribution function (also called population)

f_i^{post}: Post-collision discrete particle distribution function

$g(n_i)$: A* backward cost

$h(n_i)$: A* forward cost

k: Permeability, m^2

P Distribution probability

p: Pressure, Pa

r_H: Hydraulic radius, m

r_p: Equivalent pore radius, m

S: Surface

V: Volume

w_i: Weights depending on the lattice velocity direction

BGK: Bhatnagar-Gross-Krook

CFD: Computational Fluid Dynamics

FIB-SEM: Focused Ion Beam-Scanning Electron Microscopy

FVM: Finite Volume Method

LBM: Lattice Boltzmann Method

LUD: Linear Upwind Differencing

Micro-CT: X-ray micro-computed tomography

NSEs: Navier-Stokes Equations

PISO: Pressure-Implicit with Splitting of Operators

QSGS: Quartet Structure Generation Set

REV: Representative Elementary Volume

SEM Scanning Electron Microscopy

SIMPLE: Semi-Implicit Method for Pressure Linked Equations

Bibliography

1. Satter, A., Varnon, J. E. & Hoang, M. T. Integrated reservoir management. *Journal of Petroleum Technology* **46,** 1057–1064 (1994).
2. Verga, F. What's conventional and what's special in a reservoir study for underground gas storage. *Energies* **11,** 1245 (2018).
3. Cui, G. *et al.* Whole process analysis of geothermal exploitation and power generation from a depleted high-temperature gas reservoir by recycling CO2. *Energy* **217,** 119340 (2021).
4. Heinemann, N. *et al.* Enabling large-scale hydrogen storage in porous media–the scientific challenges. *Energy & Environmental Science* **14,** 853–864 (2021).
5. Zivar, D., Kumar, S. & Foroozesh, J. Underground hydrogen storage: A comprehensive review. *International Journal of Hydrogen Energy* **46,** 23436–23462 (2021).
6. Kelemen, P., Benson, S. M., Pilorgé, H., Psarras, P. & Wilcox, J. An overview of the status and challenges of CO2 storage in minerals and geological formations. *Frontiers in Climate* **1,** 9 (2019).
7. Bear, J. *Dynamics of fluids in porous media* (ed Publications, D.) (American Elsevier Publishing Company, 1972).
8. Blunt, M. J. *Multiphase flow in permeable media: A pore-scale perspective* (Cambridge University Press, 2017).
9. Casnedi, R. Geological characteristics of hydrocarbon reservoirs. *Encyclopaedia of Hydrocarbons* **1** (2005).
10. Knebel, G. M. & Rodriguez-Eraso, G. Habitat of some oil. *AAPG Bulletin* **40,** 547–561 (1956).
11. Boggs Jr, S. *Principles of sedimentology and stratigraphy* (Pearson Education, 2014).
12. Benetatos, C. & Viberti, D. Fully integrated hydrocarbon reservoir studies: myth or reality? *American Journal of Applied Sciences* **7,** 1477 (2010).

13. Panini, F., Onur, M. & Viberti, D. An Analytical Solution and Nonlinear Regression Analysis for Sandface Temperature Transient Data in the Presence of a Near-Wellbore Damaged Zone. *Transport in Porous Media* **129,** 779–810 (2019).

14. Viberti, D. A rigorous mathematical approach for petrophysical properties estimation. *American Journal of Applied Sciences* **7,** 1509 (2010).

15. Salina Borello, E. *et al.* Harmonic pulse testing for well monitoring: Application to a fractured geothermal reservoir. *Water Resources Research* **55,** 4727–4744 (2019).

16. Viberti, D. & Verga, F. An approach for the reliable evaluation of the uncertainties associated to petrophysical properties. *Mathematical Geosciences* **44,** 327–341 (2012).

17. Horne, R. *Uncertainty in well test interpretation* in *University of Tulsa Centennial Petroleum Engineering Symposium* (1994).

18. Battiato, I. *et al.* Theory and applications of macroscale models in porous media. *Transport in Porous Media* **130,** 5–76 (2019).

19. Hunt, A. G. & Sahimi, M. Flow, transport, and reaction in porous media: Percolation scaling, critical-path analysis, and effective medium approximation. *Reviews of Geophysics* **55,** 993–1078 (2017).

20. Rahman, T., Ramandi, H. L., Roshan, H. & Iglauer, S. Representative Elementary Volume of Rock Using X-Ray Microcomputed Tomography: A New Statistical Approach. *Geofluids* **2020** (2020).

21. Al-Raoush, R. & Willson, C. Extraction of physically realistic pore network properties from three-dimensional synchrotron X-ray microtomography images of unconsolidated porous media systems. *Journal of hydrology* **300,** 44–64 (2005).

22. Viggiani, G., Hall, S. A. & E., R. *ALERT Doctoral School 2012. Advanced experimental techniques in geomechanics* (The Alliance of Laboratories in Europe for Research and Technology, 2012).

23. Raeini, A. Q. *Modelling multiphase flow through micro-CT images of the pore space* PhD thesis (Imperial College London, 2013).

24. Raeini, A. Q., Blunt, M. J. & Bijeljic, B. Direct simulations of two-phase flow on micro-CT images of porous media and upscaling of pore-scale forces. *Advances in water resources* **74** (2014).

25. https://www.imperial.ac.uk/earth-science/research/research-groups/pore-scale-modelling/micro-ct-images-and-networks/.

26. Telmadarreie, A. & Trivedi, J. J. CO2 Foam and CO2 Polymer Enhanced Foam for Heavy Oil Recovery and CO2 Storage. *Energies* **13,** 5735 (2020).

27. Hovorka, S. D. *et al.* Comparing carbon sequestration in an oil reservoir to sequestration in a brine formation—field study. *Energy Procedia* **1,** 2051–2056 (2009).

28. Mostaghimi, P. *Transport Phenomena Modelled on Pore-Space Images* PhD thesis (Imperial College London, 2012).

29. Wildenschild, D. & Sheppard, A. P. X-ray imaging and analysis techniques for quantifying pore-scale structure and processes in subsurface porous medium systems. *Advances in Water Resources* **51,** 217–246 (2013).

30. Kelly, S., El-Sobky, H., Torres-Verdin, C. & Balhoff, M. T. Assessing the utility of FIB-SEM images for shale digital rock physics. *Advances in water resources* **95,** 302–316 (2016).

31. Blunt, M. J. *et al.* Pore-scale imaging and modelling. *Advances in Water resources* **51,** 197–216 (2013).

32. Zhu, L. *et al.* Challenges and prospects of digital core-reconstruction research. *Geofluids* **2019** (2019).

33. Coles, M. *et al.* Developments in synchrotron X-ray microtomography with applications to flow in porous media. *SPE Reservoir Evaluation & Engineering* **1,** 288–296 (1998).

34. Gong, L., Nie, L. & Xu, Y. Geometrical and topological analysis of pore space in sandstones based on x-ray computed tomography. *Energies* **13,** 3774 (2020).

35. Bera, B., Mitra, S. K. & Vick, D. Understanding the micro structure of Berea Sandstone by the simultaneous use of micro-computed tomography (micro-CT) and focused ion beam-scanning electron microscopy (FIB-SEM). *Micron* **42,** 412–418 (2011).

36. Peng, S., Hu, Q., Dultz, S. & Zhang, M. Using X-ray computed tomography in pore structure characterization for a Berea sandstone: Resolution effect. *Journal of Hydrology* **472,** 254–261 (2012).

37. Lindquist, W. B., Lee, S. M., Coker, D. A., Jones, K. W. & Spanne, P. Medial Axis Analysis of Void Structure in Three-Dimensional Tomographic Images of Porous Media. *Journal of Geophysical Research* **101,** 8297–8310 (1996).

38. Rabbani, A. & Ayatollahi, S. Comparing three image processing algorithms to estimate the grain-size distribution of porous rocks from binary 2D images and sensitivity analysis of the grain overlapping degree. *Special Topics and Reviews in Porous Media* **6,** 71–89 (Jan. 2015).

39. Mostaghimi, P., Blunt, M. J. & Bijeljic, B. Computations of absolute permeability on micro-CT images. *Mathematical Geosciences* **45,** 103–125 (2013).

40. Shah, S., Gray, F., Crawshaw, J. & Boek, E. Micro-computed tomography pore-scale study of flow in porous media: Effect of voxel resolution. *Advances in Water Resources* **95,** 276–287 (2016).

41. Vlahinic, I., Andò, E., Viggiani, G. & Andrade, J. Towards a more accurate characterization of granular media: Extracting quantitative descriptors from tomographic images. *Granular Matter* **16** (Feb. 2014).

42. Nan, N. & Wang, J. FIB-SEM three-dimensional tomography for characterization of carbon-based materials. *Advances in Materials Science and Engineering* **2019** (2019).

43. Elliott, J. C. & Dover, S. X-ray microtomography. *Journal of microscopy* **126,** 211–213 (1982).

44. Flannery, B. P., Deckman, H. W., Roberge, W. G. & D'amico, K. L. Three-dimensional X-ray microtomography. *Science* **237,** 1439–1444 (1987).

45. Hashemi, M. A., Khaddour, G., François, B., Massart, T. J. & Salager, S. A tomographic imagery segmentation methodology for three-phase geomaterials based on simultaneous region growing. *Acta Geotechnica* **9,** 831–846 (Oct. 2014).

46. Wildenschild, D., Culligan, K. A. & Christensen, B. S. *Application of x-ray microtomography to environmental fluid flow problems* in *Developments in X-ray tomography IV* **5535** (2004), 432–441.

47. Zhang, D., Zhang, R., Chen, S. & Soll, W. E. Pore scale study of flow in porous media: Scale dependency, REV, and statistical REV. *Geophysical research letters* **27,** 1195–1198 (2000).

48. Costanza-Robinson, M. S., Estabrook, B. D. & Fouhey, D. F. Representative elementary volume estimation for porosity, moisture saturation, and air-water interfacial areas in unsaturated porous media: Data quality implications. *Water Resources Research* **47** (2011).

49. Ferrari, A. *Pore-scale modeling of two-phase flow instabilities in porous media* PhD thesis (Université de Lausanne, Faculté des géosciences et de l'environnement, 2014).

50. Okabe, H. & Oseto, K. Pore-scale heterogeneity assessed by the lattice-Boltzmann method. *Society of Core Analysts (SCA2006-44),* 12–16 (2006).

51. Jackson, S., Lin, Q. & Krevor, S. Representative Elementary Volumes, Hysteresis, and Heterogeneity in Multiphase Flow From the Pore to Continuum Scale. *Water Resources Research* **56** (2020).

52. Whitaker, S. *The method of volume averaging* (Springer Science & Business Media, 1999).

53. Whitaker, S. Flow in porous media I: A theoretical derivation of Darcy's law. *Transport in porous media* **1,** 3–25 (1986).

54. Ghanbarian, B., Hunt, A. G., Ewing, R. P. & Sahimi, M. Tortuosity in porous media: a critical review. *Soil science society of America journal* **77,** 1461–1477 (2013).

55. Carman, P. C. Fluid flow through granular beds. *Trans. Inst. Chem. Eng.* **15,** 150–166 (1937).

56. Clennell, M. Tortuosity: A guide through the maze. *Geological Society, London, Special Publications* **122,** 299–344 (Jan. 1997).

57. Koponen, A., Kataja, M. & Timonen, J. Tortuous Flow in Porous Media. *Physical review E* **54,** 406–410 (Aug. 1996).

58. Koponen, A., Kataja, M. & Timonen, J. Permeability and effective porosity of porous media. *Physical Review E* **56,** 3319 (1997).

59. Ahmed, T. *Reservoir Engineering Handbook* ISBN: 978-1-85617-803-7 (Elsevier, 2010).

60. Dullien, F. A. *Porous media: fluid transport and pore structure* (Academic press, 1992).

61. Scheidegger, A. E. *The Physics of Flow Through Porous Media (3rd Edition)* (University of Toronto Press, 1974).

62. Wyllie, M. & Spangler, M. Application of electrical resistivity measurements to problem of fluid flow in porous media. *AAPG Bulletin* **36,** 359–403 (1952).

63. Corey, A. T. *et al. Mechanics of heterogeneous fluids in porous media.* (Water Resources Publications., 1977).

64. Berg, C. F. Permeability description by characteristic length, tortuosity, constriction and porosity. *Transport in porous media* **103,** 381–400 (2014).

65. Yi, Z. *et al.* Pore network extraction from pore space images of various porous media systems. *Water Resources Research* **53,** 3424–3445 (2017).

66. Arand, F. & Hesser, J. Accurate and efficient maximal ball algorithm for pore network extraction. *Computers & Geosciences* **101,** 28–37 (2017).

67. An, S. *et al.* Influence of pore structure parameters on flow characteristics based on a digital rock and the pore network model. *Journal of Natural Gas Science and Engineering* **31,** 156–163 (2016).

68. Blunt, M. J. Flow in porous media—pore-network models and multiphase flow. *Current opinion in colloid & interface science* **6,** 197–207 (2001).

69. Lock, P. A., Jing, X., Zimmerman, R. W. & Schlueter, E. M. Predicting the permeability of sandstone from image analysis of pore structure. *Journal of applied physics* **92,** 6311–6319 (2002).

70. Al-Raoush, R. I. & Madhoun, I. T. TORT3D: A MATLAB code to compute geometric tortuosity from 3D images of unconsolidated porous media. *Powder technology* **320,** 99–107 (2017).

71. Keller, L. M., Holzer, L., Wepf, R. & Gasser, P. 3D geometry and topology of pore pathways in Opalinus clay: Implications for mass transport. *Applied Clay Science* **52,** 85–95 (2011).

72. Sun, W. C., Andrade, J. E. & Rudnicki, J. W. Multiscale method for characterization of porous microstructures and their impact on macroscopic effective permeability. *International Journal for Numerical Methods in Engineering* **88,** 1260–1279 (2011).

73. Viberti, D., Peter, C., Borello, E. S. & Panini, F. Pore structure characterization through path-finding and lattice Boltzmann simulation. *Advances in Water Resources* **141,** 103609 (2020).

74. Panini, F., Salina Borello, E., Peter, C. & Viberti, D. Application of a* Algorithm for Tortuosity and Effective Porosity Estimation of 2D Rock Images. *Advanced Problem in Mechanics II. Lecture Notes in Mechanical Engineering* (2022).

75. Salina Borello, E., Peter, C., Panini, F. & Viberti, D. Application of A* algorithm for microstructure and transport properties characterization from 3D rock images. *Energy* **239,** 122151 (2022).

76. Hart, P. E., Nilsson, N. J. & Raphael, B. A formal basis for the heuristic determination of minimum cost paths. *IEEE transactions on Systems Science and Cybernetics* **4,** 100–107 (1968).

77. Nilsson, N. J. *Principles of artificial intelligence* ISBN: 0935382011 (Tioga Pub. Co., Palo Alto, CA, 1980).

78. Nilsson, N. J. *Principles of artificial intelligence* ISBN: 9781483295862 (Morgan Kaufmann, 2014).

79. Russell, S. & Norvig, P. Artificial intelligence: a modern approach (2002).

80. Dias, R., Teixeira, J. A., Mota, M. & Yelshin, A. Tortuosity variation in a low density binary particulate bed. *Separation and Purification Technology* **51,** 180–184 (2006).

81. Sobieski, W. & Lipiński, S. The analysis of the relations between porosity and tortuosity in granular beds. *Technical Sciences/University of Warmia and Mazury in Olsztyn* (2017).

82. Mauran, S., Rigaud, L. & Coudevylle, O. Application of the Carman–Kozeny correlation to a high-porosity and anisotropic consolidated medium: the compressed expanded natural graphite. *Transport in porous media* **43,** 355–376 (2001).

83. Li, K. & Horne, R. Fractal Characterization of the geysers rock. *Geothermal Resources Council Transactions* **27** (2003).

84. Øren, P. E. & Bakke, S. Reconstruction of Berea sandstone and pore-scale modelling of wettability effects. *Journal of Petroleum Science and Engineering* **39,** 177–199 (2003).

85. Xiao, B. *et al.* A novel fractal solution for permeability and Kozeny-Carman constant of fibrous porous media made up of solid particles and porous fibers. *Powder Technology* **349,** 92–98 (2019).

86. Mathworks. *Image Processing Toolbox User's Guide* (The Mathworks, Inc., 2017).

87. Fatt, I. The network model of porous media. *Transactions of the AIME* **207,** 144–181 (1956).

88. Blunt, M. J., Jackson, M. D., Piri, M. & Valvatne, P. H. Detailed physics, predictive capabilities and macroscopic consequences for pore-network models of multiphase flow. *Advances in Water Resources* **25,** 1069–1089 (2002).

89. Xiong, Q., Baychev, T. G. & Jivkov, A. P. Review of pore network modelling of porous media: experimental characterisations, network constructions and applications to reactive transport. *Journal of contaminant hydrology* **192,** 101–117 (2016).

90. Tartakovsky, A. M. & Meakin, P. Pore scale modeling of immiscible and miscible fluid flows using smoothed particle hydrodynamics. *Advances in Water Resources* **29,** 1464–1478 (2006).

91. Tartakovsky, A. M., Ward, A. L. & Meakin, P. Pore-scale simulations of drainage of heterogeneous and anisotropic porous media. *Physics of Fluids* **19,** 103301 (2007).

92. Bandara, U. C., Tartakovsky, A. M. & Palmer, B. J. Pore-scale study of capillary trapping mechanism during CO2 injection in geological formations. *International Journal of Greenhouse Gas Control* **5,** 1566–1577 (2011).

93. Kunz, P. *et al.* Study of multi-phase flow in porous media: comparison of SPH simulations with micro-model experiments. *Transport in Porous Media* **114,** 581–600 (2016).

94. Meakin, P. & Tartakovsky, A. M. Modeling and simulation of pore-scale multiphase fluid flow and reactive transport in fractured and porous media. *Reviews of Geophysics* **47** (2009).

95. Benzi, R., Succi, S. & Vergassola, M. The lattice Boltzmann equation: theory and applications. *Physics Reports* **222,** 145–197 (1992).

96. Chen, S. & Doolen, G. D. Lattice Boltzmann Method For Fluid Flows. *Annual Review of Fluid Mechanics* **30,** 329–364 (1998).

97. Guo, Z. & Zhao, T. Lattice Boltzmann model for incompressible flows through porous media. *Physical review. E, Statistical, nonlinear, and soft matter physics* **66,** 036304 (Oct. 2002).

98. Krüger, T. *et al. The lattice Boltzmann method: Principles and Practice* (Springer, 2017).

99. Tu, J., Yeoh, G. H. & Liu, C. *Computational fluid dynamics: a practical approach* (Butterworth-Heinemann, 2018).

100. Succi, S. *The Lattice Boltzmann Method for Fluid Dynamics and Beyond* (2001).

101. Bhatnagar, P. L., Gross, E. P. & Krook, M. A model for collision processes in gases. I. Small amplitude processes in charged and neutral one-component systems. *Physical review* **94,** 511 (1954).

102. Pan, C., Luo, L. & Miller, C. An evaluation of Lattice Boltzmann schemes for porous medium flow simulation. *Computers & Fluids - COMPUT FLUIDS* **35** (2006).

103. Eshghinejadfard, A., Daroczy, L., Janiga, G. & Thevenin, D. Calculation of the permeability in porous media using the lattice Boltzmann method. *International Journal of Heat and Fluid Flow* **62,** 93–103 (2016).

104. Prestininzi, P., Montessori, A., La Rocca, M. & Succi, S. Reassessing the single relaxation time lattice Boltzmann method for the simulation of Darcy's flows. *International Journal of Modern Physics C* **27,** 1650037 (2015).

105. Succi, S. *The lattice Boltzmann equation: for fluid dynamics and beyond* (Oxford university press, 2001).

106. Gunstensen, A. K., Rothman, D. H., Zaleski, S. & Zanetti, G. Lattice Boltzmann model of immiscible fluids. *Physical Review A* **43,** 4320 (1991).

107. Shan, X. & Chen, H. Lattice Boltzmann model for simulating flows with multiple phases and components. *Physical review E* **47,** 1815 (1993).

108. Swift, M. R., Orlandini, E., Osborn, W. & Yeomans, J. Lattice Boltzmann simulations of liquid-gas and binary fluid systems. *Physical Review E* **54,** 5041 (1996).

109. He, X., Chen, S. & Zhang, R. A lattice Boltzmann scheme for incompressible multiphase flow and its application in simulation of Rayleigh–Taylor instability. *Journal of computational physics* **152,** 642–663 (1999).

110. Fakhari, A., Mitchell, T., Leonardi, C. & Bolster, D. Improved locality of the phase-field lattice-Boltzmann model for immiscible fluids at high density ratios. *Physical Review E* **96,** 053301 (2017).

111. Lee, T. & Lin, C.-L. A stable discretization of the lattice Boltzmann equation for simulation of incompressible two-phase flows at high density ratio. *Journal of Computational Physics* **206,** 16–47 (2005).

112. Jacqmin, D. Calculation of two-phase Navier–Stokes flows using phase-field modeling. *Journal of Computational Physics* **155,** 96–127 (1999).

113. Leclaire, S., Pellerin, N., Reggio, M. & Trépanier, J.-Y. An approach to control the spurious currents in a multiphase lattice Boltzmann method and to improve the implementation of initial condition. *International Journal for Numerical Methods in Fluids* **77,** 732–746 (2015).

114. Chen, Y., Li, Y., Valocchi, A. J. & Christensen, K. T. Lattice Boltzmann simulations of liquid CO2 displacing water in a 2D heterogeneous micromodel at reservoir pressure conditions. *Journal of contaminant hydrology* **212,** 14–27 (2018).

115. Fakhari, A., Li, Y., Bolster, D. & Christensen, K. T. A phase-field lattice Boltzmann model for simulating multiphase flows in porous media: Application and comparison to experiments of CO2 sequestration at pore scale. *Advances in water resources* **114,** 119–134 (2018).

116. Huang, H., Sukop, M. & Lu, X. *Multiphase lattice Boltzmann methods: Theory and application* (John Wiley & Sons, 2015).

117. Nabovati, A. & Sousa, A. Fluid Flow Simulation in Random Porous Media at Pore Level Using Lattice Boltzmann Method. *Journal of Engineering Science and Technology* **2** (Dec. 2007).

118. Matyka, M., Khalili, A. & Koza, Z. Tortuosity-porosity relation in porous media flow. *Physical review E* **78,** 026306 (Sept. 2008).

119. Wang, P. Lattice Boltzmann Simulation of Permeability and Tortuosity for Flow through Dense Porous Media. *Mathematical Problems in Engineering* **2014** (July 2014).

120. Ferreol, B. & Rothman, D. H. Lattice-Boltzmann simulations of flow through Fontainebleau sandstone. *In Multiphase flow in porous media,* 3–20 (1995).

121. Xu, M. & Liu, H. Prediction of immiscible two-phase flow properties in a two-dimensional Berea sandstone using the pore-scale lattice Boltzmann simulation. *Eur. Phys. J.* **41** (2018).

122. Wang, J., Chen, L., Kang, Q. & Rahman, S. S. The lattice Boltzmann method for isothermal micro-gaseous flow and its application in shale gas flow: A review. *International Journal of Heat and Mass Transfer* **95,** 94–108 (2016).

123. Benamram, Z., Tarakanov, A., Nasrabadi, H. & Gildin, E. Field-wide flow simulation in fractured porous media within lattice Boltzmann framework. *Advances in Water Resources* **96,** 170–179 (2016).

124. Ahkami, M., Parmigiani, A., Di Palma, P. R., Saar, M. O. & Kong, X.-Z. A lattice-Boltzmann study of permeability-porosity relationships and mineral precipitation patterns in fractured porous media. *Computational Geosciences,* 1–18 (2020).

125. Liang, H., Shi, B. & Chai, Z. Lattice Boltzmann modeling of three-phase incompressible flows. *Physical Review E* **93,** 013308 (2016).

126. Zacharoudiou, I. & Boek, E. S. Capillary filling and Haines jump dynamics using free energy Lattice Boltzmann simulations. *Advances in water resources* **92,** 43–56 (2016).

127. Venturoli, M. & Boek, E. S. Two-dimensional lattice-Boltzmann simulations of single phase flow in a pseudo two-dimensional micromodel. *Physica A: Statistical Mechanics and its Applications* **362,** 23–29 (2006).

128. Laleian, A., Valocchi, A. J. & Werth, C. J. An incompressible, depth-averaged lattice Boltzmann method for liquid flow in microfluidic devices with variable aperture. *Computation* **3,** 600–615 (2015).

129. Boek, E. S. & Venturoli, M. Lattice-Boltzmann studies of fluid flow in porous media with realistic rock geometries. *Computers and Mathematics with Applications* **59,** 2305–2314 (2010).

130. Wu, M. *et al.* Single-and two-phase flow in microfluidic porous media analogs based on Voronoi tessellation. *Lab on a Chip* **12,** 253–261 (2012).

131. Liu, H., Zhang, Y. & Valocchi, A. J. Lattice Boltzmann simulation of immiscible fluid displacement in porous media: Homogeneous versus heterogeneous pore network. *Physics of Fluids* **27,** 052103 (2015).

132. Isfahani, A. M. & Afrand, M. Experiment and Lattice Boltzmann numerical study on nanofluids flow in a micromodel as porous medium. *Physica E: Low-dimensional Systems and Nanostructures* **94,** 15–21 (2017).

133. Soulaine, C., Maes, J. & Roman, S. Computational microfluidics for geosciences. *Frontiers in Water* **3,** 11 (2021).

134. Issa, R. I. Solution of the implicitly discretised fluid flow equations by operator-splitting. *Journal of computational physics* **62,** 40–65 (1986).

135. Patankar, S. *Numerical heat transfer and fluid flow* (Taylor & Francis, 2018).

136. Rusche, H. *Computational fluid dynamics of dispersed two-phase flows at high phase fractions* PhD thesis (Imperial College London (University of London), 2003).

137. Raeini, A. Q., Blunt, M. J. & Bijeljic, B. Modelling two-phase flow in porous media at the pore scale using the volume-of-fluid method. *Journal of Computational Physics* **231,** 5653–5668 (2012).

138. Hirt, C. W. & Nichols, B. D. Volume of fluid (VOF) method for the dynamics of free boundaries. *Journal of computational physics* **39,** 201–225 (1981).

139. Hoang, D. A., van Steijn, V., Portela, L. M., Kreutzer, M. T. & Kleijn, C. R. Benchmark numerical simulations of segmented two-phase flows in microchannels using the Volume of Fluid method. *Computers & Fluids* **86,** 28–36 (2013).

140. Horgue, P., Augier, F., Duru, P., Prat, M. & Quintard, M. Experimental and numerical study of two-phase flows in arrays of cylinders. *Chemical Engineering Science* **102,** 335–345 (2013).

141. Ferrari, A., Jimenez-Martinez, J., Borgne, T. L., Méheust, Y. & Lunati, I. Challenges in modeling unstable two-phase flow experiments in porous micromodels. *Water Resources Research* **51,** 1381–1400 (2015).

142. Yin, X., Zarikos, I., Karadimitriou, N., Raoof, A. & Hassanizadeh, S. Direct simulations of two-phase flow experiments of different geometry complexities using Volume-of-Fluid (VOF) method. *Chemical Engineering Science* **195,** 820–827 (2019).

143. Zhao, J., Yao, G. & Wen, D. Pore-scale simulation of water/oil displacement in a water-wet channel. *Frontiers of Chemical Science and Engineering* **13,** 803–814 (2019).

144. Konangi, S., Palakurthi, N. K., Karadimitriou, N. K., Comer, K. & Ghia, U. Comparison of pore-scale capillary pressure to macroscale capillary pressure using direct numerical simulations of drainage under dynamic and quasi-static conditions. *Advances in Water Resources* **147,** 103792 (2021).

145. Brackbill, J. U., Kothe, D. B. & Zemach, C. A continuum method for modeling surface tension. *Journal of computational physics* **100,** 335–354 (1992).

146. Renardy, Y. & Renardy, M. PROST: a parabolic reconstruction of surface tension for the volume-of-fluid method. *Journal of computational physics* **183,** 400–421 (2002).

147. Lafaurie, B., Nardone, C., Scardovelli, R., Zaleski, S. & Zanetti, G. Modelling merging and fragmentation in multiphase flows with SURFER. *Journal of Computational Physics* **113,** 134–147 (1994).

148. Pavuluri, S., Maes, J. & Doster, F. Spontaneous imbibition in a microchannel: Analytical solution and assessment of volume of fluid formulations. *Microfluidics and Nanofluidics* **22,** 1–18 (2018).

149. McNamara, G. R. & Zanetti, G. Use of the Boltzmann equation to simulate lattice-gas automata. *Physical review letters* **61,** 2332 (1988).

150. Qian, Y.-H., d'Humières, D. & Lallemand, P. Lattice BGK models for Navier-Stokes equation. *EPL (Europhysics Letters)* **17,** 479 (1992).

151. He, X. & Luo, L.-S. Lattice Boltzmann model for the incompressible Navier–Stokes equation. *Journal of statistical Physics* **88,** 927–944 (1997).

152. He, X. & Luo, L.-S. Theory of the lattice Boltzmann method: From the Boltzmann equation to the lattice Boltzmann equation. *Physical review E* **56,** 6811 (1997).

153. Ulam, S. *Random processes and transformations* in *Proceedings of the International Congress on Mathematics* **2** (1952), 264–275.

154. Neumann, J. & Burks, A. W. *Theory of self-reproducing automata* (University of Illinois press Urbana, 1966).

155. Zuse, K. *Calculating space* (Massachusetts Institute of Technology, Project MAC Cambridge, MA, 1970).

156. Hardy, J., Pomeau, Y. & De Pazzis, O. Time evolution of a two-dimensional model system. I. Invariant states and time correlation functions. *Journal of Mathematical Physics* **14,** 1746–1759 (1973).

157. Frisch, U., Hasslacher, B. & Pomeau, Y. Lattice-gas automata for the Navier-Stokes equation. *Physical review letters* **56,** 1505 (1986).

158. Asinari, P. *Multi-scale analysis of heat and mass transfer in mini/micro-structures* PhD thesis (Politecnico di Torino, 2005).

159. Reynolds, W. C. & Colonna, P. *Thermodynamics* (Cambridge University Press, 2018).

160. Chapman, S. & Cowling, T. G. *The mathematical theory of non-uniform gases: an account of the kinetic theory of viscosity, thermal conduction and diffusion in gases* (Cambridge university press, 1953).

161. Latt, J., Chopard, B., Malaspinas, O., Deville, M. & Michler, A. Straight velocity boundaries in the lattice Boltzmann method. *Physical Review E* **77,** 056703 (2008).

162. Zou, Q. & He, X. On pressure and velocity boundary conditions for the lattice Boltzmann BGK model. *Physics of fluids* **9,** 1591–1598 (1997).

163. Chen, Z., Shu, C. & Tan, D. A simplified thermal lattice Boltzmann method without evolution of distribution functions. *International Journal of Heat and Mass Transfer* **105,** 741–757 (2017).

164. Jasak, H. *Error analysis and estimation for the finite volume method with applications to fluid flows.* PhD thesis (1996).

165. Versteeg, H. K. & Malalasekera, W. *An introduction to computational fluid dynamics: the finite volume method* (Pearson education, 2007).

166. Guerrero, J. *A Crash Introduction to the Finite Volume Method and Discretization Schemes in OpenFOAM®* 2020.

167. Barth, T. & Jespersen, D. *The design and application of upwind schemes on unstructured meshes* in *27th Aerospace sciences meeting* (1989), 366.

168. Aminpour, M., Galindo-Torres, S. A., Scheuermann, A. & Li, L. Pore-Scale Behavior of Darcy Flow in Static and Dynamic Porous Media. *Phys. Rev. Applied* **9,** 064025 (6 June 2018).

169. Ergun, S. & Orning, A. A. Fluid flow through randomly packed columns and fluidized beds. *Industrial & Engineering Chemistry* **41,** 1179–1184 (1949).

170. Ergun, S. Fluid flow through packed columns. *Chem. Eng. Prog.* **48,** 89–94 (1952).

171. Papathanasiou, T., Markicevic, B. & Dendy, E. A computational evaluation of the Ergun and Forchheimer equations for fibrous porous media. *Physics of Fluids* **13,** 2795–2804 (2001).

172. Mostaghimi, P., Bijeljic, B., Blunt, M., *et al.* Simulation of flow and dispersion on pore-space images. *SPE Journal* **17,** 1–131 (2012).

173. Guibert, R. *et al.* Computational permeability determination from pore-scale imaging: sample size, mesh and method sensitivities. *Transport in Porous Media* **107,** 641–656 (2015).

174. Gao, Z. & Hu, Q.-H. Investigating the effect of median pore-throat diameter on spontaneous imbibition. *Journal of Porous Media* **18,** 1231–1238 (Jan. 2015).

175. Vitorge, E., Szenknect, S., Martins, J. & Gaudet, J.-P. Size and concentration-dependent deposition of fluorescent silica colloids in saturated sand columns: Transport experiments and modeling. *Environmental science. Processes and impacts* **15** (July 2013).

176. Andó, E., Hall, S. A., Viggiani, G., Desrues, J. & Bésuelle, P. Grain-scale experimental investigation of localised deformation in sand: a discrete particle tracking approach. *Acta Geotechnica* **7,** 1–13 (2012).

177. Churcher, P., French, P., Shaw, J., Schramm, L., *et al. Rock properties of Berea sandstone, Baker dolomite, and Indiana limestone* in *SPE International Symposium on Oilfield Chemistry* **20** (1991), 22.

178. Sato, M., Panaghi, K., Takada, N. & Takeda, M. Effect of Bedding Planes on the Permeability and Diffusivity Anisotropies of Berea Sandstone. *Transport in Porous Media* **127,** 587–603 (2019).

179. Kim, K. Y., Zhuang, L., Yang, H., Kim, H. & Min, K.-B. Strength anisotropy of Berea sandstone: results of X-ray computed tomography, compression tests, and discrete modeling. *Rock Mechanics and Rock Engineering* **49,** 1201–1210 (2016).

180. Sharma, T., Suresh Kumar, G. & Sangwai, J. S. Enhanced oil recovery using oil-in-water (o/w) emulsion stabilized by nanoparticle, surfactant and polymer in the presence of NaCl. *Geosystem Engineering* **17,** 195–205 (2014).

181. Gu, Q., Liu, H. & Zhang, Y. Lattice Boltzmann Simulation of Immiscible Two-Phase Displacement in Two-Dimensional Berea Sandstone. *Applied Sciences* **8,** 1497 (Aug. 2018).

182. Viggiani, G., Bésuelle, P., Hall, S. & Desrues, J. Sand deformation at the grain scale quantified through X-ray imaging. *Advances in Computed Tomography for Geomaterials: GeoX 2010,* 1–16 (2010).

183. Ando, E. *Experimental investigation of microstructural changes in deforming granular media using x-ray tomography* PhD dissertation (Université de Grenoble, 2013).

184. *Geometry of Pore Structure in Pressurized Berea Sandstone.* (International Society for Rock Mechanics, Rock Engineering, Taylor, and Francis Group, 2009).

185. Shi, J., Xue, Z. & Durucan, S. Supercritical CO2 core flooding and imbibition in Berea sandstone — CT imaging and numerical simulation. *Energy Procedia* **4** (2011).

186. Wang, M., Wang, J., Pan, N. & Chen, S. Mesoscopic predictions of the effective thermal conductivity for microscale random porous media. *Physical Review E* **75,** 036702 (2007).

187. Clavaud, J.-B., Maineult, A., Zamora, M., Rasolofosaon, P. & Schlitter, C. Permeability anisotropy and its relations with porous medium structure. *Journal of Geophysical Research: Solid Earth* **113** (2008).

188. Chen, L., Kang, Q., Viswanathan, H. S. & Tao, W.-Q. Pore-scale study of dissolution-induced changes in hydrologic properties of rocks with binary minerals. *Water resources research* **50,** 9343–9365 (2014).

189. Chen, L., Kang, Q., Dai, Z., Viswanathan, H. S. & Tao, W. Permeability prediction of shale matrix reconstructed using the elementary building block model. *Fuel* **160,** 346–356 (2015).

190. Germanou, L., Ho, M. T., Zhang, Y. & Wu, L. Intrinsic and apparent gas permeability of heterogeneous and anisotropic ultra-tight porous media. *Journal of Natural Gas Science and Engineering* **60,** 271–283 (2018).

191. Zhou, Y., Yan, C., Tang, A. M., Duan, C. & Dong, S. Mesoscopic prediction on the effective thermal conductivity of unsaturated clayey soils with double porosity system. *International Journal of Heat and Mass Transfer* **130,** 747–756 (2019).

192. Wang, Z., Jin, X., Wang, X., Sun, L. & Wang, M. Pore-scale geometry effects on gas permeability in shale. *Journal of Natural Gas Science and Engineering* **34,** 948–957 (2016).

193. Tian, J., Qi, C., Sun, Y., Yaseen, Z. M. & Pham, B. T. Permeability prediction of porous media using a combination of computational fluid dynamics and hybrid machine learning methods. *Engineering with Computers,* 1–17 (2020).

194. https://github.com/yongganzhe001/GenPorMed.

195. Jin, Y., Wang, C., Liu, S., Quan, W. & Liu, X. Systematic definition of complexity assembly in fractal porous media. *Fractals* **28,** 2050079 (2020).

196. Aitkenhead, A. H. Converting a 3D logical array into an STL surface mesh (2010).

This Ph.D. thesis has been typeset by means of the TEX-system facilities. The typesetting engine was pdfLATEX. The document class was `toptesi`, by Claudio Beccari, with option `tipotesi=scudo`. This class is available in every up-to-date and complete TEX-system installation.